

**Interplay between charging effects and
multiparticle charge transport processes in a
tunable single electron transistor**

Doctoral thesis for obtaining the

academic degree

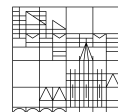
Doctor of Natural sciences (Dr.rer.nat)

submitted by

Laura Sobral Rey

at the

Universität
Konstanz



Faculty of Science

Department of Physics

Summary

In this thesis we study a device called single electron transistor (SET) where one of the junctions is a tunable atomic contact. Our device consists of an oxide tunnel barrier in series with a mechanically controlled break junction (MCBJ), being the element that allows to adjust the atomic contact. With this technique, it is possible to tune the electronic transmission of the atomic contact and thereby the coupling strength between the island and the respective electrodes. The part between both barriers is the island, and the energy for transferring an electron into it is the charging energy. Lowering thermal fluctuations, by cooling down the device to temperatures below 1K, and quantum fluctuations, by utilising junctions with a very small capacitance, make the charging energy (E_C) the characteristic energy of the SET. A third electrode is coupled to the island to act as a gate.

Until the applied energy exceeds E_C transport through the SET is not possible. This is known as Coulomb blockade (CB), and gives rise to the CB oscillations and diamonds. We will explore the limits for the CB signatures depending on the coupling of the atomic contact to the island. We will be able to characterise how charging effects vanish for higher transmission of the atomic contact, and also, how CB and the well defined energy levels inside the island vanish.

Using a superconducting material for one (or several) parts of the SET allows to have more types of transport, and in particular, multi-charge transport, namely Cooper pair transport and (multiple) Andreev reflections. In our devices, the island and one of the leads are made out of a superconductor (aluminium) and connected by a MCBJ. The other lead is made out of a normal material (copper) and is coupled to the island via an oxide barrier. This device bridges between the widely studied and better understood NSN-SET and the SSS-SET, which has a very high amount of possible transport processes and that has made it so far challenging to disentangle these

processes.

Therefore, in the second part of the thesis, we will present how the charging effects interfere with the multi-particle transport in the MCBJ. We will study how E_C modulates the different Cooper pairs and Andreev reflections over the MCBJ, and we will also be able to present such data for the strong-coupling regime. Having an atomic contact as one of the barriers in the SET allows to tune these multi-particles processes by adjusting the coupling of one electrode to the island. Charging effects caused by CB disappear when bringing the atomic contact to very large transmission.

Zusammenfassung

In dieser Arbeit untersuchen wir ein Bauelement, das als Einzelelektronentransistor (SET) bezeichnet wird und bei dem eine der Verbindungstellen ein regelbarer atomarer Kontakt ist. Unser Bauelement besteht aus einer Oxid-Tunnelbarriere in Reihe mit einem mechanisch gesteuerten Bruch-Kontakt (MCBJ), aus dem ein atomarer Kontakt gebildet werden kann. Mit dieser Technik ist es möglich, die elektronische Transmission des atomaren Kontakts abzustimmen. Der Teil zwischen den beiden Barrieren ist die Insel, und die Energie für den Transfer eines Elektrons in diese Insel ist die Ladungsenergie. Die Verringerung der thermischen Fluktuationen durch Abkühlung des Bauelements auf Temperaturen unter 1 K und der Quantenfluktuationen durch die Verwendung von Kontakten mit sehr geringer Kapazität machen die Ladeenergie (E_C) zur charakteristischen Energie des SET. Eine dritte Elektrode ist mit der Insel gekoppelt und dient als Gatterelektrode.

Solange die zugeführte Energie E_C nicht übersteigt, ist ein Ladungstransport durch den SET nicht möglich. Dies wird als Coulomb-Blockade (CB) bezeichnet und führt zu den CB-Oszillationen und -Rauten. In dieser Arbeit wird untersucht, bis zu welcher Kopplungstärke Hinweise auf CB beobachtbar sind. Insbesondere charakterisieren wir, wie die Ladungseffekte bei Kopplung des atomaren Kontaktes verschwinden.

Die Verwendung eines supraleitenden Materials für einen (oder mehrere) Teile des SET ermöglicht mehrere Transportmechanismen, insbesondere den Transport mehrerer Ladungen, nämlich Cooper-Paar-Transport und (mehrreiche) Andreev-Reflexionen. Bei unseren Bauelementen bestehen die Insel und eine der Zuleitungen aus einem Supraleiter (Aluminium) und sind durch einen MCBJ verbunden. Die andere Leitung besteht aus einem normalleitenden Material (Kupfer) und ist über eine Oxidbarriere mit der Insel verbunden. Dieses Bauelement stellt einen Zwischenschritt zwischen dem weithin untersuchten und gut verstandenen SNS-SET und dem SSS-SET dar, bei dem

es eine sehr große Anzahl möglicher Transportprozesse gibt, was es bisher schwierig gemacht hat, diese zu separieren.

Daher zeigen wir in einem zweiten Teil der Arbeit, wie die Ladungseffekte den Mehrteilchentransport durch den MCBJ beeinflussen. Wir untersuchen, wie die Ladungseffekte durch Anlegen einer Spannung an die Gatterelektrode die verschiedenen Cooper-Paar- und Andreev-Reflexionen über die MCBJ modulieren, und wir stellen solche Daten auch für den Bereich der starken Kopplung vor. Die Verwendung eines atomaren Kontakts als eine der Barrieren im SET erlaubt es, diese Mehrteilchenprozesse durch Anpassung der Kopplung an die Insel abzustimmen. Die durch CB verursachten Ladungseffekte verschwinden, wenn der Atomkontakt auf sehr große Transmission gebracht wird.

Acknowledgement

I would first like to thank my supervisor Prof. Scheer. Her role in this thesis was crucial and goes from the interest that she constantly showed in how the experiment was going to repair together with me the cryostat and passes by correcting every single grammatical mistake I had in any document from the last 4 years. It is a privilege to have a supervisor with such dedication that pays attention to the little details of all the steps of the process, from how the samples are produced to how the plots are presented, and that always has time to discuss on very short notice. On the same line, I would like to thank my predecessors Thomas and especially Susanne for the time (and patience) they took for introducing me to the project, to low-temperature measurements, to use Scheer II and in general for helping me whether I had doubts or problems with the cryostat. It was also a privilege to have access from the first day to an operating cryostat with everything ready to perform my measurements, and this was, without doubt, thanks to their hard work in previous years.

I would like to thank the theoretical part of the project, namely Prof. Siewert and Prof. Belzig, for helping to conceive the experiment, and for the large discussions that helped us to understand the results. Without them, it would not have been possible to understand and explain most of the measurements from this thesis. I would like to thank David and Prof. Cuevas for providing me with the needed data and for all remarks, questions and discussions.

I appreciate the help from Ansgar Fischer, Matthias Hagner, Mr Löble and Mr Romer for helping with the maintenance and repairment of Scheer II, and the Helium personnel, Mr Maier and Mr Sieber, for always adapting to my high demand of LHe and trying to reserve Hartmut for me.

I'm in debt to past members of the group that had the time (and patience) for introducing me to the different fabrication and measuring devices, and

for worrying in general for me, Julian Braun, Simon Haus, Thomas Möller, David Weber and Martin Prestel. Also thanks to my lab mates for the discussions about my measurements and regarding the cryostat, Lukas, Roman and Andreas. I wish all the success to the new guys dealing with SETs, Oliver and Patrick. I'm very thankful to all of AG Scheer and AG Di Bernardo for all the breaks, discussions (either work-related or random stuff) and free time that we spent together. Citing the persons I'm missing so far: Sara, Sergii, Alfredo, Prof. Di Bernardo, Mengqi, Fan, Jenni, Stefan, Valentin, Franz, Timo, Jannick, Nico, Sergej, Gautam, Marcel, Pryiana and I hope I'm not forgetting anyone! We have a very nice and collaborative work atmosphere where I always felt welcomed, so thanks to everyone for that! Also special thanks to the secretaries from P10 Eva, Kerstin, Sabine, Letizia, and Doris for always helping me with over complicated german administration forms.

On the other side, I feel very privileged that my project belonged (together with me) to the European ITN QuESTech. I am very thankful to the QuESTech consortium for all the meetings, gatherings and discussions together with the ESRs (Danilo, Jonny, Willy, Rebekka, Franz, Francesco, Ananthu, Elías, Arun, Naveen, Rishab) and especially to David, Dr Peltonen, Bayan, Danial, Prof. Pekola and Prof. Winkelmann for welcoming me in their respective labs and for all the given help. Also thanks to Prof. Courtois for being the leader of this collaborative grant and thanks a lot to Erika for always reminding kindly all the things I need to submit.

I wouldn't have come here if it wasn't for some of my friends, especially those who studied physics in Santiago together with me. Moitas grazas a toda a xente de Ponteareas, a USC e da residencia que sempre me animou, e grazas en especial á xente de física por sempre axudarnos entre nós e formar un grupiño moi guai. Here I won't write names because the list would be huge and for sure I would forget several people: you know who you are! :)

Finalmente, moitas grazas a miña familia, Pablo, Marcos, Cholo e especialmente grazas a miña nai Elena e a miña irmá Montse por sempre preocuparse por como iban as mostras e o cacharro, e por servirme de exemplo. Foi todo un detalle que solo fixerades un pequeno drama (e non un dramón) por virme a Alemania. Grazas por apoiarme e por sempre estar ahí. And last but not least, thanks to Leon, for all the support, all the time we spend together and for always reminding me what is important.

Contents

Summary	i
Zusammenfassung	iii
Acknowledgement	v
1 Introduction	3
2 Theoretical background	7
2.1 Tunnel junctions with normal and superconducting electrodes	8
2.1.1 NIN Junctions	9
2.1.2 SIN Junctions	9
2.1.3 SIS Junctions	10
2.2 Point contacts with arbitrary transmission	10
2.3 Single electron transistor (SET)	13
2.3.1 Energy considerations	13
2.3.2 Normal SET: Coulomb blockade (CB)	15
2.3.3 SSS SET; previous results on the orthodox and non-orthodox regime	18
2.3.4 SSN-SET	22
2.4 Master equation approach	23
2.5 SET in the strong coupling regime	25
3 Experimental methods	27
3.1 The mechanically controlled break junction (MCBJ)	27
3.2 Sample preparation	28
3.3 Measurement Setup	33
3.3.1 Device characterisation	34

4 The MCBJ-SET in the classical regime	37
4.1 Tunnel barrier characterisation	38
4.2 NNN and SSN MCBJ-SET in the classical regime	39
4.3 Charging energy calculation	41
4.4 Temperature estimation	43
5 Vanishing of the CB in the MCBJ-SET	45
5.1 Co-tunnelling in the SET	45
5.2 Vanishing of the Coulomb blockade for high \mathcal{T} channels	48
5.3 Re-normalisation of E_C	52
5.3.1 Dynamical Coulomb blockade	53
6 Interplay between MAR and charging effects	55
6.1 Multi-particle processes signals in the $I - V_b$ and the $dG - V_b$ characteristics	55
6.2 Low-coupling regime	58
6.3 Higher-order processes in the intermediate coupling regime	59
6.4 Multi-particle transport for high transmission contacts	65
6.5 Andreev reflection signatures in the strong coupling regime	69
7 Conclusions	73
A List of samples	75
B Python code	79
Bibliography	93

Chapter 1

Introduction

Charge in weakly coupled metallic structures is quantised in terms of the electron elementary charge e [1]. As a consequence, so called charging effects allow to detect the influence of a single charge in a macroscopic 'island', as to the transport properties of a circuit in which the island is embedded. Despite the fact that this island has a continuous spectrum for the energy levels, there is an extra quantity necessary to pay in energy in order for the transport to be possible: the charging energy (E_C). This discretises the energy spectrum for the island and gives a different reading for the total current through the system when one electron is able to tunnel through. This effect is known as Coulomb blockade (CB), because it blocks the transport for small bias voltages and after a certain value, allows the transport of one particle through it.

One possible realisation where we can get to measure the transports through the island is the single electron transistor (SET) [2] [3]. Classically, these devices have two tunnel barriers (TB) that separate the island from the two leads, and a gate coupled to this island. For the definition of the SET, the resistance R and capacitance C of these barrier play an important role: the quantum and thermal degrees of freedom are reduced by choosing junctions with adequate values for R and C . The classical SET transport is well described by the so-called orthodox theory. This is a simple approach because it neglects quite a few factors [4], but nonetheless, it has shown to have a very good agreement with measurements of the SET.

In this thesis we aim to explore how the problem changes when we stop thinking about the R and C between the island and the elements connected to it, and start considering the transmission values τ for the individual channels

of the junction instead. We need to do this because we are replacing one of the oxide barriers by an atomic contact. In the oxide junctions, one has to consider a very high amount of channels ($N \sim 10^6$) with very low transmission ($\tau \sim 10^{-6}$), while in an atomic contact the number of channels is small ($\sim 1-5$) and each of them has a high transmission ($\sim 0.01 - 1$). It is possible to study the transport for different couplings of this contact, and reproduce previous results performed on classical SETs for low transmission. The main interest here is to study contacts that have a very high transmission and that in principle overcome the limit of the definition for R . We can study how the CB vanishes when increasing the transmission of the channel, the strong coupling regime of the SET, and also discuss if the levels of the island are always discrete and well defined.

Our SET samples are formed by a superconducting island connected by a mechanically controlled break junction (MCBJ) to a superconducting lead and by an oxide TB to a normal lead. This is then a SSN-SET, never experimentally studied before, and that serves as a bridge between the well studied SNS/NSN structures and the more complicated case, the SSS-SET. Since one of the barriers connects two superconductors, our SET also allows us to study the interplay between the charging effects mentioned before and superconducting transport. Each particle that tunnels inside the island needs to pay an extra energy proportional to the charging energy. The value of it scales with the square of the transmitted particles inside the island. This competes with multi-particle transport processes typical for superconducting junctions, like Cooper pair transport and multiple Andreev reflection. We will study how these possible processes coexist and how do they predominate over others depending on the region of the bias we are looking at. Besides, we will discuss how these higher order processes charge the island and we will present as well how processes like Andreev and multiple Andreev reflection enter in the formalism.

This thesis has the following sections: in chapter 2, we make an introduction to all the theory concepts and data analysis necessary for treating our data. It starts by describing tunnelling processes on classical interfaces and in point contacts. Then, there is an introduction to the SET, from the simplest all-normal SET to the all-superconducting SET. Here, there is also an introduction to the SSN-SET, the device studied in this thesis, and we will also discuss the pros of including an atomic contact as a tunnel barrier in the SET. These concepts allows us to move on to discuss the master equation approach for calculating the current through the SET. Here we will include

our proposal for including multi-particle transport processes in the master equation approach for the transport of more than two particles. At the end of this chapter, there is a small introduction to previous results for the strong tunnelling regime of the SET, and how we can study also this regime with our devices.

Chapter 3 is focussed on the experimental techniques for making the measurements. First, there is a short introduction to the MCBJ, the method we use for creating the point contacts. After, there is an explanation on how to produce the MCBJ-SET samples. The chapter ends with a short description of the measurement set-up and the measurement techniques.

After chapter 3 we will present the experimental results of the MCBJ-SET together with the comparison to the simulations using the master equation approach and the rates for point contacts. In chapter 4 we will focus on the classical results from the MCBJ-SET, this means, the NNN and SSN-SET when the MCBJ has a very low \mathcal{T} . We will characterise here the samples, and test the master equation approach by seeing how well it fits to the classical regime. We also shortly explain how to estimate the temperature of this device from the Coulomb blockade oscillations.

Chapter 5 focuses on the normal MCBJ-SET results through different contact regimes, from low \mathcal{T} to values where the transmission of the point contact \mathcal{T} is well above 1. First we give a short introduction to the cotunnelling contributions on the SET for lower coupling regimes, how and where it appears on the measured data, and its relevance in our measured data. Section 5.2 has all the data that demonstrates how the CB vanishes as the $\mathcal{T} > 1$, in agreement with previous results and theory. We discuss the values of the charging energy for different values of the point contact of the SET in section 5.3. Finally, when $\mathcal{T} \gg 1$ the Coulomb oscillations coming from the gate disappear, but there is still a charging effect remaining: the dynamical Coulomb blockade. We present this measurement in section 5.3.1.

The results for the 'superconducting' case, i.e., the SSN-SET are in chapter 6. We start with an intuitive discussion on how one can argue what are each of the features by analysing how these features change over the different coupling regimes. The following sections focus on different coupling regimes, presenting measured data and a discussion together with the simulations: section 6.2 for the low coupling regime, section 6.3 and 6.4 for the intermediate coupling regime and section 6.5 for the strong coupling regime.

Chapter 2

Theoretical background

In this chapter we describe the theoretical concepts necessary for understanding the transport through a SET.

First, in section 2.1, there is a quick reminder of the transport and tunnelling rates for single tunnel junctions and the discussion goes for all normal junctions (NIN) 2.1.1, hybrid SIN junctions 2.1.2 and SIS junctions 2.1.3; in particular, in section 3.1, there is a introduction to the MCBJ technique and its applications as SIS junction.

In section 2.3, we will extend the discussion to systems with more than one junction, to eventually describe the SET [5][2][6][7]. First, in section 2.3.1 we will discuss about the elements and conditions that characterise a SET, and calculate the energy necessary for the transport through the device. This energy necessary for tunnelling off or on an electron on the island δE is what we need for calculating the rates from the previous section 2.1. Then, we will start by discussing the simplest version where all parts of the device are normal conducting in subsection 2.3.2. Here there is also a introduction to the Coulomb blockade (CB) effect. Then, the all superconducting SET (SSS-SET) and all the different transport processes are in subsection 2.3.3. And finally, in subsection 2.3.4 we introduce the SSN-SET and we discuss all the benefits and improvements that such a device brings.

In section 2.4 there is a description of the master equation approach for calculating the current through the SET. Here all the concepts introduced in previous sections come together, and we discuss how we need them for solving the master equation. In sections 2.4 it is explained how to include higher-order processes (Cooper pair tunnelling and multiple Andreev reflection, respectively) into the simulations.

Finally, in section 2.5, there is an introduction to previous studies on the strong coupling regime for the SET and vanishing of the CB in general. We discuss then what are the implications of both things on the MCBJ-SET.

2.1 Tunnel junctions with normal and superconducting electrodes

For the deduction of the different tunnelling processes (and associated rates) it is convenient to use the so-called *semiconductor model* [8]. This model represents the normal metal as a continuous density of states $N(0)$ and with occupied states below and above the Fermi energy E_F . The superconductor is represented as a semiconductor with a energy between the bands of 2Δ and the Fermi level in the middle of the Δ . The deduction of these expression can be found in [8] [7].

$$\Gamma_{1 \rightarrow 2}(eV) = \frac{A}{e} \int_{-\infty}^{+\infty} dE |T|^2 N_1(E) f(E) N_2(E + eV) [1 - f(E + eV)] \quad (2.1)$$

where $f(E)$ if the Fermi distribution:

$$f(E) = \frac{1}{1 - e^{\beta E}} \quad (2.2)$$

with $\beta = 1/k_B T$. For the density of states we take into account the Dynes parameter γ [9]:

$$\frac{N(E, \gamma)}{N(0)} = \begin{cases} Re\left(\frac{(E-i\gamma)}{\sqrt{(E-i\gamma)^2 - \Delta^2}}\right), & (E > \Delta) \\ 0, & (E < \Delta) \end{cases} \quad (2.3)$$

The Dynes parameter is a purely phenomenological variable from the measured experimental data (see section 4.1), that has been related in several works to the influence of the electromagnetic environment on the tunnel junction [10] [11]. The total current through the junction would be the sum of the forward and reverse rate: $I = e(\Gamma_{1 \rightarrow 2} - \Gamma_{2 \rightarrow 1})$.

2.1.1 NIN Junctions

Let's consider first the easiest case, two normal metals at the same potential and separated by an insulating layer (NIN junction). Since both Fermi levels are aligned, there is no net transport through the junction.

After applying a positive finite voltage on one side, this level would lower, allowing tunnelling from the conduction band of the grounded metal to the non-grounded one. Electron tunnelling (e or QP) is the only possible process in NIN junctions. Therefore the solution for eq. (2.1) equals Ohm's law:

$$I_{N \rightarrow N} = \Gamma_{N \rightarrow N} \cdot e = A|T|^2 N_1(0) N_2(0) eV \equiv \frac{V}{R_T} \quad (2.4)$$

which allows us to relate the density of states, transmission and constants simply to the resistance of the tunnel barrier (R_T).

2.1.2 SIN Junctions

If one of the leads is superconducting, equation 2.1 becomes:

$$\Gamma_{N \rightarrow S}(eV) = \frac{1}{e^2 R_T} \int_{-\infty}^{+\infty} dE \frac{N_S(E)}{N_S(0)} f_N(E) [1 - f_S(E + eV_b)] \quad (2.5)$$

Since the density of states on the normal metal is constant and equal to $N_N(0)$, it gets cancelled after the substitution with R_T . This is the tunnelling rate for a SIN junction from the normal to the superconducting metal. The rate in the other direction is:

$$\Gamma_{S \rightarrow N}(eV) = \frac{1}{e^2 R_T} \int_{-\infty}^{+\infty} dE \frac{N_S(E)}{N_S(0)} [1 - f_N(E)] f_S(E + eV_b) \quad (2.6)$$

This expression depends on the temperature of the normal metal, coming from β_N in eq. 2.2.

If we now re-write equations 2.5 and 2.6 in terms of the energy a particle gains when tunnelling, they would read:

$$\Gamma_{N \rightarrow S}(\delta E) = \frac{1}{e^2 R_T} \int_{-\infty}^{+\infty} dE \frac{N_S(E)}{N_S(0)} f_N(E) [1 - f_S(E + \delta E)] \quad (2.7)$$

and,

$$\Gamma_{S \rightarrow N}(\delta E) = \frac{1}{e^2 R_T} \int_{-\infty}^{+\infty} dE \frac{N_S(E)}{N_S(0)} [1 - f_N(E)] f_S(E - \delta E) \quad (2.8)$$

These equations verify that $\Gamma_{N \rightarrow S}(\delta E) = \Gamma_{S \rightarrow N}(\delta E)$, i.e. the rates do not depend on the tunnelling direction but just on the energy δE of the electron.

2.1.3 SIS Junctions

For an SIS junction, the rate reads:

$$\Gamma_{S \rightarrow S}(eV) = \frac{1}{e^2 R_T} \int_{-\infty}^{+\infty} dE \frac{N_{1S}(E)}{N_{1S}(0)} \frac{N_{2S}(E + eV_b)}{N_{2S}(0)} f_S(E) [1 - f_S(E + eV_b)] \quad (2.9)$$

Note that both of these expressions (eqs. 2.7 and 2.9) depend only on the resistance of the tunnel barrier R_T and on the superconducting gap Δ . This is a good approximation for tunnel barriers like the one we are considering for the SIN junction, i.e., a large amount of channels with a very low transmission each of them.

2.2 Point contacts with arbitrary transmission

In this section, we will introduce atomic size contacts that have a small number of channels with very high transmission. In such a small contact, it is not possible to describe the conductance of the superconducting weak link just in terms of a macroscopic quantity like the resistance as in the previous sections. In equation 2.10 the conductance comes from the sum of the individual conductance of each channel in the junction. If the transmission of one channel is 1, it contributes with one quantum of conductance $G_0 = 2e/h^2 \sim (12.9k\Omega)^{-1}$ [12].

$$G = \frac{2e^2}{h} \sum_{n=1}^N \tau_n = G_0 \sum_{n=1}^N \tau_n = G_0 \mathcal{T} \quad (2.10)$$

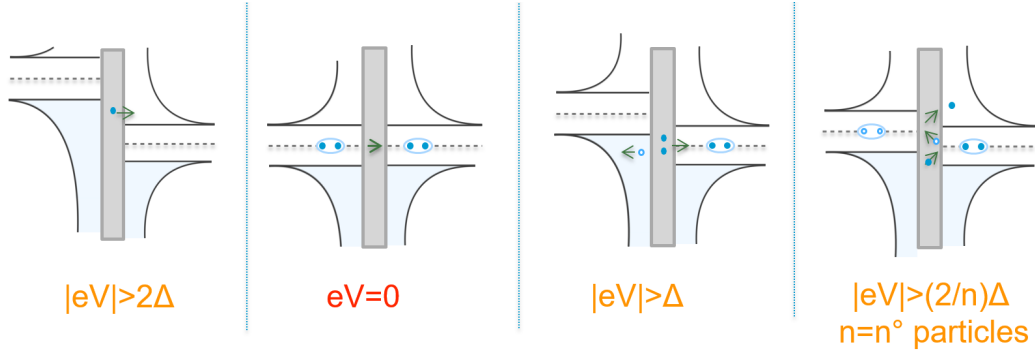


Figure 2.1: Possible transport processes on a superconducting contact with arbitrary transmission (considering same Δ at both sides) and their energy thresholds. In the left figure, single electron transport after overcoming a voltage of $V_b = 2\Delta$. In the left-centre figure, both levels are aligned, which allows Cooper pair tunnelling (cp). Multiple Andreev reflection (MAR) of order n is possible in the right figures after overcoming a threshold of $2\Delta/n$.

Equation 2.10 shows that the total conductance is the sum of the contribution of individual channels with transmission τ . Therefore, by changing the size of the point contact, it is possible to change the number of modes and therefore to change G in a step-like way [13]. This has been studied theoretically and measured in several materials showing different properties [14]. From now on, we will stick to superconducting point contacts. More about the fabrication technique and characteristics of these junctions can be found in section 3.2.

In a superconducting tunnel junctions there are multiple possible transport processes (fig. 2.1). If we consider that the gap Δ is the same on both sides of the junction, electron tunnelling (fig 2.1 (a)) would be possible after overcoming a threshold of exactly 2Δ . If both levels on the right and the left are aligned, the only possible process is Cooper pair tunnelling (fig. 2.1 (b)). This is a resonant process, i.e., as soon as the levels are not aligned it will stop. Finally, multiple Andreev reflection (MAR) of order n is possible at threshold of $V_b = 2\Delta/n$, being n the number of transmitted particles (fig. 2.1 (c) and (d)).

Previous theoretical works have approached this problem on how the different transport processes set in junctions with a single channel, and they succeeded to describe the $I - V$ characteristics of it [[15],[16],[17]]. In fig-

ure 2.2 there is an adaptation from [15] of a single channel with different transmission \mathcal{T} ranging from 0.05 to 0.95 for a BCS superconductor. For the biggest \mathcal{T} , the transport starts already at very low bias voltage and increases rapidly while for the smallest transmission the $I - V$ resembles the transport through a regular tunnel junction where there is just electron tunnelling after 2Δ . In the $I - V$ s for the intermediate values it is possible to discern certain kinks occurring at integers of $2\Delta/n$, where n corresponds to the number of transmitted particles so it can just have integer values of $n=1,2,3\dots$. These kinks correspond to MAR signatures of order n .

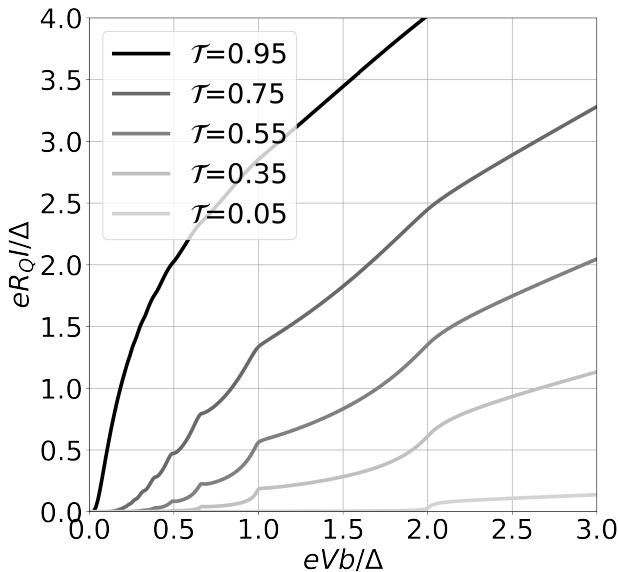


Figure 2.2: Voltage-current characteristics ($I - V$) of a superconducting MCBJ. The \mathcal{T} refers to transmission of a single channel. Order n MAR appears in the $I - V$ at $2\Delta/n$, which give rise to the characteristic kinks at these points of the voltage. Image adapted from [15], which focuses on BCS superconductors.

Later works were also able to disentangle the individual contribution from each MAR process to the current [[18],[19],[20]]. In figure 2.3 we can see the contribution to each single MAR processes separately. Summing up all the different curves on figure (2.3) gives figure (2.2) if they were calculated for a BCS superconductor. However, the transmission plot that we will be using in this thesis are calculated at 100 mK and have a Dynes parameter $\gamma \neq 0$,

so they are for non BCS superconductors.

There are several remarks on these transmission graphs. First, that independent of the \mathcal{T} of the junction, the thresholds for the different processes are always located at $2\Delta/n$. Second, a MAR process of order n is predominant in the voltage window of $2\Delta/n - 2\Delta/(n-1)$. The amplitude of orders $n > 3$ go quickly again to zero. For $n=2$ the amplitude of MAR remains constant for very high voltages, and the order $n=1$ (so single electron transport) grows linearly and becomes predominant at large voltages for both cases.

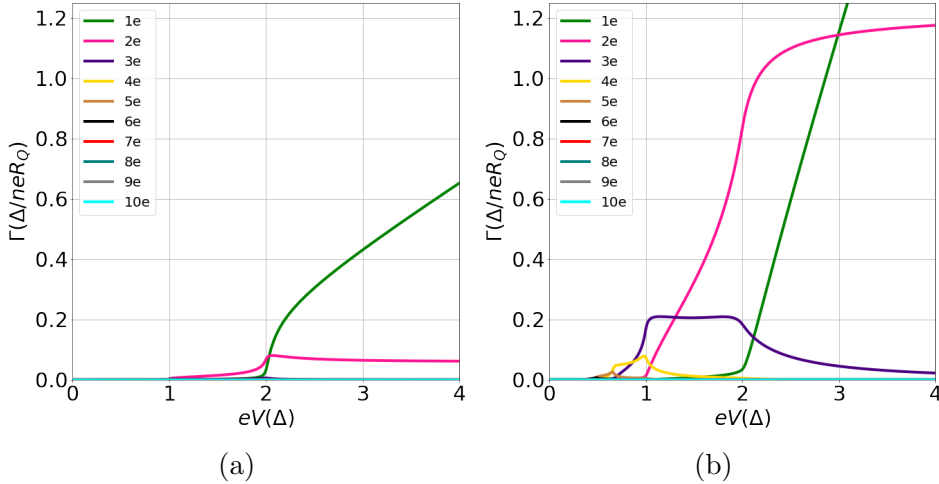


Figure 2.3: $I - V$ plot of each MAR order contribution for a channel with a transmission of $\tau=0.1$ (a) and $\tau=0.5$ (b). The different colours represent the different order of n transmitted particles, going from 1 (green) to 5 (brown). Data provided by David Ohnmacht.

Finally, each of the curves in fig. 2.3 described the transport of n particles. Therefore, it is possible to calculate the rate for each process Γ of the junction due to each contribution simply by dividing this current by ne .

2.3 Single electron transistor (SET)

2.3.1 Energy considerations

Let us consider first an island that is totally isolated from the rest of the world. The charge on the island must be an integer of the elementary charge

e , and therefore the charge can be written as $Q = Ne$. The electrostatic energy of the island is:

$$E = \frac{Q^2}{2C} = \frac{e^2}{2C} N^2 = E_C N^2 \quad (2.11)$$

where the charging energy E_C is a characteristic quantity that determines the energy necessary for charging the island with one electron.

A realisation for connecting this island to the outside world and measure the current through it is the single electron transistor (SET). A SET consists of an island coupled to two leads and a gate. From expression 2.11 it is possible to obtain the electrostatic energy for the SET [6] as:

$$E_{ch} = E_C(n - q/e)^2 \quad (2.12)$$

Where $E_C = \frac{e^2}{2C_\Sigma}$ now is proportional to the inverse of the sum of the capacitances coupled to the island $C_\Sigma = C_L + C_R + C_G$. q is the induced charge from all electrodes $q = C_R V_R + C_L V_L + C_G V_G$, and it is not quantised.

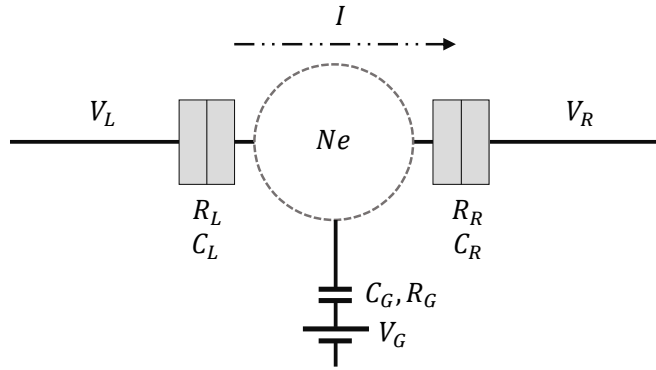


Figure 2.4: SET equivalent circuit. The number of particles in the island is N , so the charge of the island is Ne . In this generalised picture, the tunnel barriers and gate coupling appear as elements with a specific resistance R and capacitance C that connect the island with the voltage sources of these elements.

For making this charging energy E_C relevant, it is necessary to reduce as much as possible thermal and quantum fluctuations. Therefore, on the one

side $E_C >> E_{th} \sim k_B T$, which from eq. 2.11 translates to very small capacitances on the order of $C < 10^{-15}$ F, and requires also very low temperatures (below 1K). This is possible to achieve if the barriers have a very small area, below $1 \mu\text{m}^2$. On the other side, to assure that the particle is localised on the island, the resistance of these junctions needs to be higher than $2\hbar/e^2$ [21], which is approximately the quantum resistance $R_Q = h/e^2 = 25.8 \text{ k}\Omega$.

Now we need to know what is the energy n particles gain when tunnelling in or onto the island in order to calculate the rates for each process. This can be easily calculated with 2.12 as:

$$\delta E = E_{ch}(n) - E_{ch}(n \pm 1) + \kappa_i V_b = \mp 2E_C(n - q/e \pm 1/2) + \kappa_i V_b \quad (2.13)$$

where we already included the energy proportioned by the source κV_b . Since in our case the two junctions from the SET are not equal, we define a capacitor divisor [22] [21] as:

$$\kappa_L = \frac{C_G/2 + C_L}{C_\Sigma}; \kappa_R = \frac{C_G/2 + C_R}{C_\Sigma} \quad (2.14)$$

This energy from eq. 2.13 is what we need to plug into the rate equations explained before in eq. 2.5-2.9 for one single particle.

For two transmitted particles we would need to rewrite 2.13 as:

$$\delta E_2 = E_{ch}(n) - E_{ch}(n \pm 2) + 2\kappa V_b = \mp 4E_C(n - q/e \pm 1) + 2\kappa V_b \quad (2.15)$$

And for m particles:

$$\delta E_m = E_{ch}(n) - E_{ch}(n \pm m) + m\kappa V_b \quad (2.16)$$

One important point is to realise that these are the energies for adding (+) or removing (-) n electrons from the island. The rates are expressed as single charge divided by time, so when calculating them in terms of δE , it is necessary to take into account that $\delta E = \delta E_n/n$.

2.3.2 Normal SET: Coulomb blockade (CB)

In the simplest picture, just electron transport is possible through the SET, which in other words means that all the elements are normal conducting metals.

The energy levels on the island are discrete, so in a random configuration of these levels with respect to the chemical potential of the leads, the transport through the SET would not be possible (figure 2.5a). When applying a bias, there will be a value when the transport starts to be possible (figure 2.5b). This effect is known as **Coulomb blockade (CB)**: there is a blockade of the transport for small values of the bias voltage, until a specific voltage value when transport starts to be possible.

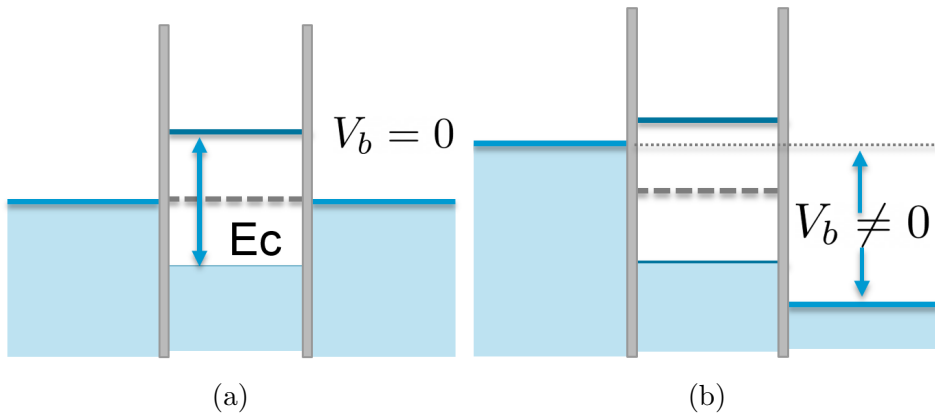


Figure 2.5: Simplified picture of the energy level diagram for a SET, in its ground state (a) and after applying a finite voltage (b). In (a) the transport through the SET is not possible, while in (b) the flow from left to right is possible.

Now, if we move the relative position of the energy levels of the island with respect to the leads, and we repeat the experiment, the bias voltage where the transport starts to be possible will change (fig. 2.6(a)). By repeating this $I - V_b$ characteristic for different gate voltages and plotting all the $I - V_b$ curves together in a 3D map, we can see the so-called Coulomb diamonds (fig. 2.6(b)). From a perspective of a gate voltage vs bias voltage map (fig. 2.6(c)) ($V_g - V_b$ or $n_g - V_b$ from now on) it is possible to see these diamonds quite clearly. Therefore this will be the representation that we will use for the rest of the thesis. From this representation it is possible to obtain very important characteristics from the SET; such as the E_C , the values for the capacitances of the junctions and also the coupling between the gate and the island for determining Q_g .

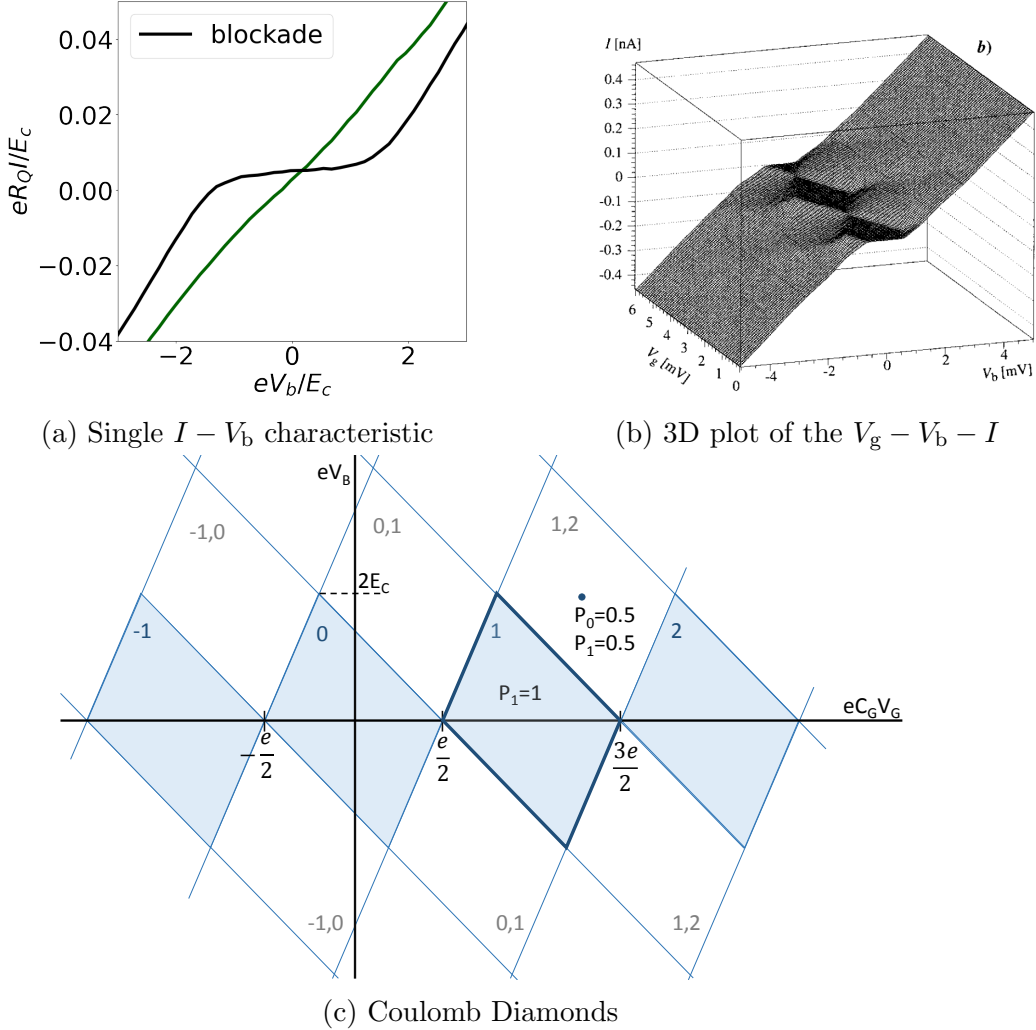


Figure 2.6: In (a) there are two $I - V_b$ curves that correspond to two different arrangements of the gate voltage of the SET. On the green line the chemical potentials of the three elements are at the same level and the transport through the SET is possible. On the black line the transport is blocked up to a finite bias. Figure (b) is a 3D plot that has $I - V_b$ combined with the dependence on the gate voltage V_g (taken from [23]). Looking from the $V_g - V_b$ perspective (c) the diamonds from (b) become more visible. From picture (c) several characteristic parameters of the SET can be extracted, such as the E_C and the coupling between the island and gate.

2.3.3 SSS SET; previous results on the orthodox and non-orthodox regime

In this section, we will be talking about different current cycles in the SSS-SET. Cycles are formed by a process that charges the island with n particles, followed by a second one that de-charges the island with n particles; then the cycle would be closed and it leaves the island in the original state afterwards.

The simplest cycle is the one already discussed in the previous section, which would be to charge the island through one of the junctions with an electron, and de-charging it through the other junction by another electron.

However, since all parts of the SET are superconducting, Cooper pair transport (cp) and MAR are also possible. Therefore, cycles that combine any of these transport possibilities are possible. All-superconducting SETs have a high number of possible transport cycles [24] [25] [26][27] which we are describing now (for simplicity, we are considering that the current flows from left to right):

- The Josephson-quasiparticle cycle (JQP)[28][29][24] [30] [31]: this cycle consists of (de-) charging the island with a Cooper pair and simultaneously (charging) discharging it with a quasi-particle through the other junction. In a second step, the remaining electron would tunnel through this second junction out and the island would recover its original state. Because one of the particles is immediately tunnelling through the other junction, it is considered that this cycle charges the island with just one particle. This cycle starts at $2\Delta + E_C$ (2Δ from the e tunnelling of the SIS oxide barrier) and if $E_C > \frac{2}{3}\Delta$ it would just 'stop' or get hidden when another cycle is energetically favourable. However, if the charging energy is $E_C < \frac{2}{3}\Delta$, the cycle will be between $2\Delta + E_C \leq eV \leq 2\Delta + 3E_C$ [24]. Finally, since the cp tunnelling is a resonant process (it is just possible when the voltage difference between the two leads is equal to zero), the JQP presents in the $I - V$ curves as a peak. This means, as soon as the condition of $eV = 0$ is fulfilled, the current goes up, but as soon as $eV \neq 0$ for the SIS junction, it goes back to zero.
- The Andreev-quasiparticle cycle (AQP)[24][21][25]: the AQP is the same concept as the JQP but with two particles that are transported by Andreev reflection. (Also, we would consider that there is no co-tunnelling like in the previous case). Therefore, now two particles would

tunnel onto the island through Andreev reflection on the left junction. In a second step, a single particle would tunnel off the island through the right junction. And in a final step, the last electron would tunnel off the island tunnelling through the right junction. Therefore the main differences with the JQP are that:

- The AQP is a threshold cycle: this is because the Andreev reflection itself is a threshold process, once you reach the energy necessary to transport particles through Andreev reflection it will also be possible for higher bias.
- Since it requires to overcome an energy of Δ on one of the SIS junctions to make AR possible, this process starts at $3\Delta + E_C$.
- This cycle charges the island with two particles.
- The multiple Andreev reflection-quasiparticle cycle (MARQP)[25] [32]: the last cycle can be generalised to n particles. In this case, n electron would tunnel onto the island through the left junction, and then tunnel off the island individually through the right junction. The location of this cycle would start at $\frac{2}{n}\Delta + 2\Delta + E_C$.

Table 2.1: Possible cycles on a SSS SET. It is also specified if the processes are threshold (T) or resonant (R). Table reproduced from [24]

Name	Cycle components	Position
$n \rightarrow n \pm 1$		
SET	e,e	T: $4\Delta \leq eV \leq 4\Delta + 2E_C$
JQP	J-e, e	R: $2\Delta + E_C^*$
AQP	A-e, e	T: $3\Delta + E_C \leq eV$
3e	J-e, J-e	R: $eV = 2E_C$
3e-A	J-e, A-e	R: $\Delta + 2E_C \leq eV$
3e-AA	A-e, A-e	T: $2\Delta + 2E_C \leq eV$
$n \rightarrow n \pm 2$		
supercurrent	J,J	P: $eV \sim 0$
JA	J,A	P: $\Delta \leq eV$
AA	A,A	T: $2\Delta \leq eV$

* $2\Delta + E_C \leq eV \leq 2\Delta + 3E_C$ if $E_C < 2\Delta/3$ (Ref. [30] and [29])

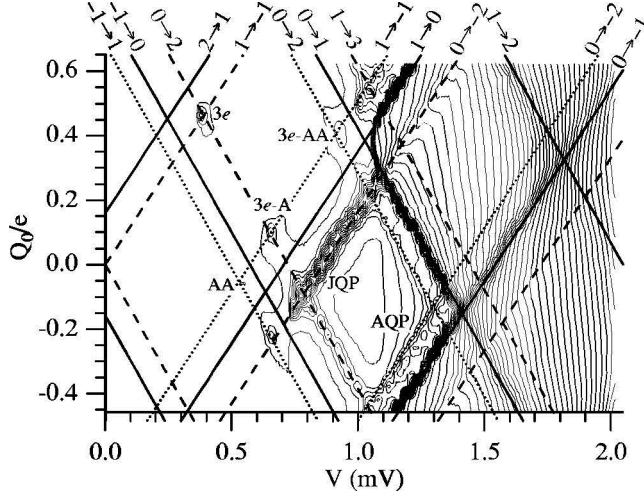


Figure 2.7: Transport diagram on a classical SSS-SET. The different lines represent the threshold (solid lines for e and dotted lines for AR tunnelling) or resonant (dashed lines for cp transport) conditions. Plot taken from [21].

And, what makes them particularly interesting, is that each of this processes shows up at a different energy threshold. The idea then is that this would make it possible to differentiate some of the multi-particle processes with a simple $I - V_b$ curve on the device since each of them would appear at a different voltage threshold, see table 2.1. In figure 2.7 there is a stability diagram of such device. The different resonant points/lines are marked, which allowed the authors to identify to which particular cycle each feature corresponds.

The first problem of such devices is that most of these higher-order processes are hindered by the tunnel barrier [33] [34], showing a very small amplitude in most of the cases. To avoid this, previous works included a MCBJ in an SSS SET [25] [35] [36]. The MCBJ substitutes one of the oxide barriers and acts as a tunable barrier in the SET between one of the leads and the island. The main benefits of a MCBJ-SET are:

- Higher-order processes: MCBJ allows by its nature Cooper pair transport, as well as multiple Andreev reflections up to high order depending on the transmission of the junction. Therefore with such SET it is possible to easily measure cycles that include such processes.

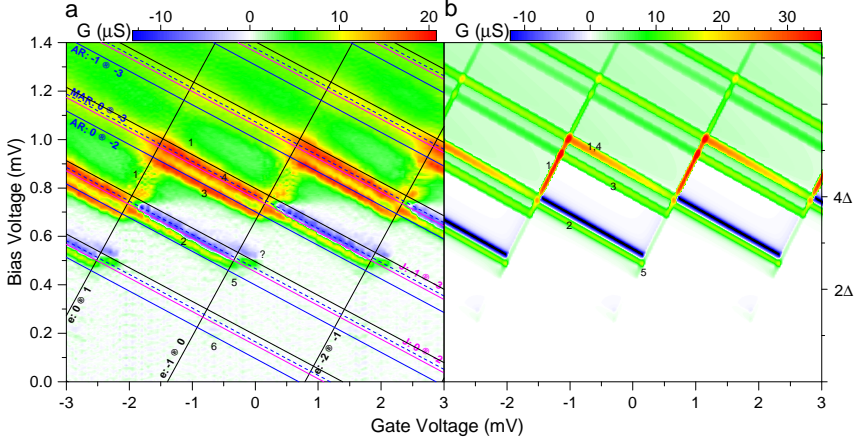


Figure 2.8: Experimental (left) and simulated (right) results for a SSS-SET with a MCBJ. Measurements and simulations show e cycle (1), JQP(2) AQP(3), MARQP (4) and signs of $3e$ and J-A (6). Some of the processes are not covered by the theory (labelled as ?). Plots taken from [25].

- Charging effects: depending on the coupling of the island to the leads, the charging energy would vary, as well as the resistance R of the MCBJ. This allows to explore the limits of the conditions for neglecting quantum and thermal fluctuations that define the SET.
- Tunability: finally, but not less important, just one sample is necessary for studying different coupling regimes (from high to small transmission) as the transparency of the junction changes while opening or closing the MCBJ.

Figure 2.8 shows a measurement and a simulation of such a device. Here the MCBJ was adjusted for having a R of $R_{BJ} = 72 \text{ k}\Omega$ and the tunnel barrier had a resistance of $R_{TB} = 112 \text{ k}\Omega$. Here some of the processes observed in fig. 2.7 are visible too, and besides they were able to distinguish a MARQP cycle. Some of the processes measured in this regime are already not reproduced by the simulations taking into account the classical rates and the orthodox theory.

Although this realisation of the SET opens up a new range of possibilities and simplifies the technical problem of allowing multi-particle processes, the number of possible cycles from table 2.1 has increased tremendously. To

simplify this problem we will introduce in the next section, and study for the rest of this thesis, the conceptually easier SSN-SET.

2.3.4 SSN-SET

The SSN-SET that we will discuss from now on consists of a MCBJ in series with a SIN oxide barrier. When the MCBJ breaks, it forms the SIS contact. Between the two tunnel barriers there is a third lead coupled that works as a gate. There are a few theoretical works for this type of SET [37] [38] and also some indirect experimental realisations [39], but the concept was never studied experimentally before.

The main benefit of this configuration is that the number of possible cycles is lower than in the SSS-SET because the SIN junction just allows single electron transport. Therefore the cycles that were possible in the SSS-SET from table 2.1 reduce to table 2.2.

Table 2.2: Possible cycles in a SSN-SET. As in table threshold (T) or resonant (R).

Name	Cycle components	Position
$n \rightarrow n \pm 1$		
SET	e,e	T: $3\Delta \leq eV \leq 3\Delta + 2E_C$
JQP	J-e, e	R: $\Delta + E_C$
MARQP	MAR-e, e	T: $2/n\Delta + \Delta + E_C \leq eV$

The different cycles here as well occur at different energy thresholds, which allows to identify them separately by just localising in the $I - V$ curve at which voltage the different kinks occur. Note that now, in comparison with table 2.1, the cycles start at a different position. The difference of one Δ is because now in the oxide barrier junction, (the SIN) just a voltage bias of Δ instead of 2Δ is necessary for the single electron transport to be possible.

Other types of hybrid SET have been widely studied before, but exclusively as SNS or NSN devices ([40] [41] [42] [22] [43] [44], [45], [4]). The sub-gap characteristics of these are well understood, while for the SSS, since there are so many possible transport processes, there are some features that

show as new processes that cannot be explained by the theory. Therefore, the SSN-SET is a bridge between the two types of realisations that can help to disentangle some of the unknown processes from the all-superconducting SET.

Finally, we would like to describe the 3e process [46][47], listed in table 2.1 and it is in principle a process that is measured regularly in the SSN-SET [48]. In this process, 3 particles are transmitted through the SET but the island is just charged with one electron: in a first process, two electrons tunnel through the left junction and simultaneously another electron from the island tunnels off through the other junction. In the next step, one electron tunnels via the left junction and two leave simultaneously the island through the right junction. This charges the island with one charge, but in the whole process the source is giving three electrons. Therefore the energy of the process is:

$$\delta E_{3e} = E_{ch}(n) - E_{ch}(n \pm 1) + 3\kappa V_b \quad (2.17)$$

We measure conceptually similar processes in the SSN-SET (section 6.4). This one in particular characterised for starting at a voltage 3 times smaller than the single electron tunnelling: following the last equation (2.17) the threshold is $V_{3e} = V_{se}/3 = \Delta$. For the same reason, the slope of this process in the $V_g - V_b$ is three times smaller in comparison with the single electron transport.

2.4 Master equation approach

To calculate the current through the SET we use the master equation approach [45]. This equation (2.18) takes into account that the rates over the single junctions depend on the island charge due to previous tunnelling processes, i.e., on the probability $P(n)$ that the island has n excess electrons due to previous tunnelling events.

$$P_{n \rightarrow n+1} \Gamma_{n \rightarrow n+1} = P_{n+1 \rightarrow n} \Gamma_{n+1 \rightarrow n} \quad (2.18)$$

These probabilities are normalised by the condition:

$$\sum_n P_n = 1 \quad (2.19)$$

For a single particle tunnelling in this system, the tunnelling rates are given by the expressions 2.4, 2.6 or 2.9 depending on the junction and after taking into account that for a SET the δE comes from eq. 2.13. The steady-state probabilities $P(n)$ of various charge states on the island are calculated by solving the system of equations from (2.18- 2.19). This solution comes from numerical methods since this system becomes very large when considering several charge states and different processes that charge the island with n particles. This program is in appendix B.

After both the rate Γ and the $P(n)$ are known, we can calculate the current with eq.(2.20):

$$I = e \sum_n P_n (\Gamma_{1,n \rightarrow n+1} - \Gamma_{1,n \rightarrow n-1}) = e \sum_n P_n (\Gamma_{2,n \rightarrow n-1} - \Gamma_{2,n \rightarrow n+1}) \quad (2.20)$$

Where the current through the left and right junction is the same since we are assuming there is no charge accumulation in the island.

It is also possible to calculate the rate over a single junction on the SET for higher-order processes that charge the island with $n > 1$. Although previous works were able to measure AR and MAR over 'opaque' tunnel barriers, in our experiments we never observed contributions from these processes from oxide barriers. Only in the MCBJ we could measure higher-order processes.

Therefore, the approach that we take is to obtain the rates from the MCBJ calculated for n particles separately as explained in section 3.1.

For a more general case where more particles can tunnel in or out simultaneously, i.e. for MAR, we can use the generalised expression of the master equation:

$$\sum_{n \neq n'} P_{n' \rightarrow n} \Gamma_{n' \rightarrow n} = P_{n \rightarrow n'} \sum_{n \neq n'} \Gamma_{n \rightarrow n'} \quad (2.21)$$

The rates in equation 2.21 are then the ones related to the MCBJ taking into account the energy that is necessary to pay in order to tunnel n particles (eqs. 2.15,2.16).

This whole treatment for calculating the current of the SET belongs to an approach known as the **orthodox theory**. As we have seen, for this we have ignored quite a few parameters, like the dimension and shape of the tunnel junctions, the duration of tunnelling processes or a possible duration of the electric charge re-distribution inside the electrodes [4]. The problem

is reduced to analyse the different charge and energy states of each of the SET components and to connect the probability of each charge state with the amplitude of each process. Nonetheless, this theory has shown to fit very well previous SET results [22] [26] [49], and one of the aims of this thesis is to explore the limits of this approach when considering high-transmission junctions with a small amount of channels.

JQP simulation: Averin-Aleshkin approach

In their work [5], Averin and Aleshkin come to an expression for calculating the rate of the JQP on a SET.

$$I = \frac{\gamma E_J^2}{4\delta E_2^2 + (\gamma/(2\pi))^2} \quad (2.22)$$

where, $\gamma = \Gamma_{N \rightarrow S}(\delta E_1)$ and following the Ambegaokar-Baratoff formula, it is possible to obtain E_J of a tunnel barrier from the SC gap Δ as $E_J = \frac{\Delta}{8R}$ [8].

This rate is a pseudorate since it is a process that charges the island with one single particle [6], because one of the particles simultaneously tunnels through the second junction in a coherent process.

MAR-QP simulation

For the MAR-QP cycle, it is not clear so far if the MAR tunnelling charges the island with actually the value of the transmitted particles, or if the island gets charged with a smaller value. Or both options, since one doesn't exclude the other.

It is possible with the master equation approach to include both processes and to check what exactly shows up in our measurement. In the case when the MAR of order m charges the island with m particles, the energy cost will be δE_m (eq. 2.16). This processes threshold is in any case at 2Δ .

2.5 SET in the strong coupling regime

One of the things that it is possible to study with the MCBJ-SET are the limits of the quantum condition, this means, to explore the limit where $R < R_Q$. This is known as the strong coupling regime. This is possible by increasing the transmission of the atomic contact, which will increase the conductance of the whole device.

Previous works have shown how the Coulomb Blockade (CB) vanishes for high conductances ([50] [51] [52]) in agreement with previous theories ([53]). For that, they compare plots of the normalised conductance G/G_0 (maximum and minimum of the CB peak) with respect to the reduced temperature $k_B T/E_C^0$.

With our data we can perform a similar analysis. We can calculate the temperature following the procedure described in section 4.4 and the charging energy as described in section 4.3. However, in our case, since we didn't perform any T dependent measurements and the E_C as we will show in section 5.3 does not significantly change for $\mathcal{T} < 1$, we cannot reproduce exactly this graph.

Other theory works have focussed on the channel nature and its transmission for the CB effect ([54] [55] [56]). An analogous analysis was presented in [57] where they mostly focussed on measure that, according to those previous theories, charging effects and the CB oscillations persist as long as there is a ballistic channel on the junction that has no $\tau = 1$. In this experiment, it is demonstrated that soon as one of the channels in contact with the island has $\tau = 1$, the CB oscillations and the charge quantisation vanish.

An equivalent analysis on the MCBJ-SET is in section 5.2.

Chapter 3

Experimental methods

3.1 The mechanically controlled break junction (MCBJ)

In section 2.2 we introduced the concept of an atomic contact. Here we will focus on one of the possible experimental realisations of such contacts: the mechanically controlled break junction (MCBJ).

When talking about MCBJs we are referring exclusively to thin-film MCBJs. This version makes it possible to build such a sample where the MCBJ is in series in very small distance with an oxide barrier. This thin-film MCBJs are small constrictions patterned on top of a bendable substrate. The atomic contact is adjusted by bending the substrate and breaking this small constriction.

At variance with other methods for creating atomic contacts like scanning tunnelling microscopy, MCBJs have shown to be able to create very stable contacts over long periods of time, crucial in our case since the measurement of individual current-bias voltage curves takes hours.

Superconducting MCBJs are a good method for creating the appropriate conditions for allowing MAR signatures. As explained in section 2.2, these appear as kinks in the $I - V_b$ characteristics of atomic contacts. Previous works [58] have reported signatures in the $I - V$ characteristic for aluminium break junctions (like the one we will be using in this thesis). These studies have shown that the best fit for the $I - V$ s comes from considering three channels with transmissions between 0.3-1 each of single atom contacts. This agrees with the fact that aluminium has valence 3, and after hybridisation

and due to the spatial distribution of each orbital, it is quite likely that there is one channel that is the dominant (i.e., has the highest transmission) and two others that will have a much smaller transmission [59].

3.2 Sample preparation

The samples are prepared as follows:

The bronze wafer is bendable for allowing the break of the MCBJ. First, it has to be polished and cleaned. After this, a layer of polyimide (Durimide 115A distributed by *Fujifilm*) is spin coated on top of it (fig. 3.1 I); this has the function to isolate the metallic wafer from the sample, and later it will be an adequate material for creating free standing junctions. This layer is soft-baked at 170 °C for 30 minutes, and hard-baked in vacuum at 350 °C for an hour.

On this wafer, first a layer of copolymer (MMA-MAA EL11 by *Micro chem USA*) is spin coated and then baked for 5 minutes at 100 °C on a hot plate. A layer of polymer (PMMA A6 by *Micro chem USA*) is deposited on top, also with spin coating, and baked at 170 °C for 30 min in the oven (fig. 3.1 II). The first copolymer layer works as an adhesion layer and besides offers the chance of having an undercut below the sample design that is directly exposed on the top most layer. The exact design of the sample is written on the polymer layer on top.

The wafer is then ready for use. The wafer pieces are 22×3 mm. The sample size with the pads is 8.5×1.5 mm and it is placed in the centre of the device. This is crucial because the extremes of the sample need to be clamped on the mechanism for breaking the MCBJ.

All structures of the sample are written within one e-beam lithography step (fig. 3.1 III and using the mask from fig. 3.2). For the smallest details (the ones from the 100 μm write field with the 20 μm aperture) the dose is 170 μAs/cm² and the beam current about ∼ 25-30 pA. This write field includes the island, the MCBJ and the finger (the longest extension from the second lead for creating the oxide barrier, third zoom in figure 3.2). For the leads and the pads (1000 μm field with the 120 μm aperture) the dose is 150μAs/cm² and the beam current is 8000 pA. For all structures the acceleration voltage is 10 kV. The connectivity between the different parts can be challenging due to the misalignment between the different apertures, vibrations, or mismatching after moving the stage for the 1000 μm write

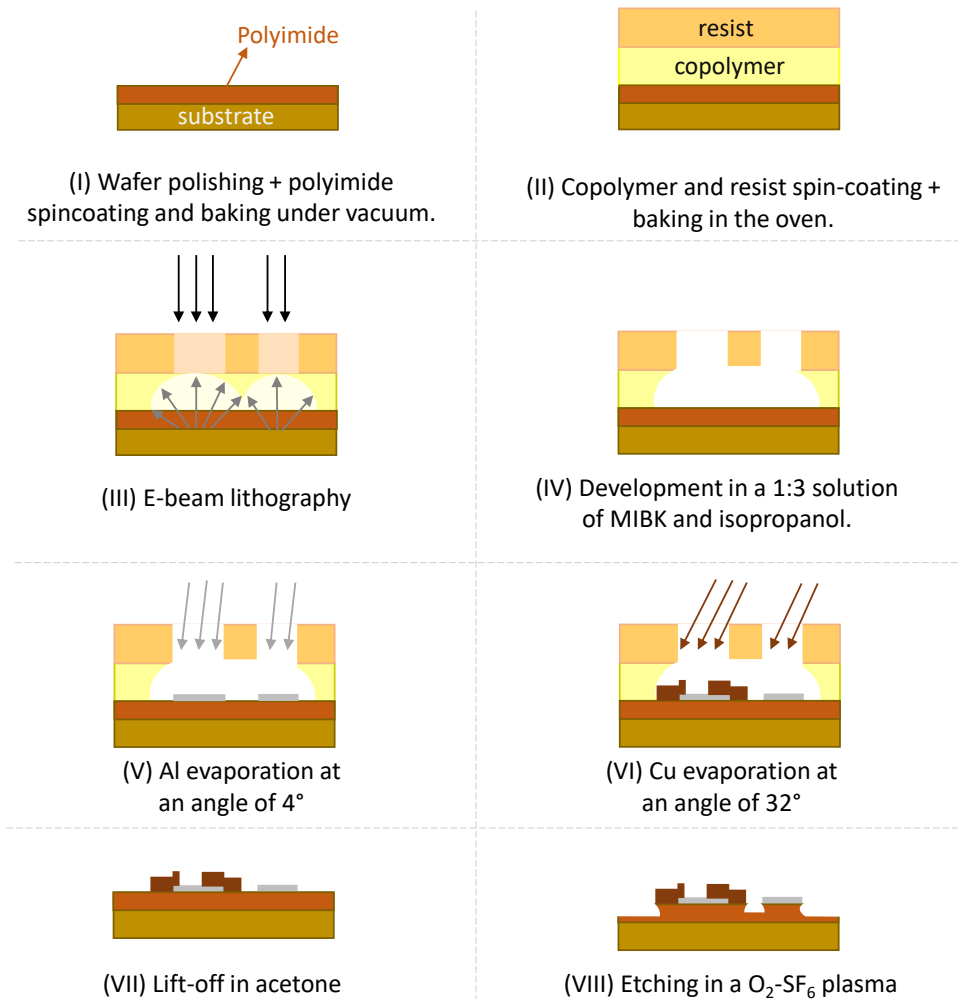


Figure 3.1: Sample fabrication steps

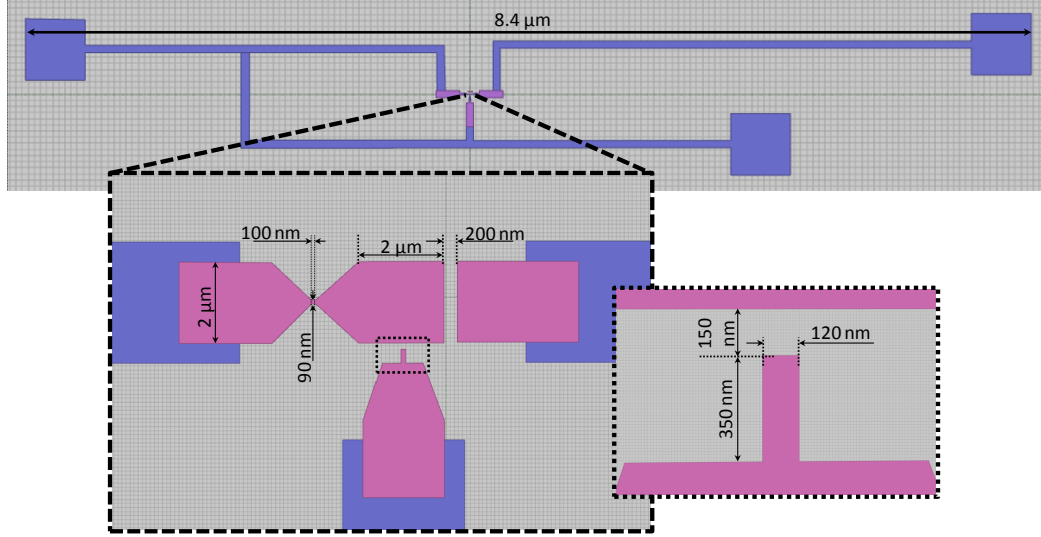


Figure 3.2: Lithography mask with the sample design with all dimensions. In purple, the parts in a $1000 \mu\text{m}$ write field, and in pink, the parts in a $100 \mu\text{m}$ write field. See text for the details of the parameters of each writing process.

field. In order to assure all the connections between the inner structure and the pads, we introduce an overlapping between each $1000 \mu\text{m}$ write field of $30 \mu\text{m}$. Between the $100 \mu\text{m}$ and $1000 \mu\text{m}$ write field, very big leads are written on top of the small ones from the $100 \mu\text{m}$ write field in order to assure the overlap.

After exposure, and since this is a negative resist, a development with a solution of 1:3 methyl isobutyl ketone (MIBK)-isopropanol will remove the exposed surface of resist (fig. 3.1 IV). 25 s in this solution are enough, and afterwards the sample goes into a pure isopropanol bath for a short time in order to stop the reaction.

For evaporation, and since it is necessary to achieve a continuous and very homogeneous Al film for growing a high quality oxide barrier, a very good vacuum is mandatory. For that, first we would clean the sample holder with isopropanol and blow it dry with high pressure nitrogen. Heating the wafer pieces mounted on the sample holder up to 100°C also helps to evaporate most of the possible remainders of water from the sample holder. Finally,

the sample holder with the samples stays in the loadlock of the evaporator over night for reaching pressures in the order of 10^{-8} mbar.

This very good vacuum is necessary because Al oxidises very fast, and a low concentration of impure O₂ can oxidise the surface fast and in a non clean way. For growing a high quality oxide barrier, a layer of homogeneous Al needs to be in a controlled atmosphere of O₂ for a relatively short time [60] [61]. After growing, the only possibility to protect this thin layer of Al₂O₃ is by depositing a second layer of other material on top (Cu in our case) without breaking the vacuum in between. Afterwards, we can take it out of the vacuum being confident that the Ox present in the air will not disrupt the Al₂O₃ layer, because they have no contact.

With a process known as shadow evaporation it is possible to create the different Al and Cu parts of our sample without breaking the vacuum of the evaporator. The key is to evaporate each of the layers at different angles: first, 40 nm of Al at an angle of 4°(fig. 3.1 V), then 90 nm of Cu at 35°(fig. 3.1 VI). In our evaporator, there are actually two evaporation sources: a thermal evaporator exclusively for Al pellets, and an e-beam evaporator with 4 possible pockets where we will put a Cu target. The Al evaporator is at an angle of approximately -4° with respect to the perpendicular line of the sample holder, and the e-beam evaporator is at an angle of approximately 4°. Therefore the effective angles are 0° and around 40°. The big difference of the angles allows to evaporate the shadow of the constriction of the MCBJ onto the resist, leaving just one MCBJ. The thickness difference is necessary for assuring a continuous layer of Cu on top of the Al: normally, when evaporating, the second layer needs to be thicker than the first such that the step-like parts are covered. When using big angles like in our case, we experienced that a considerable thickness of Cu is necessary for assuring the continuity of the small details. Therefore, for being always on the safe side, we decided to evaporate twice the amount of Cu with respect to Al. Between the two evaporations the sample is moved to the load-lock of the evaporator, where it stays for 3 min with an O₂ pressure of around 3 mbar for growing a smooth oxide layer on the Al.

After evaporation, a lift-off in acetone (heated to 50 °C if it is necessary to accelerate the process) removes all the resist and the evaporated metal on top, leaving just the patterned structure (fig. 3.1 VII). A short bath in isopropanol removes all the acetone remainders, and afterwards, we blow the sample dry with pressurised nitrogen.

The last step of the sample fabrication is an isotropic etching process

for removing the resist below the break junction (to form a free standing constriction), which makes the breaking process possible. For this we use a mixture of SF₆ and O₂ at 1 mbar, 45 W and 12 V, for around 14-16 min (fig. 3.1 VIII). This process removes around 550-650 nm of the polyimide.

The pads for contacting the sample are 0.5 mm squared. This allows to contact the sample by putting a Cu wire on top of the pad and fixing it with conductive silver paint. This Cu wire is either a 50 or 90 μm diameter twisted cable for biasing the sample, and a single for the gate. The inner structures of our device are far away from these pads, so they will not get covered with silver conducting paint. For avoiding electrostatic shocks while contacting, there is an additional lead patterned that shorts the bias leads of the sample. When the contacts are in place, we test the bonds, and then scratch out this short. Finally the cables are glued to the substrate to avoid ripping them off while installing the device in the cryostat.

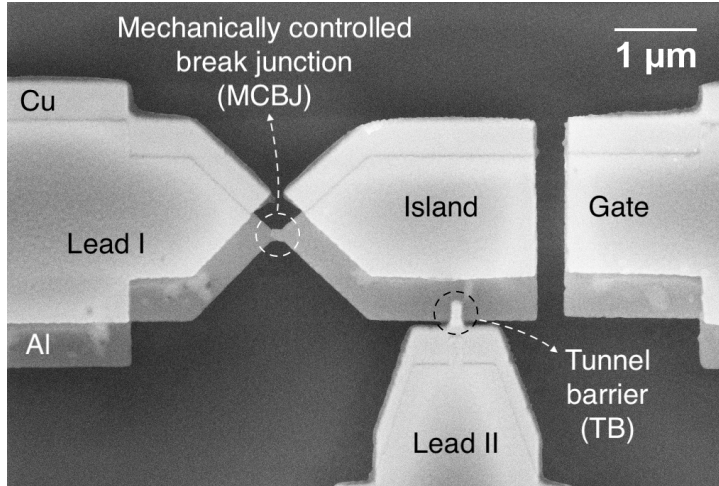


Figure 3.3: SEM picture of a SSN-SET sample (sample I after measurement). The darker parts of the structure in the picture are Al (S) and the lighter are Cu (N). The SIS junction is the MCBJ and the SIN junction is the TB, and each of them connects one of the leads to the island. The last electrode is the gate on the right of the picture, keeping a distance of around 200 nm to the island. Note that just the Al part of the MCBJ is continuous, while the Cu part of the MCBJ is not, and therefore the transport is just possible across the superconducting part.

The distance between the pads is large to avoid a shortcut between them

while contacting. There are three pads, two for applying the bias voltage to the island and the other one for controlling the gate voltage.

A SEM picture of the final sample is fig. 3.3. The inner part of the sample is a $2 \times 2 \mu\text{m}$ island connected to the leads via a MCBJ and a tunnel barrier (TB). The lighter parts are Cu, and the darkest Al. It is visible how the only possible path for current transport is through the Al break junction, since the Cu MCBJ is not connected due to the large angles used in the shadow evaporation step. This is a picture of sample I after the measurement.

3.3 Measurement Setup

We use a commercial dilution refrigerator (AirLiquide Maxidil 100) for low temperature measurements of the sample. With this set-up it is possible to reach temperatures that are on the range of 20-50 mK on the sample. All measurements are then at a maximum temperature of 60 mK at the sample. For reducing the electronic temperature there are 4 levels of filters between the electronic devices and the bottom end of the lines: a RC filter in the 4K plate, and Cu-powder filters at the level of the still, the mixing chamber and the sample. For reducing the noise level there is a voltage divider at room temperature with a factor 1/100. The cabling has a disposition that allows to create a symmetric bias at the sample (figure 3.4) by applying $+V/2$ and $-V/2$ at each side. The sample has a series reference resistance at each side with an approximate value of $110 \text{ k}\Omega$. This circuit enables to independently vary the bias voltage and the gate voltage. It also avoids offsets or influences generated by the thermal voltage created from the top to the bottom of the cryostat, since this voltage cancels out on those dispositions.

For the measurement, we apply a voltage over the whole configuration (sample + resistances) and then measure the voltage drop on one of the reference resistors (for calculating later the current) and on the sample. The signal is a quasi-DC voltage, i.e., a sinusoidal signal with a very low frequency. For reducing the noise on the measurements we average normally between 3-6 of this voltage sweeps.

In the cryostat a breaking mechanism is mounted at the bottom that consists of a series of connected screws and wheels. It is connected to an outside motor to turn the these pieces, which translates to an up-down movement of the last step of the mechanics.

The measurement setup, electronics and breaking mechanism are well

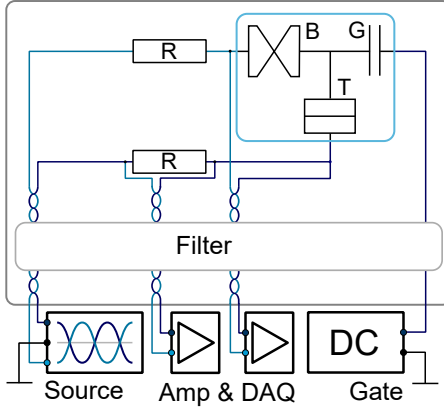


Figure 3.4: Cabling scheme of the cryostat. Figure taken from [35].

described in [35] and also in [36], so for more details refer to these works.

3.3.1 Device characterisation

We measure all samples at three different temperature stages while cooling down: room temperature, liquid nitrogen temperature and liquid helium temperature, namely around 298 K, 77 K and 4K. The resistance of the oxide tunnel barrier increases by 20% to 50% while cooling down.

The characterisation of the SIN junction requires temperatures below 1K. It is important to note that we have no means to measure any of the junctions separately. This means that after breaking the MCBJ we would always measure two junctions in series, since the MCBJ never comes back to its original state even after totally removing the bending. Therefore at this point, before breaking the MCBJ, it is possible to characterise the superconducting gap Δ , the Dynes parameter γ and the temperature T (see section 4.1).

Once this is done, we can break the MCBJ for finally creating the SET. By moving the mechanics it is possible to adjust contacts that go from very low transmission (~ 0.01) to contacts with one to few channels with transmissions over the order of ~ 1 . For each of these contacts we systematically measure the normal conducting map ($I - V_b - V_g$), achieved after applying a small magnetic field of around 30-50 mT, and the 'superconducting' map, in which one of the leads and the island are superconducting.

The bath T of for the measurements of sample I and sample III is always between 25-60 mK. In sample II, the bath temperature was most of the times higher than this, stabilising at the sample level at a value of around 100 mK. Tables A.2-A.4 in Appendix A has all the information for the T of each contact.

Chapter 4

The MCBJ-SET in the classical regime

From now on we will report the experimental results of the samples listed in appendix A. We will also present the simulations for each regime in comparison with the measurements, which we performed with the code in appendix B.

In this chapter we will focus on the classical regime of the SET. We will explain how to characterise the oxide barrier of the SIN junction in section 4.1, this means, to calculate the superconducting gap Δ and the Dynes parameter γ .

In section 4.2 we present our measurements for the normal and SSN-SET. There is also a comparison with the corresponding simulation. We will discuss here the difference between using classical rates for the MCBJ from eq. 2.9 and using the rates for a MCBJ with one unique channel of very low transmission. This is a first test for the master equation approach for the MCBJ-SET.

In section 4.3 we will explain the two methods that we can use for calculating the charging energy E_C of the SET. And last, section 4.4 is dedicated to briefly explain how to calculate the electronic T of the SET on the classical regime.

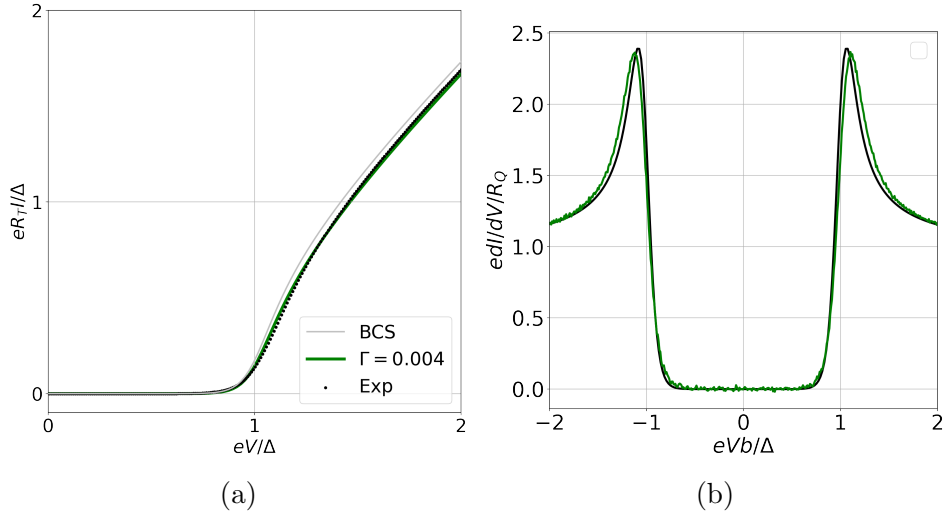


Figure 4.1: Experimental data (black dots) and theoretical current (green line) for a SIN junction. Figure (a) is the $I - V_b$ curve and figure (b) is the differential conductance of the same set of data. As indicated in the legend, the green line is a calculation taking into account a Dynes parameter of $\gamma = 0.004\Delta$ which fits the experimental data much better than the grey line (calculated taking $\gamma = 0$, so the classical BCS result).

4.1 Tunnel barrier characterisation

At this stage we can characterise the superconducting gap. For this it is necessary to measure the tunnel barrier over a large bias, and make a linear fit on the wide bias range on the differential conductance $dG = dI/dV$. Then from the intersection between this fit line and the transition curve for the SC gap it is possible to obtain the superconducting gap Δ . For all samples listed here we obtain $\Delta \sim 182\mu\text{eV}$.

At this point it is also possible to estimate the approximate temperature of the normal metal from eq. (2.2) and the Dynes parameter from eq. (2.3). For this it is not truly possible to make a fit, so we choose the set of parameters that best agree with our experimental data. This would be $\gamma = 0.004\Delta$ and $\beta_N > 20$ (which implies $T \lesssim 100\text{mK}$). For $\beta_N > 20\Delta$ it is not possible to see any difference in comparison with bigger values of β_N . The comparison between theory and experiment is in figure 4.1.

Finally, we also determine the resistance of the junction by doing a simple

linear fit to the $I - V_b$ curve.

4.2 NNN and SSN MCBJ-SET in the classical regime

In this section there are results for the MCBJ-SET in a regime where the MCBJ has a very large resistance (or very low transmission \mathcal{T}). From now on we will show plots like figure (4.2). This is a contour plot of the V_b against V_g (equivalent to n_g), and the contour lines show the linear increment in current (or conductance). Figure (4.2 a) is the measured data for sample I ($R_{TB}=43.25$ k Ω) in normal state with a $R_{BJ}=1216$ k Ω and figure (4.2 b) is the corresponding simulation. In both cases V_b is normalised to the value of E_C and V_g to the values of the coupling between the island and the gate electrode, for giving n_g .

In the normal state, the transport is blocked until the bias voltage overcomes a threshold that is between $V_b=0$ and $\pm 2E_C$ (in each polarity).

The SSN-SET map is in figure (4.3), for the same configuration for the MCBJ as in figure (4.2). In this case instead of showing CB between 0- $2E_C$ (in the positive polarity) it is necessary to overcome first a threshold of 3Δ (2Δ from the SIS junction and Δ from the SIN junction).

Considering the SIS tunnelling rate of eq. (2.9) for a superconducting MCBJ is also a good approximation in this case (what we denominate as tunnelling regime). In the simulation from figure (4.3) (b) this is the rate implemented in the simulation.

As shown in both figure (4.2) and (4.3), when just taking into account electron transport in the SET (no matter if using NN, SN or SS junctions) the agreement between theory and experiment seems to be good when comparing the transport maps.

Finally, we estimate the resistance of the break junction R_{BJ} as follows: first we perform a fit to obtain the R of the MCBJ and the TB in series from the normal conducting (NC) data. For this we need to pick the line that we obtain for $N_g = \pm 0.5$, i.e., when there is no CB and the transport is possible. From the plot 4.2 this would correspond to the cut line at $N_g = 0.5$, and from figure 4.4 it would correspond to the straight curve that crosses the origin. Then we subtract the value of the R_{TB} previously calculated when the MCBJ was not broken. The \mathcal{T} is always calculated as $\mathcal{T}=12.9$ k Ω/R_{BJ} .

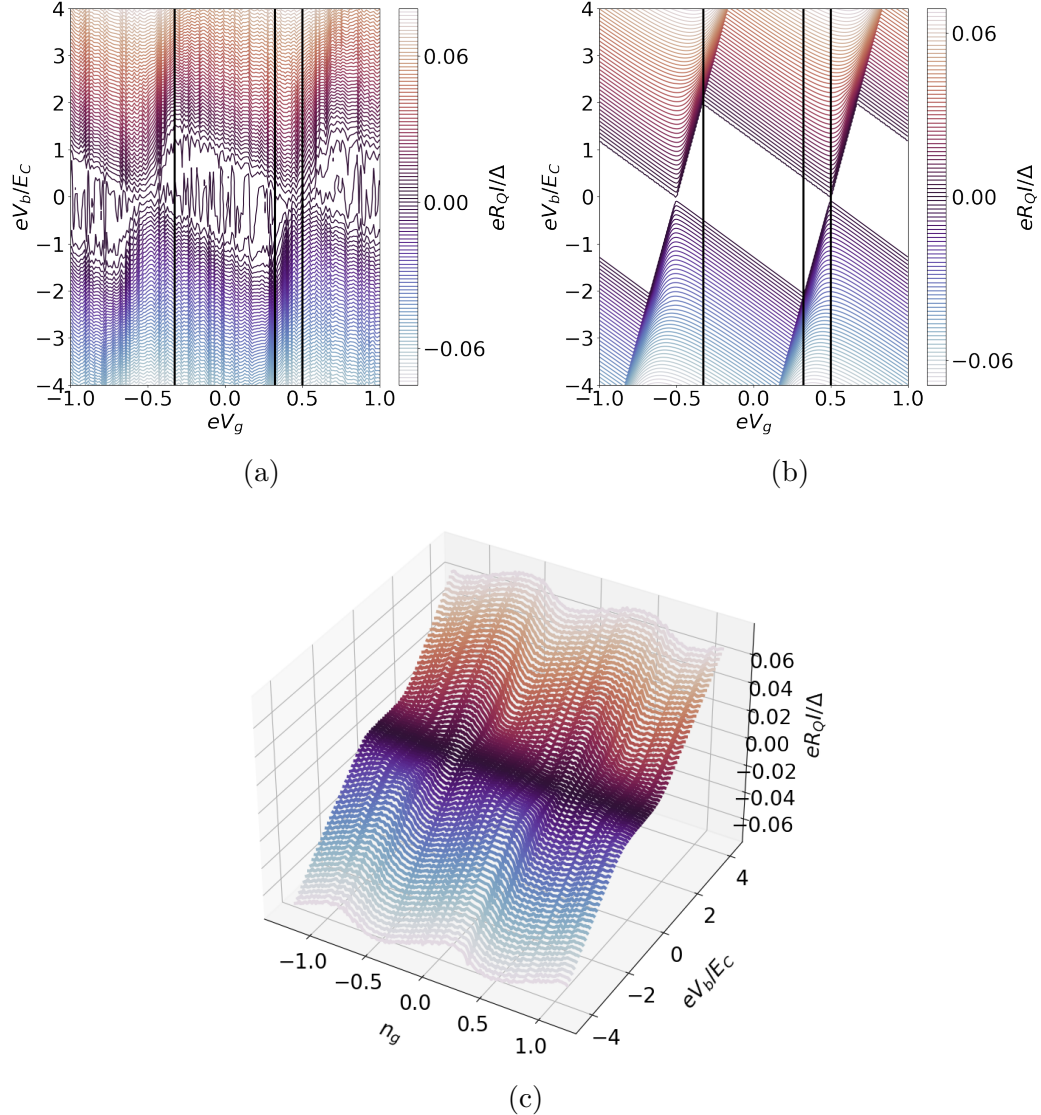


Figure 4.2: Contour plot of $n_g - V_b - I$ for a NNN-SET with $R_{\text{TB}}=43.25$ k Ω and $R_{BJ}=1216$ k Ω : experimental (a) and simulated (b) data. The transport is blocked between $V_b=0$ and $V_b=2 E_C$ depending on the charge of the island, i.e., on the coupling to the gate voltage. The vertical axis is normalised to the value of the E_C , which is $E_C=69.2$ μ V. The black lines represent position of cuts that later we will plot as $I - V_b$ curves in figure 4.4. For clarity, we include a quasi-3d plot in (c) analogous to (a).

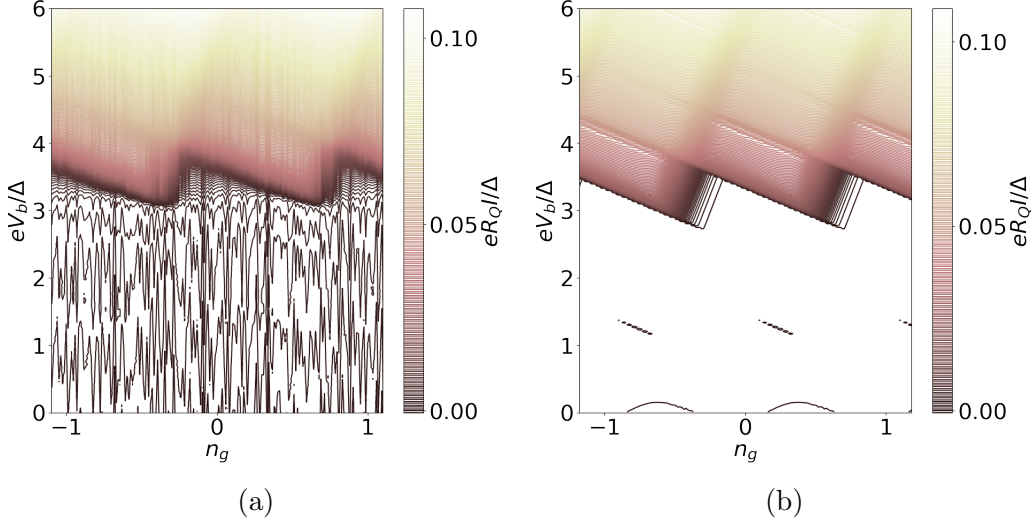


Figure 4.3: Contour plot of $n_g - V_b - I$ for a SSN SET with $R_{TB}=43.25\text{ k}\Omega$ and $R_{BJ}=1216\text{ k}\Omega$: experiment (a) and simulated(b) data. The transport is blocked between $V_b=3\Delta$ and $V_b=3\Delta+2E_C$. Only positive polarity is shown.

4.3 Charging energy calculation

There are several methods for estimating the charging energy E_C of the SET. Here we explain two methods that we use in this thesis, plus two quick ways to check how the agreement is between them.

For the first method we use formula 4.1, derived in [21] and analogous to 2.13:

$$m\kappa_i V(Q_0) = U(n+m) - U(n) + q\Delta = 2mE_C \left[(-1)^{i-1} \cdot \left(\frac{Q_0}{e} - n \right) + \frac{m}{2} \right] + q\Delta \quad (4.1)$$

If we derive eq. (4.1) with respect to V_g , we obtain eq. 4.2 :

$$\kappa_i = 2 \cdot s \cdot E_C \frac{(-1)^{(i-1)}}{V_g} \quad (4.2)$$

Where 's' refers to the slope of the diamonds that can be estimated from the plots. Since the capacitance divisors of the SET must sum up to 1, we have

$$\kappa_{TB} + \kappa_{BJ} = 2 \cdot (s_{TB} + s_{BJ}) \cdot \frac{E_C}{V_g} = 1$$

where we can easily clear the E_C . This allows to estimate the E_C also from the superconducting maps.

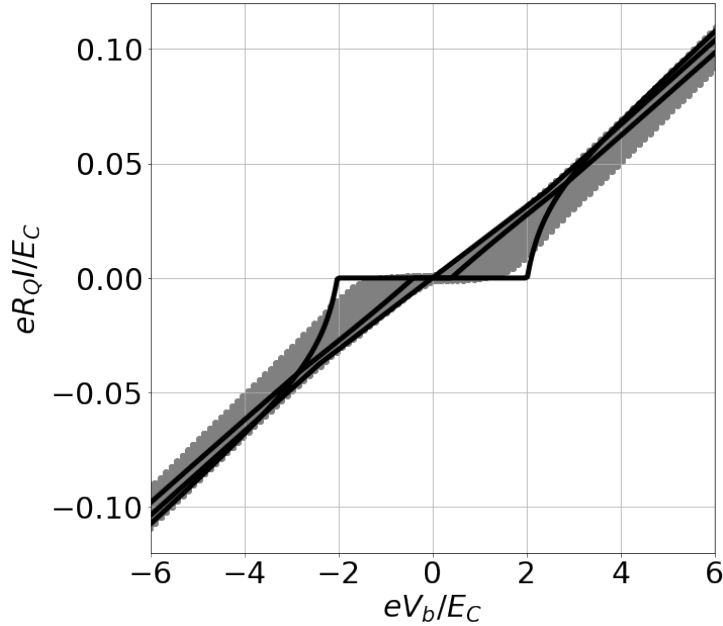


Figure 4.4: Plot including all $I - V_b$ curves for all gate values of figure 4.2(a) as grey dots. The black solid lines are cuts from the simulation from the highest values of the diamonds (as indicated in figure 4.2, so it would be the 'envelope' that indicates the maximum values of the blockade area. This means that the transport for these lines starts at $V_b = \pm 2E_C$.

$$E_C = \frac{V_g}{2} \frac{1}{s_{TB} + s_{BJ}} \quad (4.3)$$

The second method consists on sweeping quickly the gate voltage V_g while sweeping slowly V_b for obtaining the so-called envelope curve where the current oscillations show the minimal and maximal values [2][7]. We have not performed such measurement, but an equivalence would be to plot all the measured $I - V_b$ for a wide range of V_g [36]. Then, by solving the master equation with the E_C estimated with the previous method it is possible to corroborate the E_C , since the curves should create an envelope for the data that fits with the width on the V_b axis. This method is plotted on figure 4.4. This is a $I - V_b$ plot, where the grey dots are experimental points for

all different gates V_g of a contact with $R_{BJ} = 1216 \text{ k}\Omega$, and the black lines are the cuts from figure 4.2(b) at values of $N_g = \pm 0.4$ (the 'maximum' and 'minimum' of the diamonds) and for $N_g = 0.5$ (point where the CB is zero and transport is possible for all the range of V_b). The fit to the cut at $N_g = 0.5$ fits our experimental data (straight line that goes through the origin). However, already at this low T , there is a rounding for values of V_b close to $2E_C$. This is due to co-tunnelling (see section 5.1) and it would allow us to compare the excess current caused by this phenomena. For higher transmission contacts the co-tunnelling will make more complicated to determine the value of E_C by any of the methods, as we will explain in section 5.1.

Finally, two quick checks that we can make to assure that the values calculated following these methods make sense and are consistent: as we could see in figure 2.6 (c) the peaks of the diamonds on the V_b axes are at a distance of $4E_C$. From table 2.2 we know that each process starts at a very specific threshold that depends on Δ but also on E_C . In both cases, by inspecting the maps, we can estimate the value of E_C and verify if it agrees with the values that we calculated with the two previous methods.

4.4 Temperature estimation

The CB on the SET can be used for estimating the electronic temperature [62] [63] of the circuit. For calculating the temperature of the SET we follow the protocol explained in [12].

For this, we need to obtain the full width at half maximum (FWHM) for the Coulomb peak of the conductance dG plotted against the bias voltage. The Lorentz distribution (eq. 4.4) fits this peak; we use the following formula:

$$f(x) = a + \frac{1}{b \cdot \left(1 + \left(\frac{x-c}{d}\right)^2\right)} \quad (4.4)$$

where a, b, c, d are free parameters of the fit. We are only interested in the parameter d , since $\text{FWHM} = 2d$. Then the temperature is:

$$T = \frac{e \cdot \alpha \cdot \text{FWHM}}{3,525 \cdot k_B} \quad (4.5)$$

where $\alpha = Cg/C$, being C_g the capacitance of the gate and $C = C_\Sigma$ is the sum of all capacitances from the SET. We know C_g from the periodicity of

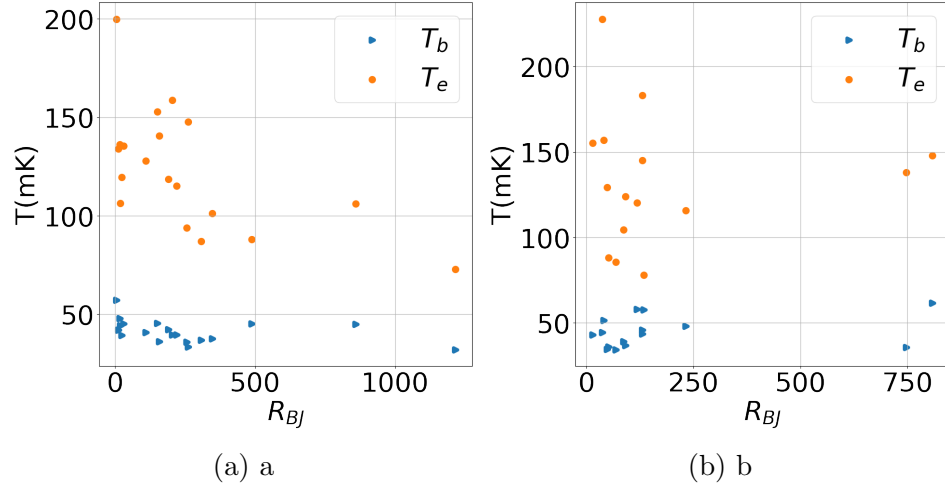


Figure 4.5: Plots for comparison of the bath and electronic temperature for sample I (a) and sample II (b). The electronic temperature is bigger in all cases, as expected. In sample I, since R_{TB} is above R_Q the tendency of both plots is more similar than for sample II where $R_{TB} < R_Q$

the Coulomb oscillation since $C_g = e/V_g$ and C_Σ from the charging energy value. Therefore it is possible to estimate the electronic temperature of the sample in principle for each contact configuration (see appendix A). This data is plotted for sample I and sample II in figure 4.5. The electronic temperature is systematically bigger than the bath temperature, as expected. The tendency of the electronic and bath temperature for different contacts is more consistent for sample I because for this one $R_{TB} > R_Q$. For sample II, specially for contacts with a low R , the values of the electronic temperature don't seem to be truly correlated to the bath temperature. We need to keep in mind that this method for calculating the electronic temperature is just valid for the orthodox regime, so the values for $R < 25.8 \text{ k}\Omega = R_Q$ are not trustful. However, this can be used for getting an approximate estimation of the electronic temperature even for values with a low resistance.

Chapter 5

Vanishing of the CB in the MCBJ-SET

As we mentioned in the introduction, by adjusting contacts with a high transmission it is possible to study the strong coupling regime of the SET. This would be the focus of this chapter. Since for now we are mostly interested in discussing the charging effects and how they evolve for different \mathcal{T} , we will mainly focus on the normal state measurements, i.e., the NNN-SET.

The chapter starts in section 5.1 discussing the co-tunnelling effect: what it is, and how it shows and affects our measurements. We will show examples of excess current in the diamond region of the CB, both in the NNN and SSN-SET.

In section 5.2 we will present our results for all measured contacts of our 3 samples. We will first explain how we can see the CB oscillations vanishing, and afterwards we will present two analysis (analogous to previous publications [50] and [64]) that demonstrate that also in our case the charging effects vanish for high conductance and \mathcal{T} .

In section 5.3 we will briefly discuss the renormalisation of the charging energy and in section 5.3.1 we present the effect that remains when $\mathcal{T} > 1$, the dynamical Coulomb Blockade.

5.1 Co-tunnelling in the SET

Until now we have just considered sequential processes that would charge/decharge the island of the SET with one particle. However, if a particle doesn't

have enough energy to overcome the charging energy it is still possible that it tunnels through the SET due to co-tunnelling [45][65] [66][67]. This can be either elastic or inelastic: in elastic co-tunnelling a particle would tunnel to the island through the left junction and leave it through the right junction within a time that would be smaller than the Heisenberg uncertainty time $t_H \sim \hbar/E_C$ [6]. This particle would not have to pay for any extra charging energy and would not lose any energy in the process. For inelastic co-tunnelling, a particle would tunnel to the island and within the time t_H , another particle from the island would tunnel off via the other junction.

The probability of having co-tunnelling comes from the condition that $\Gamma t_H \ll 1$. Multiplying the chances for both junctions, we would obtain:

$$\Gamma_{\text{cot}} \sim \Gamma_R \Gamma_L \frac{\hbar}{E_C} \quad (5.1)$$

An approximation for the rate of single electron would be $\Gamma_e \sim \frac{1}{RC} = \frac{E_C}{Re^2}$, which allows us to rewrite the previous expression as:

$$\Gamma_{\text{cot}} \sim \Gamma_e \frac{R_Q}{R} \quad (5.2)$$

This approximation can be improved by taking into account the energy conservation in this state [6], which would reduce the number of states available by a factor $\sim (eV_b/E_C)^3$. This in our case would give:

$$\Gamma_{\text{cot}} \sim \frac{R_Q}{R_{\text{TB}}} \frac{R_Q}{R_{\text{BJ}}} \left(\frac{eV_b}{E_C} \right)^2 \text{eV} \quad (5.3)$$

The factor $(eV_b/E_C)^2$ makes that the co-tunnelling is more likely to happen at bias voltages that are $V_b \sim E_C$, and less likely for values of the bias voltage that are $eV_b \ll E_C$. On the other side there are the factors of R_Q/R : in our case sample I has a $R_{\text{TB}} = 43.25 \text{ k}\Omega$, sample II has a $R_{\text{TB}} = 23.6 \text{ k}\Omega$ and sample III has a $R_{\text{TB}} \sim 17.85 \text{ k}\Omega$, so all of them are in the order of R_Q , and specially for sample II and sample III $R_{\text{TB}} \sim R_Q$. Besides, while tuning the MCBJ we also go to values of $R_{\text{BJ}} < R_Q$. Therefore in this cases we will measure an extra current in the areas close to $eV_b \sim E_C$.

These features are visible both in the normal conducting map and in the superconducting map. In figure 5.1 (a) there is an experimental normal conducting (NC, measured after applying a magnetic field of 50 mT for cancelling the SC of Al) map for sample I with $R_{\text{TB}} = 43.25 \text{ k}\Omega$ and $R_{\text{BJ}} = 18.55 \text{ k}\Omega$, so a rather low resistance that will correspond to a \mathcal{T} of 0.7. Figure (b) is

the corresponding simulation without taking into account any co-tunnelling events. For these values, the pre-factor from eq. 5.3 will be approximately 0.83, therefore eq. 5.3 becomes $\Gamma_{\text{cot}} \sim \left(\frac{eV_b}{E_C}\right)^2 \text{ eV}$. This agrees with the measurement of figure 5.1 (a): while in the simulation the transport doesn't start between values of 0 and $2E_C$ (white area), in the experiment there is some transport contribution starting at around E_C . This is also visible when we plot the $I - V$ characteristics from all gate values (figure 5.1 (c)). The black lines are the simulation for the values when the transport starts at $2E_C$ (analogous to figure 4.4)). In comparison with this figure, we can see here that the small rounding around $2E_C$ that we had in figure 4.4, already starts at smaller values for V_b (around E_C) and that the excess current is much bigger in this case.

This result means that even for our sample with the biggest R for the TB we will have contributions from co-tunnelling, specially while studying contacts with a $\mathcal{T} \sim 1$.

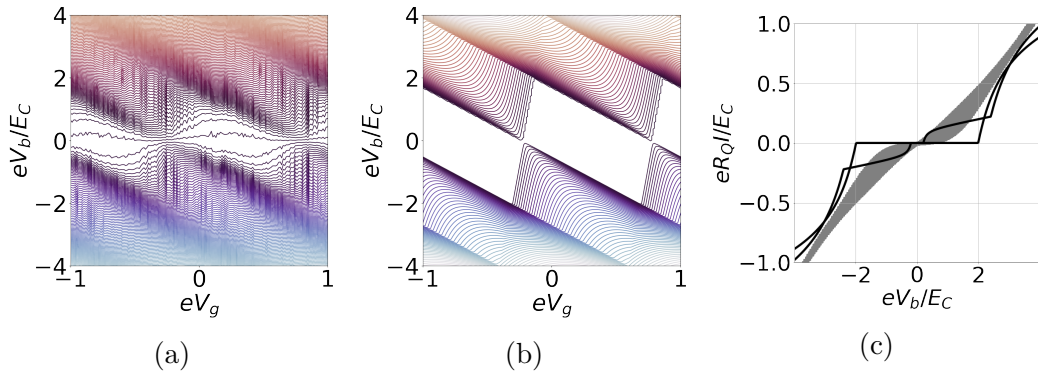


Figure 5.1: Experimental NC map for sample I with $R_{\text{TB}} = 43.25 \text{ k}\Omega$ and $R_{\text{BJ}} = 18.55 \text{ k}\Omega$ (a) and simulation for the same R , $\kappa_{\text{BJ}} = 0.911$ and $E_C = 0.39\Delta$ ($\sim 71 \mu\text{eV}$) (b). The shape of the diamond agrees between experiment and theory, although above $\sim E_C$ there is an excess current in the experimental data due to co-tunnelling according to eq. 5.3 that is not included in the simulation. Figure (c) is a plot of all the experimental $I - V_b$ characteristics for every V_g (grey dots) and an envelope taking the simulation data for the values of V_g where the transport starts at $2E_C$ in the fully blockade situation.

These co-tunnelling features are also visible in the superconducting map

(SC, no magnetic field applied), but now the co-tunnelling of the single electron starts to be possible after 3Δ (figure 5.2, dashed line). This are experimental records for sample III with a $R_{\text{TB}} = 17.85 \text{ k}\Omega$ and different values for R_{BJ} in decreasing order. The current measured between 3Δ and $2E_C$ increases for lower resistances, and this shows in a higher density of contour lines around this area when comparing figs 5.2(a) and 5.2(c).

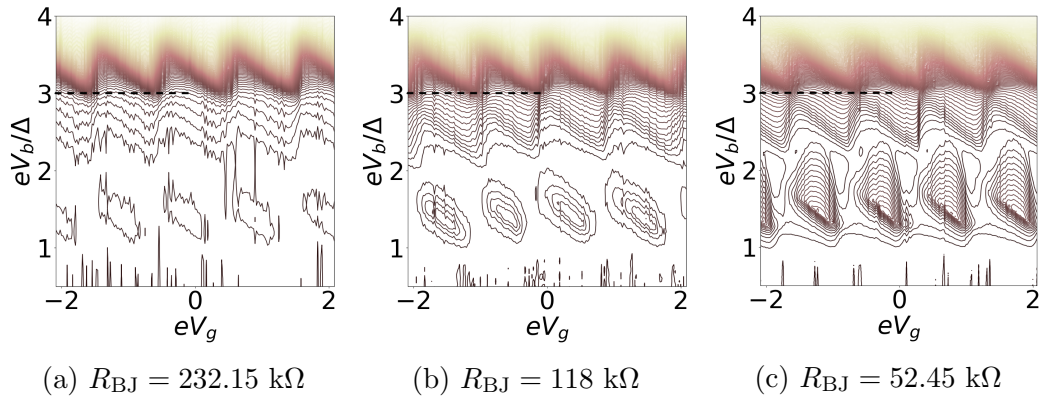


Figure 5.2: Experimental normalised SC maps for sample III with $R_{\text{TB}} = 17.85 \text{ k}\Omega$ and R_{BJ} indicated in the sub-caption. The co-tunnelling contributions are more visible for lower R after 3Δ (dashed line in the maps).

On the other side, for elastic co-tunnelling the estimation from eq. (5.3) would become:

$$\Gamma_{\text{cot}} \sim \frac{G_L G_R}{G_Q} \frac{\delta_S}{E_C}$$

where δ_S is the spacing of the electron states in the island. Since the island in our SET is quite big ($2\mu\text{m} \times 2\mu\text{m}$), we assume that the contribution from this type of co-tunnelling to the transport is negligible.

5.2 Vanishing of the Coulomb blockade for high \mathcal{T} channels

Coulomb blockade is expected to vanish if one channel from any of the junction has a $\tau = 1$ [57] [68]. Reaching this limit with the MCBJ technique is possible by closing it and adjusting a total $\mathcal{T} \gg 1$.

In figure 5.3 there are three plots where it is shown how the CB modulation vanishes for higher \mathcal{T} . The three plots represent the normalised G/G_0 (where $G_0 = 1/(R_{\text{TB}} + R_{\text{BJ}})$) versus the applied gate voltage V_g on the island for a constant bias voltage V_b . On figure 5.3(a) there is a measurement of the CB peak for a contact with a very low \mathcal{T} . The baseline of this peak is around zero and its maximum reaches $0.5 G/G_0$, in agreement with theory predictions for the classical regime [69].

If the \mathcal{T} has a much bigger value (figure 5.3(b)), the minimum of the graph is not zero anymore. The baseline is also expected to have $G/G_0 \neq 0$ for high temperatures. The peak becomes wider and the difference between the maximum and the minimum conductance is smaller than in the low \mathcal{T} regime. This agrees with previous results [57] [50] [51], although in this case, the total $\mathcal{T} > 1$ and we still measure the CB oscillations. We attribute this to the fact that in the junction there are several individual channels (for Al single atom contacts there are three channels [58]) that sum up to the total \mathcal{T} . Therefore, although $\mathcal{T} > 1$, there is not necessarily an individual channel with $\tau = 1$.

In the last case, there are no further signatures of the CB oscillations: independently of the applied gate voltage, the conductance has always the same constant value. In this case, since the total \mathcal{T} is well over 1, and we measure no further Coulomb signatures, we can assume that there is at least a single channel with a $\tau = 1$.

A better representation for representing how these peaks vary for the different possible \mathcal{T} is figure 5.4. This is a plot of the maximum conductance (grey squares) and the minimum conductance (black triangles) against the \mathcal{T} of the point contact. Each of the plots corresponds to a different sample with a different R_{TB} , as specified in the legend.

Figure 5.4(a) corresponds to sample I with $R_{\text{TB}} = 43.25 \text{ k}\Omega > R_Q$, (b) to sample II with $R_{\text{TB}} = 23.6 \text{ k}\Omega \sim R_Q$ and (c) to sample III with $R_{\text{TB}} = 17.9 \text{ k}\Omega < R_Q$. Figure (a) corresponds to the classical case: constant values for G_{max} and G_{min} until a value of \mathcal{T} close to 1, where the minimum value starts to increase and they become the same for $\mathcal{T} \gg 1$. For figure (b) the minimum is already higher than 0 from the beginning. This is most likely because all the measurements of sample II were at T of around 100 mK for the bath temperature at the sample stage. This agrees with previous T dependent measurements ([50]). Finally, for sample III the maximum for the conductance is around $G/G_0=0.2$ for the low transmission contacts, below 0.5 as theoretically predicted for the classical case, due to the low value of

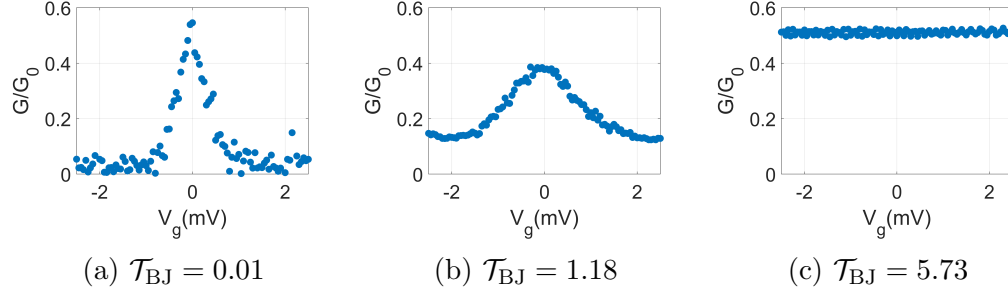


Figure 5.3: Normalised conductance plots for different MCBJ contacts, from the tunnelling regime (a) to a perfect contact with transmission $\mathcal{T} \sim 1$ (b). In figure (b) the CB peak is still visible, although its amplitude and base line are smaller in comparison with (a). It is necessary to adjust bigger \mathcal{T} contacts for the CB to vanish (c). All of these contacts are from sample I, with $R_{TB} = 43.25$ k Ω . The \mathcal{T} is calculated as $\mathcal{T} = 12.9$ k Ω/R_{BJ} .

the R_{TB} . For this sample we did not measure a contact with a very high \mathcal{T} , so we cannot check if the CB oscillations vanish in this case.

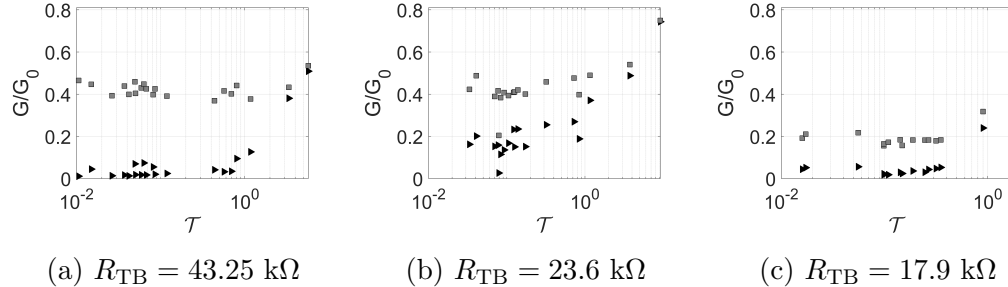


Figure 5.4: Renormalised conductance for different MCBJ transmission contacts for sample I (a), sample II (b) and sample III (c), with decreasing R_{TB} . The maximum of the CB peak are the grey squares and the baseline/minimum are the black triangles. The minimum-maximum on figure (b) are higher than expected due to the high bath temperatures. In figure (c) the maximum doesn't reach a value of 0.5.

Finally, an equivalent way of plotting the data from figure 5.4 for comparing all the samples in a plot is fig. 5.5. We follow [57] and first calculate

ΔQ as:

$$\Delta Q = \frac{G_{\max} - G_{\min}}{G_{\max} + G_{\min}} \quad (5.4)$$

Figure 5.5 is ΔQ for every sample as indicated in the legend against the transmission of the MCBJ (inserted plot). The bigger plot is the same but on a log-log scale. Eq. 5.4 is a measure of how far away G_{\min} is from the baseline at 0, and also on how different are G_{\min} and G_{\max} . Therefore, for the classical case we expect to have $G_{\min} \rightarrow 0$ and therefore $\Delta Q \rightarrow 1$. For higher conductance the maximum and minimum of the Coulomb oscillations will become closer and then $\Delta Q \rightarrow 0$.

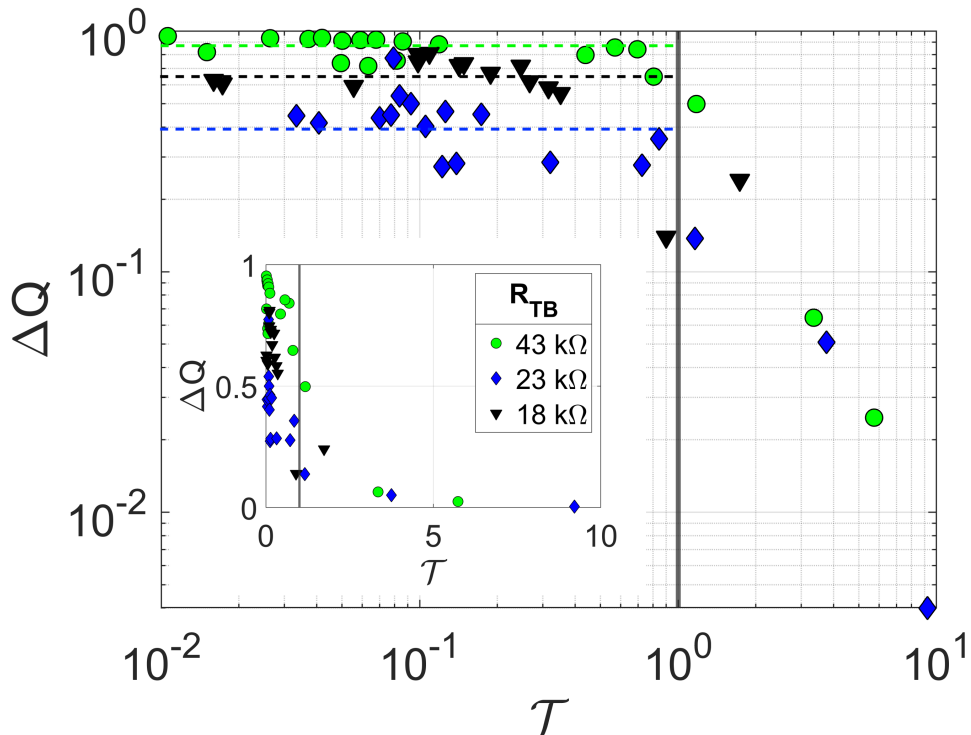


Figure 5.5: ΔQ data for the three different samples with different R_{TB} as indicated in the legend. The insert plot is in a normal scale where as the main one is the same but in a log-log scale. The dashed horizontal lines are a guide to the eye to the baseline of the respective samples (same colours as the scatter plot).

The first remarkable result from figure 5.5 is that ΔQ doesn't collapse immediately to zero (values below 10^{-1}) when reaching a total transmission $\mathcal{T} = 1$ (grey lines on both plots). This is achieved when \mathcal{T} is much higher than the unit. This shows again what we claimed before, although $\mathcal{T} > 1$ there is not necessarily a single channel with $\tau = 1$. On the other hand, the baseline of the sample I ($43\text{ k}\Omega$, green dots) is around 1, according to what we explained before. However, the other two samples have their baseline below 1. In sample II ($23\text{ k}\Omega$, blue diamonds) this agrees with the fact that the T when measuring was higher than for the other two samples. And for sample III ($17.9\text{ k}\Omega$, black triangles) this baseline it is just a little bit below 1, which is expected when $R_{\text{TB}} < R_Q$ and the conductance of the TB becomes higher. As shown in [57], both high temperatures and high transmission contacts contribute to the disappearance of the CB peak, and this is what we indeed measure in sample II and III.

5.3 Re-normalisation of E_C

Following the different methods that we describe in section 4.3, we can estimate the charging energy for each of the configurations of the MCBJ. This task becomes more challenging for contacts that have a $R \sim R_Q$, because of the co-tunnelling excess current that we mentioned in the previous section. This makes it hard to estimate if the rounding and excess current is due to a increase of the co-tunnelling current or because of actual reduction of the charging energy E_C .

It is always possible to simulate the normal-conducting map as we showed in the previous section 5.1. Then by inspecting the shape of the diamonds and comparing the single $I - V$ characteristics, it is possible to estimate how does the charging energy changes and how the co-tunnelling current changes over the different coupling regimes.

The actual capacitance of the atomic contact from the MCBJ is very small, on the order of aF (10^{-18} F) [70]. The capacitance of this junction will be dominated by the shape and size of the leads that are around the atomic contact [14], and it can increase its value by three orders of magnitude until $\sim \text{fF}$. In our case indeed, the coupling to the gate brings a capacitance of $C \sim 0.04\text{ fF}$, and the total C of the SET is 1.2 fF , being $C = C_{\text{BJ}} + C_{\text{TB}} + C_g$. Since $C_g \ll C$, we can approximate $C_i \sim \kappa_i C$, and therefore $C_{\text{BJ}} \sim 1.1\text{ fF}$ in agreement with previous works on single MCBJ [14]. It is not clear if

the capacitance of this atomic contact should change much while adjusting different atomic contacts, because the surrounding of the MCBJ should not change.

If we assume that the C of the junction is not changing, the only free variable in eq. 4.3 of E_C is the coupling of the gate to the island. This value doesn't change for different R_{BJ} .

Therefore, from our data we cannot assure to see any change on the charging energy determined from the slopes of the diamonds for values with $R_{BJ} > 12.9 \text{ k}\Omega$, so when it is clear that there is no channel with $\mathcal{T}=1$. When closing the MCBJ there is point when the $R_{BJ} \ll 12.9 \text{ k}\Omega$ when we stop seeing any diamonds on the $V_g - V_b - I$ map, in other words, no further modulation from the gate electrode. However, we still measure a CB peak. This is known as dynamical CB (see next subsection 5.3.1).

5.3.1 Dynamical Coulomb blockade

As shown in [64], when having a perfect ballistic channel any signal from Coulomb blockade oscillations vanishes (figure 5.3 (c)). However, the signs of quantisation are still present in the $I - V_b$ characteristics as the dynamical Coulomb blockade [71].

As shown in figure 5.6, the diamonds that we previously measured are now gone and there is just a small plateau around $V_b = 0$. This has no modulation or change function of the gate voltage. This is more obvious when looking at the differential conductance from figure 5.6 (b). In both of those graphs the total transmission is well above 1, which suggests that one of the channels is a ballistic contact. It is interesting to point out that for a bigger \mathcal{T} the amplitude of the dynamical CB peak is smaller.

Also, since in this regime there is no modulation coming from the gate and also there is no visible diamond, we can confirm that when there is a ballistic channel the charging energy gets re-normalised [56] [65] [72] [73] [74]. If it still has a finite value, it would be so small that we cannot resolve it from our measured data, since it is not possible to distinguish any diamond shape from figure 5.6 (a).

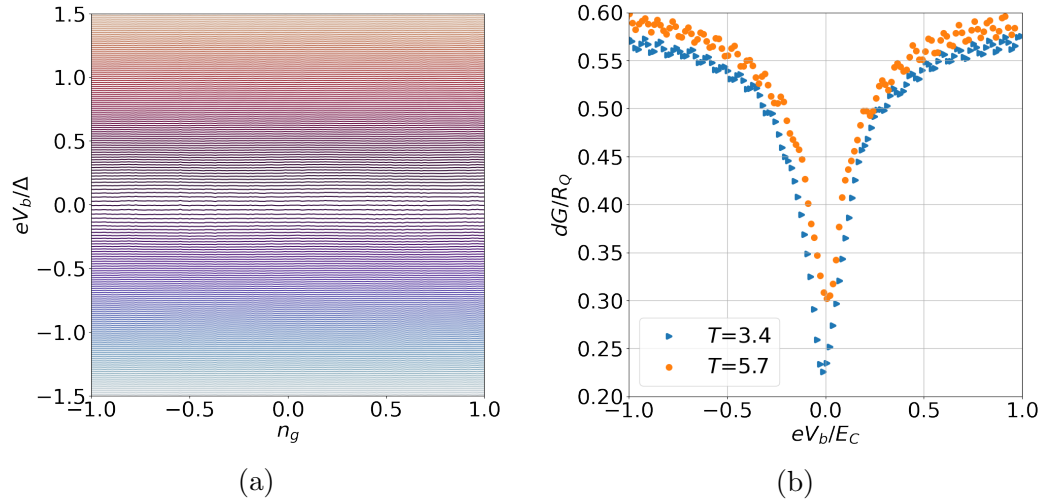


Figure 5.6: Experimental data from sample I with $R_{\text{TB}} = 43.25 \text{ k}\Omega$. The transmission for the MCBJ of the map in figure (a) is 3.4. The two graphs in panel (b) correspond to two different contacts with a different value for the \mathcal{T} of the MCBJ, as indicated in the legend.

Chapter 6

Interplay between MAR and charging effects

This chapter focusses on the superconducting state of the SET, i.e., on the results for the SSN-SET. First, we will focus in section 6.1 on analysing single $I-V_b$ for different contacts. By comparing the different thresholds for different transmissions of the MCBJ, we will be able to recognise the different processes. It is also a quite visual and simple demonstration that new processes appear in the gap region for different contacts, as well as we can study how the amplitude of each of these signatures evolves.

As explained in section 2.4, the master equation approach can be extended for multi-particle processes in order to account for the Andreev and multiple Andreev contributions. The next sections will treat about proving in a more systematic way the description of the first section. Therefore, section 6.2 is focussed on the low coupling regime ($\mathcal{T} \sim 0.01$ for the MCBJ), section 6.3 treats contacts that start to show MAR signatures but that still have a low \mathcal{T} of around 0.1-0.5. Section 6.4 focuses on contacts that have a higher \mathcal{T} and that show multi particle processes. And finally section 6.5 treats the strong-coupling regime, i.e., contacts with $\mathcal{T} > 1$.

6.1 Multi-particle processes signals in the $I - V_b$ and the $dG - V_b$ characteristics

First, we will discuss how by inspecting the $I - V_b$ characteristics of our measurements we can identify the different processes just by analysing the

threshold where they start. The signatures of (M)AR-QP processes, as well as the JQP, will appear in the inner gap of the SSN-SET, this means, between Δ and 3Δ . In figure 6.1 we show several curves of the conductance dG as function of V_b for different coupling of the MCBJ to the island. All the plots are taken at gate voltages corresponding to the minimum CB, i.e. at the lowest corner of the diamonds, so the comparison between the different peaks is consistent. This is a good representation for visualising the amplitude and relevance of each process while increasing the transmission of the MCBJ. We plot separately the down- (in fig. 6.1(a)) and up-sweep (fig. 6.1 (b)) curves, and the superposition of both in figure 6.1(c).

Starting from the top plot, we just measure what we would expect for a classical SET with high values for R_{TB} and R_{BJ} : no transport until some point between 3Δ and $3\Delta + E_C$ when e transport starts to be possible. Up- and down-sweep overlap perfectly in 6.1(c).

For lower values of R_{BJ} (the three next values, 157 k Ω , 75 k Ω and 41 k Ω) we see how the features inside the window of $\Delta - 3\Delta$ grow in amplitude for lower R_{BJ} . The first feature starting between Δ and 2Δ is, according to table 2.2, a JQP, which is expected to start at $\Delta + E_C$. The shape of a peak followed by a negative differential conductance confirms it, since this is a signature of a resonant feature.

After this, between 2Δ and 3Δ , there is a feature that we identify as an AQP. This is a peak that is not followed by any negative differential conductance, and it is starting after $2\Delta + E_C$ according to table 2.2.

The superposition of both up- and down-sweep in figure 6.1(c) shows that there is a hysteresis in the JQP. This hysteresis increases as the \mathcal{T} of the MCBJ becomes larger, and it is not limited to the JQP position, but it also affects other peaks at higher voltages, making the amplitude of the AQP smaller in some contacts. This means that for certain contacts some of the features in the experimental data will be hidden by this hysteresis of the up-sweep. This hysteresis is a signature of under-damped SIS Josephson junctions as a consequence of cp transport [75].

In these three plots there is a peak after 3Δ which corresponds according to table 2.2 to single-electron transport. If we now go one graph below ($R_{BJ} = 18$ k Ω) following this same line at 3Δ , we can see that this peak has vanished. On the other hand, the peaks inside the gap are bigger in amplitude, especially the AQP. This means that for higher \mathcal{T} the processes that transport multiple particles are dominant over single-electron transport.

In the up-sweep for the positive bias voltage, there are some features that

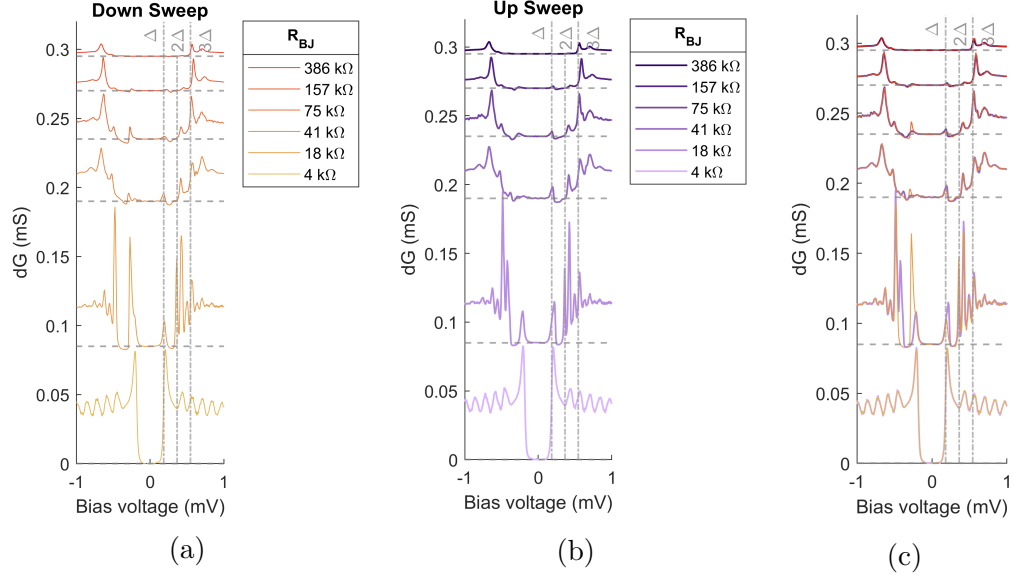


Figure 6.1: dG - V curves for different contacts with different R_{BJ} as indicated in the respective legends for sample II with $R_{TB} = 23.6 \text{ k}\Omega$. The cuts are made at a gate for the lowest value where the diamond starts, so it is possible to compare all different coupling strengths. The scale is in the measurement units the vertical lines indicate the different values of Δ , and the grey dashed horizontal lines indicate the origin value for each curve. Figure (a) is the down sweep, (b) is the up sweep and (c) is the superposition of both plots.

are covered by this hysteresis, but that show up in the down-sweep at around 2Δ .

Finally, for very low values of R_{BJ} , there is a peak at Δ and an oscillatory behaviour starting after 2Δ . This plot is not the same for all the values of the gate voltage applied, because the position of these small oscillations changes depending on the applied gate voltage (see section 6.5) contrary to what we saw for the normal case in figure 5.6.

In the next section we will analyse case by case all the different coupling strengths summarised here. We will start by the low-coupling regime where the R_{BJ} is very high in section 6.2. This case will be very similar to what we already discussed in section 2.3.4.

6.2 Low-coupling regime

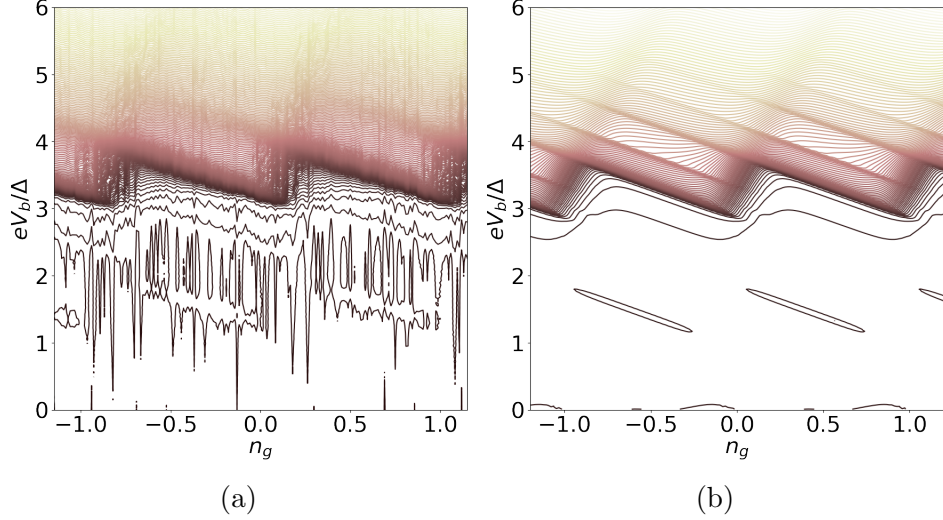


Figure 6.2: Measured (a) and simulated map (b) for a low transmission using the rates for a MCBJ.

Analogous to what we did in section 4.2, we can compare the experimental data to simulations considering a point contact with a very low transmission \mathcal{T} . The results from this comparison are shown in figure 6.2, where we use a channel with transmission $\mathcal{T}=0.025$ for the MCBJ, and the corresponding set of data where the R of the MCBJ is $489\text{ k}\Omega$.

This is only a slightly stronger coupling than what we presented in section 4.2, but nonetheless, there seems to be an extra line on top of the single-electron process that doesn't appear in our experimental data. This line is due to a MAR of order 2,i.e., the transport of two electron. The possible explanation for this extra line is that we are assuming here that a MCBJ with a R of $489\text{ k}\Omega$ has only one channel, which gives an upper bound to the amplitude of the Andreev contributions for all orders. An example to illustrate this is in figure 6.3: they represent a single channel (6.3(b)) with a defined \mathcal{T} , and divided in two channels with τ_i that sum up to the same total \mathcal{T} (6.3(a)).

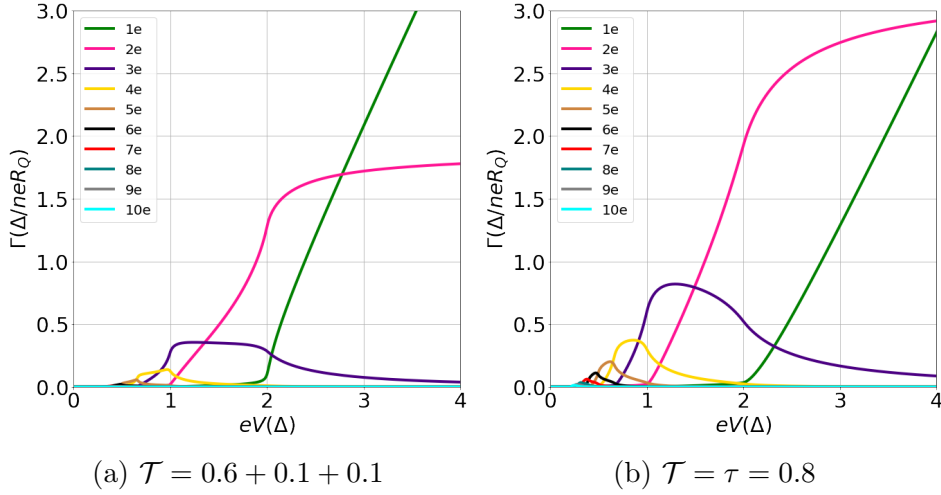


Figure 6.3: Plots for the rates of contacts with a total transmission of $\mathcal{T} = 0.8$, but in (a) they are divided in two individual transmissions coming from three channels ($\tau = 0.6$ plus two channels with $\tau = 0.1$). The amplitude of single electron transport is the same in both plots, but the amplitude of higher order of MAR is smaller in (a).

The amplitude of single-electron tunnelling is in principle the same for both plots. However, it is quite remarkable that the amplitude of MAR of all orders in sub-figure 6.3(a) is significantly smaller than in sub-figure 6.3 (b) for all the cases. And not just that, but also the kinky shape of each of the contribution looks very different. Therefore, depending on the configuration of the channels, the final map after using these rates in the master equation cannot just have a different amplitude, but also look different and show different lines in the $I - V_b - V_g$ maps. Although for these low \mathcal{T} contacts there should not be several channels but just one with very low τ , some works [76] have also shown that even for contacts with low \mathcal{T} several channels must be taken into account.

6.3 Higher-order processes in the intermediate coupling regime

As we have already seen in figure 6.1 for contacts that have lower resistances than in the previous cases but still way above R_Q , some new signatures start

to appear inside the gap region between Δ and 3Δ . In this section we aim to better understand these features by giving a more complete analysis via the results from the master equation approach.

In figure 6.4 we show such an analysis. Figure 6.4(a) is the experimental data for a contact with $R_{BJ} = 158 \text{ k}\Omega$, as indicated in the title. Sub-figure (b) is the corresponding simulation of this data, with $\mathcal{T} \sim 0.08$. By inspecting these two pictures, it is possible to check that there is qualitative agreement between experiment and theory: first, the feature starting at $\Delta + E_C$ that goes until approximately $\Delta + 3E_C$, corresponds to a JQP. The next sub-gap feature starts at $2\Delta + E_C$ and doesn't stop, but becomes covered by the next process starting at 3Δ . This are, respectively, an AQP and a single e-e process. In comparison with the previous figure 6.2 in the low-coupling regime, it is remarkable that there are new process between Δ and $3\Delta + 2E_C$, and this is exclusively a consequence of increasing the coupling of the MCBJ.

The black lines in the maps indicate the cuts at constant gate voltage that are shown in figures 6.4 (c) and (d). In these plots, the black lines are the measured data, the grey line is the simulation and the different colour scatter plots are the individual contributions to the simulated current. In green the single electron transfer, in pink the Andreev reflection, in purple the multiple Andreev reflection of order 3 and in blue the cp are shown as indicated in the legend. This allows us to assign the peaks to the different processes. According to what we explained before, the first peak corresponds to a JQP, and from this perspective it is possible to see its resonant behaviour. Next, the small current contribution that comes at 2Δ is due to the start of Andreev reflection. And after 3Δ , single-electron transport starts to be possible and this together with AR sums up to the total current.

Although in the measured data from figure 6.4 it was not possible to reproduce the exact shape of the $I - V_s$ as shown in the simulation, and although the amplitude of the JQP is visibly lower on the measurement, we can say that there is a good agreement between the two lines in sub-figures (c) and (d). It is most certainly safe to conclude that the excess current starting after 2Δ for both subplots 6.4 (c) and (d) is due to a contribution of MAR of order 2. Besides, the roundness of the single electron process between 3Δ and $3\Delta + 2E_C$ in the experimental data can come from the same MAR contribution of order 2 at higher bias voltages. MAR of order 3 shows a small feature in the simulated data, that we could not distinguish in our measurements.

Figure 6.4 represents a contact where we start to see some signature of

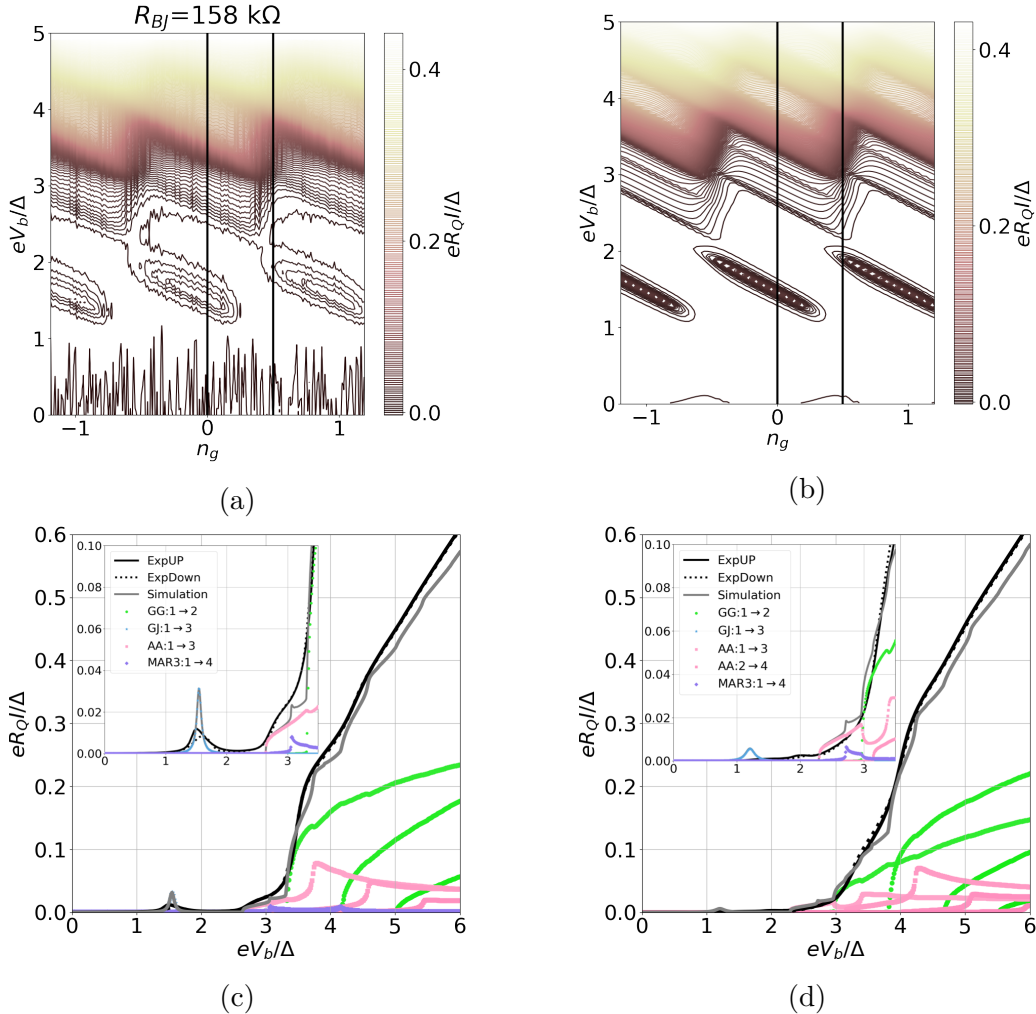


Figure 6.4: Experimental (a) and simulated (b) results for a contact with $R_{BJ} = 158 \text{ k}\Omega$ and $T = 0.08$. The two black vertical lines indicate the two cuts at constant gate voltage that are plotted in figure (c) and (d), respectively.

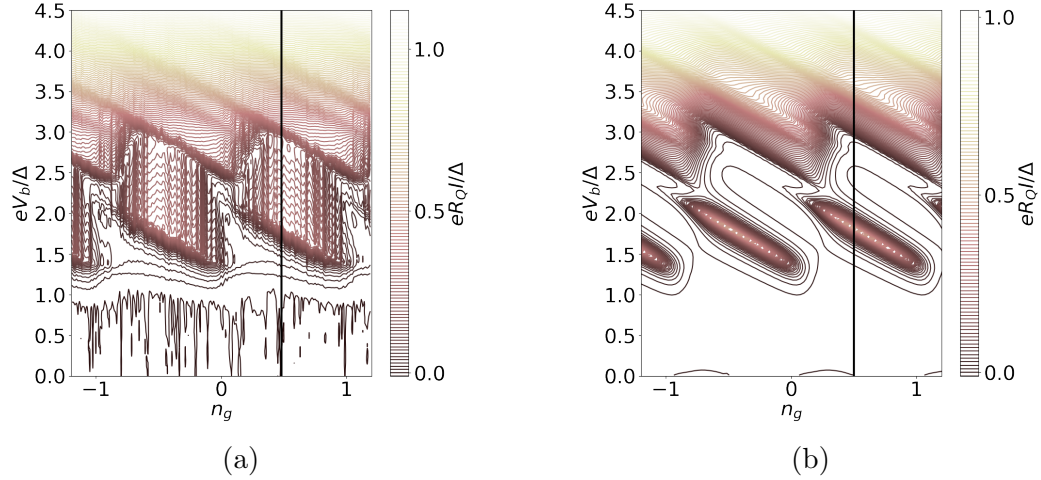


Figure 6.5: Experimental (a) and simulated (b) data for sample I with $R_{\text{TB}} = 43.25 \text{ k}\Omega$ and $R_{\text{BJ}} = 29.5 \text{ k}\Omega$ ($\mathcal{T} \sim 0.44$). For the simulation we just considered one channel, so $\tau = \mathcal{T}$). The lines starting around 2.5Δ cover the QP lines between 3Δ and $3\Delta + 2E_C$, meaning that the main process that it measured now is MAR. The hysteresis coming from the JQP covers partially the MARQP starting at 2.5Δ (up-sweep measurement). The vertical black line is a cut at a constant gate of $n_g = 0.5$ plotted in figure 6.6.

MAR and with it we can conclude that the signatures that are below 3Δ (besides the JQP) are due to MAR of order 2, as already shown in previous works [24] [77] [78]. However, in this measurement we don't see any clear high-order MAR signature because the amplitude of orders over 3 is still rather small for this \mathcal{T} .

In figure 6.5 we show data of a contact with a higher transmission for the MCBJ and that shows processes with a higher amplitude inside the gap region. Notice that at this point we don't see any distinct line starting between 3Δ and $3\Delta + 2E_C$. The MAR process amplitude starting at around 2.5Δ in figure 6.5 is big enough for covering the single-electron process at higher V_b .

Although higher orders of MAR appear at lower values of V_b for atomic contacts, in the SET it is also necessary to pay the E_C of the island for charging it (equation 2.16). Therefore, it is expected that higher-order MAR doesn't appear for low values of V_b , but the opposite: MAR processes of order n will appear at higher values of V_b if we assume that they charge the

island with n particles. Therefore, we do not expect to measure further kinks at lower V_b than $2\Delta + E_C$ and in principle we will not be able to associate new peaks to contributions of a specific order of MAR. However, we will see a difference coming from the MAR in the final amplitude of the total current going through the SET.

The simulation allows us to include or exclude different orders of MAR, so that it is possible to differentiate what actually contributes to the final current. We present the result of this analysis in figure 6.6. Sub-figure 6.6 (a) is the result after computing the master equation taking into account MAR until order 10, JQP processes described by the Averin-Aleshkin rate (eq. 2.22), and QP tunnelling. The black lines are the experiment lines, and the scatter plots correspond to the individual contributions to the simulated current as indicated in the legend. The sum of all these plots gives the theory line, grey solid line in figure 6.6.

The agreement in the JQP peak (resonance between $\Delta + E_C$ and 2Δ) is good in terms of amplitude, but in the experiment it occurs at a higher value of V_b . We argue that this deviation probably occurs because this expression is derived for a classical SET and not one containing an atomic contact. Besides, it depends on the Josephson energy which in our case is derived with the Ambegaokar-Baratoff formula for tunnel junctions, giving $E_J = \Delta/8R_{BJ}$ (R_{BJ} in units of R_Q). It has been shown that this expression, valid for tunnel barriers, does not hold true for weak links [79] with high τ_i .

The peaks that are visible in the theory beyond 3Δ occur roughly the same position in the experiment curves, but they are slightly faded out. Specially the peak at 3Δ , and we claim that this is because the hysteresis covers it partially, as it is visible in the contour plot from figure 6.5. The agreement between experiment and theory is, however, quite good: they both show the same amplitude and the peaks appear at the same position, as it is also visible in the plots of figure 6.5.

Sub-figures 6.6 (b) and (c) are also a cut at the same n_g as 6.6 (a), but including less processes: in 6.6 (b) we include AR and QP; while in 6.6 (c) we include QP. In all of them we include the JQP. Starting by this last subplot (c), in the theory line the transport after the JQP starts at some point after 3Δ , clearly bigger threshold than what we measured. In sub-figure 6.6 (b) the transport starts at the same point as in the experiment, but the amplitude of the current doesn't match as good as when we consider higher orders of MAR. Also the agreement between the features visible in the theory line do not correspond as well to the experiment as in sub-figure 6.6 (a).

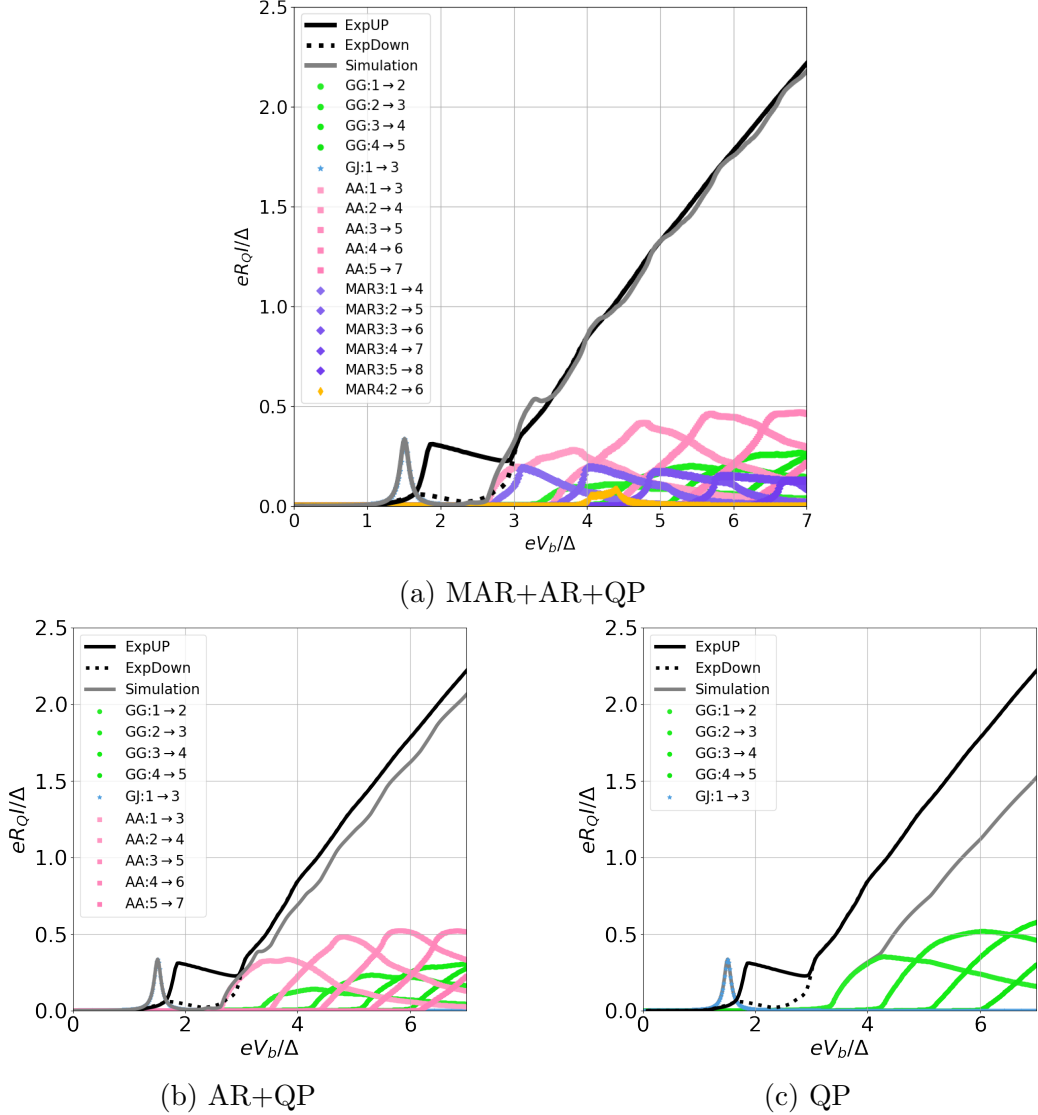


Figure 6.6: Cut from figure 6.5 at $n_g=0.5$. sub-figure (c) just includes quasi-particle (QP) transport, sub-figure (b) includes QP and MAR of order 2 (AR) and sub-figure (a) includes QP and MAR until order 10. As indicated in the legend, green dots are QP, pink squares AR and purple diamonds are MAR of order 3. The scatter plots just include contributions until a value of $I = 0.1\Delta/eR_Q$, but for the total current (grey line) all contributions are summed up. Black solid line is experimental up-sweep, black dotted line is the down-sweep.

For all of this, it is safe to say that in our experiments we measure MAR processes of order n that charge the island with n particles. They show up in the measured features (lines in the contour plots, peaks in the single $I-V_b$) as well as on the total amplitude of the final current.

For this simulation we considered that there was just one channel, so $\tau = \mathcal{T}$. Considering more than one channel with divided transmissions τ would lower the current value, giving a smaller amplitude for I than what we measured. Therefore, the only possibility left that justifies the fit is to consider orders of $\text{MAR} > 2$.

As a final remark, MAR of order 3 in a single MCBJ is just relevant for a small voltage range because after 2Δ its amplitude goes back to zero (figure 2.3 and 6.3). However, figure 6.6 shows how MAR-3 in the SET is also relevant for higher V_b .

6.4 Multi-particle transport for high transmission contacts

In this section we will focus on contacts that have a \mathcal{T} close to one, but we still can claim that there is no channel with $\tau = 1$.

Figure 6.7 includes two experimental plots from different samples where with high total transmission \mathcal{T} for the MCBJ. Figure 6.7 (a) corresponds to sample I with $R_{TB} = 43.25 \text{ k}\Omega$ and a contact with $R_{BJ} = 16 \text{ k}\Omega$ ($\mathcal{T} = 0.81$) for the MCBJ. The plot in figure 6.7 (b) is from sample II with $R_{TB} = 23.6 \text{ k}\Omega$ and a contact with $R_{BJ} = 11.1 \text{ k}\Omega$ ($\mathcal{T} = 1.16$) for the MCBJ.

When reaching a regime where $\mathcal{T} > 0.5$, we start to consistently observe a new process starting after Δ in all of our samples. This new process has a slope in the $V_b - V_g$ maps smaller than the other processes. In particular, it fits well to a factor $1/3$ with respect to the processes described in the previous sections (JQP, MARQP and QP cycles, with slopes that agree with the black line from figure 6.7 in both plots). This process is below the pink line in both plots from figure 6.7.

Another remarkable feature that is visible in our data is the elongation of all lines for a wide range of V_b . This is particularly visible in the case of the JQP and the MAR-QP line.

As we have already shown in section 5.1, at higher values of \mathcal{T} the cotunnelling of quasiparticles becomes bigger, specially for values of V_b that

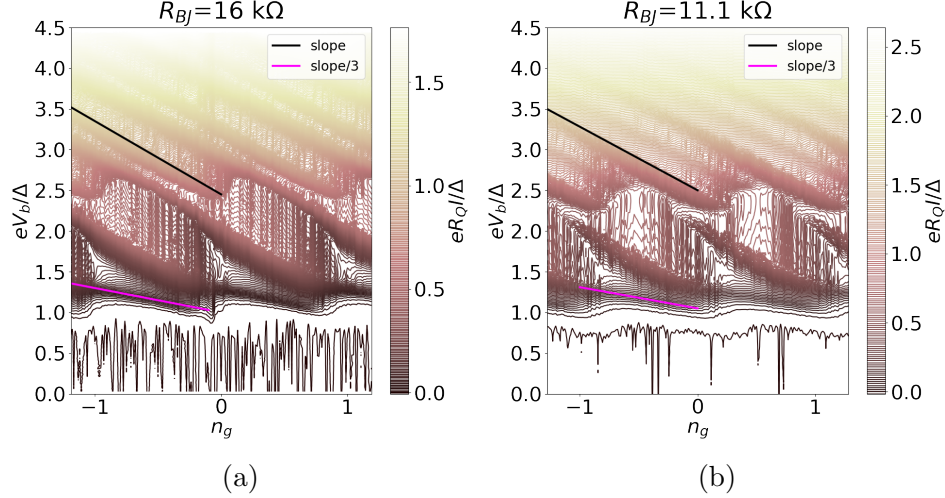


Figure 6.7: Contour plots for sample I (a) with $R_{TB} = 43.25 \text{ k}\Omega$ and $\mathcal{T} = 0.81$ for the MCBJ, and sample II (b) with $R_{TB} = 23.6 \text{ k}\Omega$ and $\mathcal{T} = 1.16$ for the MCBJ. The slope of the black line corresponds to processes that transport m particles and charge the island with m particles (JQP, MARQP and QP cycles explained in the previous sections). These maps show new features that have a slope with a factor $1/3$ (pink line) as indicated in the legend. This signature contains a process that transports 2 particles, but just charges the island with 1 electron (AQP-cot). Both plots are up-sweep measurements.

are closer to the diamond border. Below 3Δ it is not expected to have qp co-tunnelling because there are no quasiparticle states in the superconducting gap [66]. What is instead possible is to have the processes we explained before with MAR transport but, that they charge the island with less particles than they actually transport in total.

We will name this process as co-tunnelling-AQP (cot-AQP). We will be giving this slope this name because we know that some sort of co-tunnelling must be involved and besides, since there are no signatures of hysteresis as we normally see for the JQP, we can in principle assume this involves AR transport.

The energy necessary for charging the island would be:

$$\delta E_{AQPC} = E_{ch}(n) - E_{ch}(n \pm 1) + 3\kappa V_b \quad (6.1)$$

Instead of equation 2.13. The factor 3 in equation 6.1 is because we are

removing two particles from the left and putting one in the right lead (or vice-versa) and the electrostatic energy difference is the same as for single QP tunnelling because the island just gets charged with one particle. Processes that transport m particles and charge the island with m particles have the same slope independently of the specific value of m . In this case, since there is a simultaneous transport of three particles through two junctions but just one charges effectively the island, the slope will be a factor $1/3$ of what we used to see for the other features over the MCBJ.

The same mechanism applies for other type of higher order processes, in particular for the $3e$ process [48][47], as we explained in section 2.3.4, where we have two times this process (but with J instead of A) over different junctions.

When implementing these new processes to the simulation, the main problem is that we actually don't know their rates. They are not the same as for MAR of order n that charges the island with n particles. MAR rates are calculated for one unique junction while this AQP-cot process occurs on two junctions simultaneously and it is not possible to disentangle it into two separate transports processes in two junctions. Following the same naive argument as in section 5.1, we could take an approximation as the one we took with eq. 5.2, and assume that for this case $\Gamma_{\text{cot},\text{MAR}} = \gamma \Gamma_{\text{MAR}}$ being γ a factor that in this case we would have to figure out from our experimental data. However, this of course does not give us any information about the voltage dependence of this rate. Therefore, we would keep it simple and define this rate as step function that sets in at Δ (like the AR) which amplitude comes from a constant factor we determine from our experimental data.

Further difficulties are that in this regime for \mathcal{T} there are most likely several channels with transmission τ_i and what we already encountered in the previous section 6.3 with the JQP amplitude for the simulation.

Therefore we do not expect to obtain quantitative agreement between simulation and experiment, but to reproduce the tendency by including these other co-tunnelling processes on top of the ones already considered. In the simulation plot from figure 6.8(b) we have just taken the rate as a constant that sets in at 2Δ and has a value of $\gamma = 0.05(\Delta/neR_Q)$ (arbitrary amplitude that fits our measurement). This simulation was made for a contact from the sample I with $R_{\text{BJ}} = 16 \text{ k}\Omega$ corresponding to $\mathcal{T} = 0.81$.

By including the rate for the AQP-cot process, we were able to reproduce the line we measure at Δ (pink arrow in figure 6.8): it appears at the same positions and has the same slope as in the measurement. The lines for the

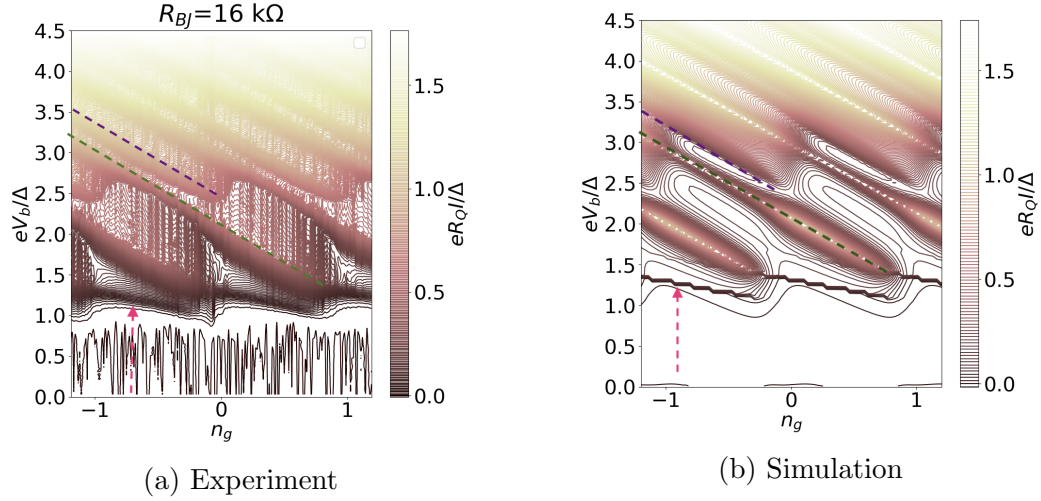


Figure 6.8: (a) Simulated map for $\mathcal{T} = 0.81$ and considering one channel and corresponding measured data for sample I. On top of MARQP, we are adding co-tunnelling processes that charge the island with one particle but transport a total of 2 particles. With this we are able to reproduce the processes marked on the maps with a purple dotted line (MAR processes), dark green line (JQP) and the one marked with a pink arrow (AQP with co-tunnelling).

MAR processes (purple dashed line) as well as the JQP (dark green dashed line) also appear in the correct position for the simulation. However, the JQP appears to have a bigger amplitude in the simulation than in the experiment, especially the subsequent peaks that we measure after the first peak. This is better visible in the the $I - V_b$ curve 6.9. By subsequent peaks we are referring to the peaks at 3Δ and 4Δ in sub-figure 6.9(a). It is remarkable how in the simulation (6.9 (a)) the subsequent JQP peaks appear as a resonant feature while in the correspondent experimental data (6.9(b)) we measure two dips in the same spots that just show an increase in current. Regarding this, probably there are more co-tunnelling processes that we are not yet taking into account. This is because although the total amplitude for the current agrees quite well between simulation and experiment (plots (a) and (b) from figure 6.9), right after the JQP peaks there is a decrease in the current amplitude that we do not measure.

We see these processes also in the same position for sample II (6.9 (c)),

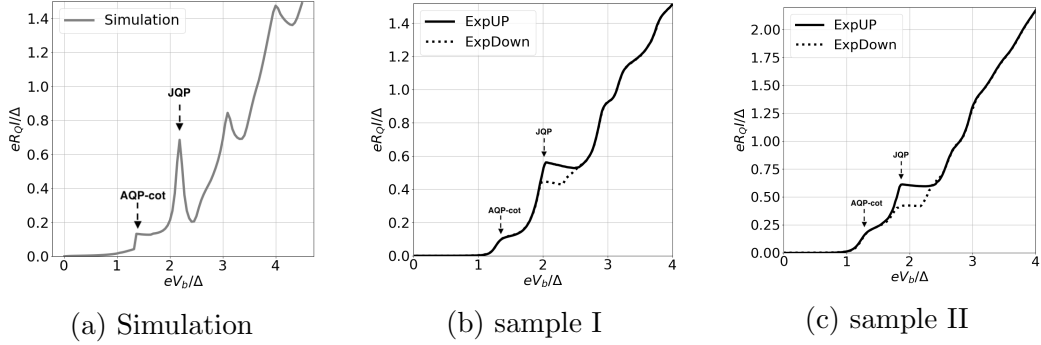


Figure 6.9: (b,c) Cuts at a constant n_g for the experimental maps from figure 6.7 and (a) from the simulation of figure 6.8 (b). The simulation reproduces the position of the new features (AQP-cot marked in the map), but cannot reproduce the subsequent peaks from the JQP, specially regarding the double peak behaviours that is visible in booth experimental plots.

and again, the same tendency for the $I - V_b$: no further resonant peaks from the JQP, but also there is an increase of the current around Δ . In sub-figure (c) this feature is slightly bigger than in sub-figure (b), which agrees with the fact that for lower values of R (in (c) both junctions have lower R) the amplitude of the co-tunnelling processes should be bigger.

A final remark is that although we just define the AQP-cot rate as a step function, it seems to agree relatively well with the measurement. This gives us the hint that the voltage dependence of this rate must be very similar to a step function. Since we don't have the full information about this rate, we cannot make a firm conclusion about its nature, and we can just claim that a process with an energy for charging the island with eq. 6.1 and that has the shape of a step function as we defined would fit our measured data.

6.5 Andreev reflection signatures in the strong coupling regime

In this section we will include results when the MCBJ has $\mathcal{T} \gg 1$. We already talked about the results in this regime for the normal SET in section 5.6. Here we will include the SC maps.

Figure 6.10 (a) is a colour map which represents V_b against n_g as in pre-

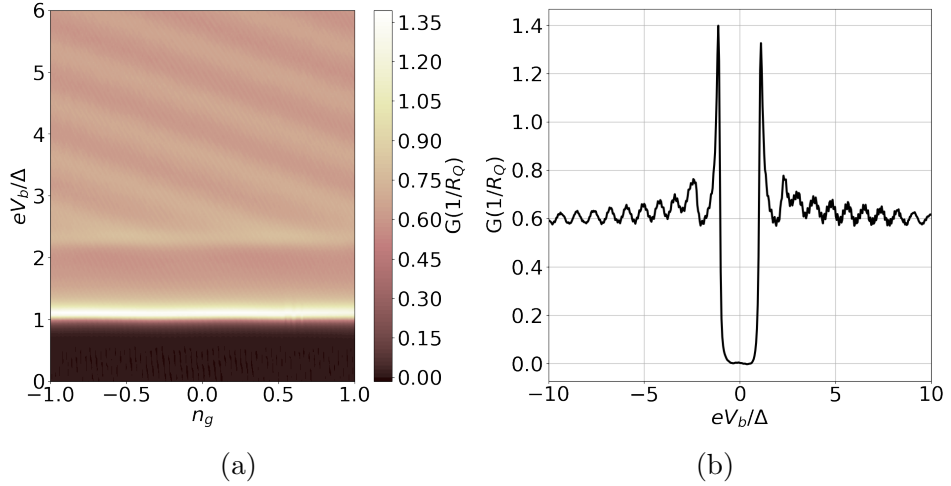


Figure 6.10: Plots for the strong coupling regime in the SSN-SET. Figure (a) is a conductance map for a contact from sample I with $\mathcal{T}=3.35$ and figure (b) is a cut at a constant n_g that represents conductance against V_b . For low voltages between 0 and Δ we measure the classical $G-V_b$ for a SIN junction. Between Δ and 2Δ there is a decrease in the conductance followed by a increase, and for every n_g there is a oscillatory behaviour starting at 2Δ . These oscillations extend until very high voltages.

vious maps, but now the colour scale represents the differential conductance. In this plot, the conductance is ~ 0 until Δ , when there is a maximum peak which is not modulated by the gate. Between Δ and 2Δ there is no characteristic feature, just a constant conductance different than zero. After 2Δ there is, however, some modulation that has the same slope as processes going through the MCBJ from previous maps. These modulations are oscillations in the conductance as visible from figure 6.10(b). Here we can see between 0 and Δ the regular gap for a SIN junction, and that the conductance increases just before 2Δ . After , the oscillatory behaviour starts. This extends until very high V_b , over 10Δ .

It is hard to simulate this regime. In this regime, higher order processes play a big role, and as we have said, we don't know the rates for these events. On the other hand, it seems that all cp processes start at Δ , like in a regular SIN junction, and then this eliminates all traces of JQP on the maps. The features starting after 2Δ should be due to MAR. It is quite remarkable that these features are still gate-modulated, because in the normal case this

contact didn't show gate modulation anymore: the map shown in fig. (6.10) is the SC map of the same contact as the NC map from fig.(5.6). In the SC map of fig.(6.10) the modulation displacement (i.e., the exact position of the maximum and minimum peaks depending on n_g) depends on the chosen gate voltage, while in fig. (5.6) we measured always the same conductance dip independently of n_g . This would mean that while the charge states in the NNN-SET have vanished, in the SSN-SET they can still remain.

Chapter 7

Conclusions

We have fabricated SETs with a tunable atomic contact that substitutes one of the classical tunnel barriers. With this device we were able to first explore the limits of the conditions that define a SET (the junctions must have low C for avoiding thermal fluctuations and high R for avoiding quantum fluctuations). First, we could demonstrate how CB oscillations vanish for high \mathcal{T} contacts, but the CB remains visible as dynamical CB even for contacts with $\mathcal{T} \gg 1$. In our case, since atomic contacts of multivalent metals tend to have more than one channel, these oscillations didn't exactly vanish at $\mathcal{T} = 1$, but at a higher total value of \mathcal{T} for which there is at least $\tau = 1$. Also, it was possible to confirm that E_C didn't change or vanish until there was a ballistic contact on the MCBJ. This overall concludes that the charging effects remain even for contacts with $R < R_Q$ and for values of $G \sim G_0$. However, having a contact with $\tau = 1$ makes it impossible to differentiate any feature coming from E_C , eliminates all CB oscillations, and the only remaining is the dynamical CB. In this respect, a wide range of measurements adjusting the MCBJ in a configuration of $R_{\text{MCBJ}} \sim 2k\Omega - 15k\Omega$, i.e., studying very high transmissions but with different τ_i division between the different contacts, can clarify this latter affirmation. Besides, using other materials for the MCBJ can also help in this matter: instead of using a multivalent element like Al, which has several conduction channels [58], gold single-atom contacts have shown to have just one transmission channel [80], so that we can assume that $\mathcal{T} \sim \tau$, and it would be possible with this setup to confirm if the charging effects vanish when $\mathcal{T} = 1$.

With this device it was also possible to study the modulation of cp and MAR by CB charging effects. Our data shows that the features that we start

to measure in the gap region, i.e., between Δ and 3Δ are due to cp and MAR transport cycles. Simulations using the master equation approach verify these findings up to values for the $R_{BJ} \sim 30k\Omega$. AR contributes to the final current, and this was proven because this process sets in before single electron transport, as we have seen in the measurement. On top, considering higher orders of MAR gives an excellent agreement between theory and experiment, which also proves that MAR of order n charges the island with n particles. Contrary to a single MCBJ, in the SET higher orders of MAR contribute also for large V_b .

For smaller R higher order processes appear at low voltages. These imply the simultaneous particle transport through two junctions that does not charge the island. These processes require tunnelling rates that we do not know and that therefore we cannot implement in the master equation. However, it was possible to obtain where and with which slope these processes would set in by defining an arbitrary step rate. This agrees, qualitatively, with the measurements, proving that this process charges the island with the defined δE and that its rate must be very similar to a step function.

A possible improvement would be to first be able to model how the co-tunnelling contributes to the excess current measured inside the diamonds in the NNN-SET. Specific rates for the processes that imply the simultaneous transport over two junctions are necessary in order to obtain a quantitatively agreement between theory and experiment, and in order to fully differentiate different contributions. We have argued that it would be necessary to know the rate for the AQP-cot, a process that implies the simultaneous tunnelling of two particles in one junction and one in the other, charging the island with one particle. Probably, other types of co-tunnelling processes implying several quasiparticles (co-tunnelling of AR for instance) also play a role, because we keep measuring a higher current in comparison with the simulation for some parts of the $I - V_b$. Finally, several ingredients are necessary for understanding the measurements on the strong coupling regime, and most likely, the understanding of this regime is linked to the better understanding and modelling of multi-terminal Josephson junctions.

Appendix A

List of samples

In this appendix we list the SSN-SET samples presented in this thesis, measured between 05.2019 and 07.2021. The list includes the resistance of the contacts adjusted in the MCBJ for each sample, and the corresponding E_C , κ_{BJ} , coupling from the gate to the island α and T. About the superconducting gap Δ , for all of them the value is approx 182 μeV .

In tables A.2-A.4 there is a summary for all the measured contacts for samples I-III respectively. We present the resistance R_{BJ} and correspondent transmission \mathcal{T}_{BJ} for the MCBJ of each of this contacts , as well as the bath (T_b) and electronic (T_e) temperature.

Table A.1: Summary with the most important values from each of the samples presented. The R for the TB are at RT (room temperature) and base temperature ($\sim 40 \text{ mK}$). We also include the charging energy E_C , the capacitor divisor for the BJ κ_{BJ} and the coupling between gate and island α .

	Sample I	Sample II	Sample III
$R_{TB} (\text{k}\Omega)$ [RT]	49.33	23.60	18.73
$R_{TB} (\text{k}\Omega)$	43.24	23.60	17.85
$E_C (\mu\text{eV})$	69.76	63.82	54.60
κ_{BJ}	0.86	0.81	0.873
α (mV)	0.0042	0.0038	0.0024

Table A.2: Sample I: summary of all the contacts measured, with $R_{\text{BJ}}=R$ of the MCBJ, \mathcal{T}_{BJ} =transmission of the MCBJ, T_b =bath temperature and T_e =electronic temperature.

$R_{\text{TB}} = 43.25\text{k}\Omega$			
R_{BJ}	\mathcal{T}_{BJ}	T_b (mK)	T_e (mK)
1216.2	0.011	31.96	72.94
859.5	0.015	44.96	106.02
488.9	0.026	45.1	88.04
347.4	0.037	37.52	101.30
307.8	0.042	36.78	87.15
256.6	0.050	35.83	93.93
260.6	0.050	33.35	147.82
218.8	0.059	39.62	115.21
204.0	0.063	39.51	158.73
190.4	0.068	42.25	118.49
158.1	0.082	36.2	140.59
150.1	0.086	45.55	152.93
108.7	0.119	40.75	127.92
18.6	0.695	44.34	106.34
29.5	0.438	45.12	135.49
22.7	0.570	39.26	119.50
16.1	0.804	47.88	136.14
11.0	1.178	42.06	133.98
3.9	3.351	57.11	199.90
2.3	5.733	43.06	-

Table A.3: Sample II

$R_{\text{TB}} = 23.60 \text{k}\Omega$			
R_{BJ}	\mathcal{T}_{BJ}	T_b (mK)	T_e (mK)
386.4	0.033	123.54	151.55
316.4	0.041	135.48	151.00
184.2	0.070	66.6	136.59
162.8	0.079	115.2	178.19
166.6	0.077	68.01	165.43
154.5	0.083	140.24	134.49
139.3	0.093	98.65	150.37
122.3	0.105	116.58	153.53
105.4	0.122	111	162.80
102.5	0.126	124.66	161.69
92.9	0.139	125.54	167.41
74.4	0.173	124.88	149.40
40.3	0.320	79.65	181.46
17.8	0.725	143.39	133.08
15.3	0.843	120.13	139.55
11.1	1.162	86.44	127.97
3.44	3.750	158.53	-
1.4	9.214	98.04	-

Table A.4: Sample III

$R_{\text{TB}} = 17.85 \text{k}\Omega$			
R_{BJ}	\mathcal{T}_{BJ}	T_b (mK)	T_e (mK)
808.4	0.016	61.64	147.85
747.5	0.017	35.75	137.99
232.2	0.056	48.03	115.83
134.8	0.096	57.74	77.97
131.1	0.098	43.6	145.05
131.2	0.098	45.98	183.21
118.4	0.109	58.04	120.24
91.0	0.142	36.71	124.01
86.8	0.149	39.09	104.60
68.7	0.188	34.28	85.59
52.5	0.246	35.98	88.19
48.4	0.267	34.53	129.43
40.9	0.315	51.41	156.97
36.8	0.351	44.38	227.75
14.4	0.899	43.11	155.36
7.4	1.735	46.42	-

Appendix B

Python code

This section includes the code for simulating the current through a SSN SET written in Python 3.9.7. In particular, it gives back the V_g - V_b – I map for a defined R_{BJ} , R_{TB} , κ_{BJ} and E_C . Everything is in units of the sc gap, so $\Delta = 1$. It includes MAR until order 10. With this particular set of parameters, it will reproduce fig. 6.5 (b).

```
%reset -f
import numpy as np
import matplotlib.pyplot as plt
plt.rcParams.update({'font.size':30})
import scipy.integrate as sci
from scipy.interpolate import interp1d
levels=np.arange(-10,20,1)
ls=np.size(levels)
#define the number of energy levels of the SET
print('Levels=',levels)
print('N levels=',ls)

#read david's data
import scipy.io
Vbjpos=np.arange(0.1,6,0.01)
Vbjneg=np.arange(-5.99,-0.09,0.01)
Vbj=np.concatenate((Vbjneg, Vbjpos), axis=0)
Vbj=np.append(Vbj,50)
Vbj=np.insert(Vbj,0,[-50])
```

```

#import the transmission data from the directory where I saved it
#just one transmission
ratesDavid=scipy.io.loadmat(r'C:\Users\P1_results_0.44_n_10_Nchi_100')
ratesBJ=np.real(ratesDavid['In_final'])
#ratesBJ=np.vstack((np.zeros((Vbjneg.size,11)),ratesBJpos))

#different channels
ratesDavid=scipy.io.loadmat(r'C:\Users\P1_results_0.40_n_10_Nchi_100')
ratesBJ1=np.real(ratesDavid['In_final'])
ratesDavid=scipy.io.loadmat(r'C:\Users\P1_results_0.04_n_10_Nchi_100')
ratesBJ2=np.real(ratesDavid['In_final'])
ratesDavid=scipy.io.loadmat(r'C:\Users\P1_results_0.02_n_10_Nchi_100')
ratesBJ3=np.real(ratesDavid['In_final'])
ratesBJ=ratesBJ1+ratesBJ2+ratesBJ3

#add initial and final values
EfinalValue=((ratesBJ[-1,11]-ratesBJ[-20,11])/0.2)*(50-5.99)+ratesBJ[-1,11]
erate=np.append(ratesBJ[:,11],EfinalValue)
erate=np.insert(erate,0,0)

arate=np.append(ratesBJ[:,12],ratesBJ[-1,12])
erate=np.insert(arate,0,0)
arate=arate/2

marate=np.append(ratesBJ[:,13],0)
marate=np.insert(marate,0,0)
marate=marate/3

marate4=np.append(ratesBJ[:,14],0)
marate4=np.insert(marate4,0,0)
marate4=marate4/4

marate5=np.append(ratesBJ[:,15],0)
marate5=np.insert(marate5,0,0)
marate5=marate5/5

marate6=np.append(ratesBJ[:,16],0)
marate6=np.insert(marate6,0,0)
marate6=marate6/6

```

```

marate7=np.append(ratesBJ[:,17],0)
marate7=np.insert(marate7,0,0)
marate7=marate7/7

marate8=np.append(ratesBJ[:,18],0)
marate8=np.insert(marate8,0,0)
marate8=marate8/8

marate9=np.append(ratesBJ[:,19],0)
marate9=np.insert(marate9,0,0)
marate9=marate9/9

marate10=np.append(ratesBJ[:,20],0)
marate10=np.insert(marate10,0,0)
marate10=marate10/10

#and now the interpolation function

rateSSr=interp1d(Vbj,erate)
rateSSL=interp1d(Vbj,erate)

AArateSSr=interp1d(Vbj,arate)
AArateSSL=interp1d(Vbj,arate)

MAR3rateSSr=interp1d(Vbj,marate)
MAR3rateSSL=interp1d(Vbj,marate)

MAR4rateSSr=interp1d(Vbj,marate4)
MAR4rateSSL=interp1d(Vbj,marate4)

MAR5rateSSr=interp1d(Vbj,marate5)
MAR5rateSSL=interp1d(Vbj,marate5)

MAR6rateSSr=interp1d(Vbj,marate6)
MAR6rateSSL=interp1d(Vbj,marate6)

MAR7rateSSr=interp1d(Vbj,marate7)
MAR7rateSSL=interp1d(Vbj,marate7)

```

```

MAR8rateSSr=interp1d(Vbj,marate8)
MAR8rateSSL=interp1d(Vbj,marate8)

MAR9rateSSr=interp1d(Vbj,marate9)
MAR9rateSSL=interp1d(Vbj,marate9)

MAR10rateSSr=interp1d(Vbj,marate10)
MAR10rateSSL=interp1d(Vbj,marate10)

#let's plot this to see how it looks...

fig0=plt.figure(figsize=(10,10))
ax0=fig0.add_subplot(111)

ax0.plot(Vbj,erate,color='green',label='1e',linewidth=4)
ax0.plot(Vbj,arate,color='deeppink',label='2e',linewidth=4)
ax0.plot(Vbj,marate,color='indigo',label='3e',linewidth=4)
ax0.plot(Vbj,marate4,color='gold',label='4e',linewidth=4)
ax0.plot(Vbj,marate5,color='peru',label='5e',linewidth=4)
ax0.plot(Vbj,marate6,color='black',label='6e',linewidth=4)
ax0.plot(Vbj,marate7,color='red',label='7e',linewidth=4)
ax0.plot(Vbj,marate8,color='teal',label='8e',linewidth=4)
ax0.plot(Vbj,marate9,color='gray',label='9e',linewidth=4)
ax0.plot(Vbj,marate10,color='cyan',label='10e',linewidth=4)

#ax0.scatter(Vbj,ratesBJ[:,9],color='orange')

ax0.set_xlim([0,4])
ax0.set_ylim([0,1])
#ax0.scatter(Vbj,ratesBJ[:,9],color='orange')
ax0.set_xlabel(r'$\delta E$')
ax0.set_ylabel(r'$e R_Q I/\Delta$')
#ax0.set_title(r'$R_{BJ}=29.5 \ k\Omega$')
ax0.legend()
ax0.grid()

#Parameters of the sample
#Left junction: BJ(SS). Right junction: TB(SN)

```

```

Delta = 1 #everything is in units of the gap Delta.
EC = 0.38 #charging energy

kappaleft = 0.86 #capacitor divisor of the MCBJ
kapparight = 1-kappaleft #capacitor divisor of the TB

Rleft=29.45/25.8 #Resistance of the MCBJ
Rright=43.24/25.8 #Resistance of the TB

Jleft = Delta/8./Rleft;
#Here you can define more points for the bias and gate voltage for
#obtaining a better resolution map.
#This would take more time.
BiasPoints=np.linspace(0.01,4.5,100)
GatePoints=np.linspace(-1,1.9,100)

parityrate = 10**(-12)

#Functions for calculating the different rates

def Ech(N,Ng):
    return np.array([EC*(N-Ng)**2])

def ediff(Ninit,Nfin,Ng,eV,VoltageGain):
    return np.array([Ech(Ninit,Ng)-Ech(Nfin,Ng)+VoltageGain*eV])

def ediff2(Ninit,Nfin,Ng,eV,VoltageGain):
    return np.array([Ech(Ninit,Ng)-Ech(Nfin,Ng)+2*VoltageGain*eV])

def ediff3(Ninit,Nfin,Ng,eV,VoltageGain):
    return np.array([Ech(Ninit,Ng)-Ech(Nfin,Ng)+3*VoltageGain*eV])

def ediff4(Ninit,Nfin,Ng,eV,VoltageGain):
    return np.array([Ech(Ninit,Ng)-Ech(Nfin,Ng)+4*VoltageGain*eV])

def ediff5(Ninit,Nfin,Ng,eV,VoltageGain):
    return np.array([Ech(Ninit,Ng)-Ech(Nfin,Ng)+5*VoltageGain*eV])

```

```

def ediff6(Ninit,Nfin,Ng,eV,VoltageGain):
    return np.array([Ech(Ninit,Ng)-Ech(Nfin,Ng)+6*VoltageGain*eV])

def ediff7(Ninit,Nfin,Ng,eV,VoltageGain):
    return np.array([Ech(Ninit,Ng)-Ech(Nfin,Ng)+7*VoltageGain*eV])

def ediff8(Ninit,Nfin,Ng,eV,VoltageGain):
    return np.array([Ech(Ninit,Ng)-Ech(Nfin,Ng)+8*VoltageGain*eV])

def ediff9(Ninit,Nfin,Ng,eV,VoltageGain):
    return np.array([Ech(Ninit,Ng)-Ech(Nfin,Ng)+9*VoltageGain*eV])

def ediff10(Ninit,Nfin,Ng,eV,VoltageGain):
    return np.array([Ech(Ninit,Ng)-Ech(Nfin,Ng)+10*VoltageGain*eV])

#quasiparticle rates

def dosNS(E):
    #superconducting DOS normalised with respect to the normal state
    if np.abs(E)>Delta:
        return
        np.real(np.abs(E-gammaD*1j)/np.sqrt((E-gammaD*1j)**2-Delta**2))
    else:
        return 0
def FermiD(b,E):
    return 1/(1+np.exp(b*E))

def rateNSint(E, bn, bs, deltaE):
    return dosNS(E)*FermiD(bn, E-deltaE)*(1-FermiD(bs, E))

biasNSa=np.linspace(-60,-4.9,10)
biasNSb=np.linspace(-5,5,400)
biasNSc=np.linspace(5.1,60,10)
biasNS=np.concatenate((biasNSa,biasNSb,biasNSc))
rate=np.zeros((biasNS.size))
#realistic temperature
#bn=1.609e-19*10e-3/(0.05*1.38e-23)
gammaD=0.004
bn=20
bs=100

```

```

for i in range(biasNS.size):
    deltaE=biasNS[i]
    rate[i]=
    (1/Rright)*sci.quad(rateNSint,-np.inf,np.inf,args=(bn,bs,deltaE))[0]

rateNS=interp1d(biasNS,rate)

#Averin-Aleshkin rates (JQP)

rescutoff = 10**(-4)

def AvAJleftQPrightOff(Ninit, Nfin, Ng, eV):
    NJ1 = Ninit
    NJ2 = Ninit + 2
    ECpair = Ech(NJ1, Ng) - Ech(NJ2, Ng) + 2*kappaleft*eV +
    rescutoff
    gamma = rateNS(ediff(NJ2, Nfin, Ng, eV,kapparight))
    return gamma*(Jleft**2)/(4*ECpair**2+(gamma/(2*np.pi))**2)

def AvAJleftQPrightOn(Ninit, Nfin, Ng, eV):
    NJ1 = Ninit
    NJ2 = Ninit - 2
    ECpair = Ech(NJ1, Ng) - Ech(NJ2, Ng) - 2*kappaleft*eV +
    rescutoff
    gamma = rateNS(ediff(NJ2, Nfin, Ng, eV,-kapparight))
    return gamma*(Jleft**2)/(4*ECpair**2+(gamma/(2*np.pi))**2)

#Solve master equation

import time
start_time = time.time()
Ileft=np.zeros((BiasPoints.size,GatePoints.size))
Irigh=nt.zeros((BiasPoints.size,GatePoints.size))

for m in range(GatePoints.size):
    Ng=GatePoints[m]

```

```

for h in range(BiasPoints.size):
    vb=BiasPoints[h]
    #matrices for charging/decharging for 1,2...10 charges
    #GG:charging(C)/decharging(D) the island with one particle.
    AA:chargind(C)/decharging(D)
    #the island with two particles.
    MARn:chargind(C)/decharging(D) the island w n particles.
    #defined as matrices of zeros that are after filled with
        the rates
    GGC=np.zeros((3,levels.size))
    GGD=np.zeros((3,levels.size))
    AAC=np.zeros((1,levels.size))
    AAD=np.zeros((1,levels.size))
    MAR3C=np.zeros((1,levels.size))
    MAR3D=np.zeros((1,levels.size))
    MAR4C=np.zeros((1,levels.size))
    MAR4D=np.zeros((1,levels.size))
    MAR5C=np.zeros((1,levels.size))
    MAR5D=np.zeros((1,levels.size))
    MAR6C=np.zeros((1,levels.size))
    MAR6D=np.zeros((1,levels.size))
    MAR7C=np.zeros((1,levels.size))
    MAR7D=np.zeros((1,levels.size))
    MAR8C=np.zeros((1,levels.size))
    MAR8D=np.zeros((1,levels.size))
    MAR9C=np.zeros((1,levels.size))
    MAR9D=np.zeros((1,levels.size))
    MAR10C=np.zeros((1,levels.size))
    MAR10D=np.zeros((1,levels.size))

    for i in range(levels.size):
        if i<(ls-1):
            GGC[0,i]=rateNS(ediff(levels[i],levels[i+1],Ng,vb,-kapparight))
            GGC[1,i]=rateSS1(ediff(levels[i],levels[i+1],Ng,vb,kappaleft))
            GGC[2,i]= AvAJleftQPrightOff(levels[i],levels[i+1],
                Ng, vb) #cp left junction
        if i>0:
            GGD[0,i]=rateNS(ediff(levels[i],levels[i-1],Ng,vb,kapparight))
            GGD[1,i]=rateSSr(ediff(levels[i],levels[i-1],Ng,vb,-kappaleft))
            GGD[2,i]= AvAJleftQPrightOn(levels[i],levels[i-1],

```

```

Ng, vb) #cp left junction

if i<(ls-2):
    AAC[0,i]=
        AArateSS1(ediff2(levels[i],levels[i+2],Ng,vb,kappaleft)/2)

if i>1:
    AAD[0,i]=
        AArateSSr(ediff2(levels[i],levels[i-2],Ng,vb,-kappaleft)/2)

if i<(ls-3):
    MAR3C[0,i]=
        MAR3rateSS1(ediff3(levels[i],levels[i+3],Ng,vb,kappaleft)/3)

if i>2:
    MAR3D[0,i]=
        MAR3rateSSr(ediff3(levels[i],levels[i-3],Ng,vb,-kappaleft)/3)

if i<(ls-4):
    MAR4C[0,i]=
        MAR4rateSS1(ediff4(levels[i],levels[i+4],Ng,vb,kappaleft)/4)

if i>3:
    MAR4D[0,i]=
        MAR4rateSSr(ediff4(levels[i],levels[i-4],Ng,vb,-kappaleft)/4)

if i<(ls-5):
    MAR5C[0,i]=
        MAR5rateSS1(ediff5(levels[i],levels[i+5],Ng,vb,kappaleft)/5)
if i>4:
    MAR5D[0,i]=
        MAR5rateSSr(ediff5(levels[i],levels[i-5],Ng,vb,-kappaleft)/5)

if i<(ls-6):
    MAR6C[0,i]=
        MAR6rateSS1(ediff6(levels[i],levels[i+6],Ng,vb,kappaleft)/6)
if i>5:
    MAR6D[0,i]=
        MAR6rateSSr(ediff6(levels[i],levels[i-6],Ng,vb,-kappaleft)/6)

```

```

if i<(ls-7):
    MAR7C[0,i]= MAR7rateSS1(ediff7(levels[i],levels[i+7],
    Ng,vb,kappaleft)/7)
if i>6:
    MAR7D[0,i]= MAR7rateSSr(ediff7(levels[i],levels[i-7],
    Ng,vb,-kappaleft)/7)

if i<(ls-8):
    MAR8C[0,i]= MAR8rateSS1(ediff8(levels[i],levels[i+8],
    Ng,vb,kappaleft)/8)
if i>7:
    MAR8D[0,i]= MAR8rateSSr(ediff8(levels[i],levels[i-8],
    Ng,vb,-kappaleft)/8)

if i<(ls-9):
    MAR9C[0,i]= MAR9rateSS1(ediff9(levels[i],levels[i+9],
    Ng,vb,kappaleft)/9)
if i>8:
    MAR9D[0,i]= MAR9rateSSr(ediff9(levels[i],levels[i-9],
    Ng,vb,-kappaleft)/9)

if i<(ls-10):
    MAR10C[0,i]=
        MAR10rateSS1(ediff10(levels[i],levels[i+10],
        Ng,vb,kappaleft)/10)
if i>9:
    MAR10D[0,i]=
        MAR10rateSSr(ediff10(levels[i],levels[i-10],
        Ng,vb,-kappaleft)/10)
#from these matrices we can obtain the total contribution
    by summing up the columns of each matrix (marked with s)

```

```

GGCs=np.sum(GGC, axis=0)
GGDs=np.sum(GGD, axis=0)
AACs=np.sum(AAC, axis=0)
AADs=np.sum(AAD, axis=0)
MAR3Cs=np.sum(MAR3C, axis=0)
MAR3Ds=np.sum(MAR3D, axis=0)

```

```

MAR4Cs=np.sum(MAR4C, axis=0)
MAR4Ds=np.sum(MAR4D, axis=0)
MAR5Cs=np.sum(MAR5C, axis=0)
MAR5Ds=np.sum(MAR5D, axis=0)
MAR6Cs=np.sum(MAR6C, axis=0)
MAR6Ds=np.sum(MAR6D, axis=0)
MAR7Cs=np.sum(MAR7C, axis=0)
MAR7Ds=np.sum(MAR7D, axis=0)
MAR8Cs=np.sum(MAR8C, axis=0)
MAR8Ds=np.sum(MAR8D, axis=0)
MAR9Cs=np.sum(MAR9C, axis=0)
MAR9Ds=np.sum(MAR9D, axis=0)
MAR10Cs=np.sum(MAR10C, axis=0)
MAR10Ds=np.sum(MAR10D, axis=0)

#with all of these elements now we can build the matrix for
    solving the master equation;
#first we create a matrix of zeros M.

M=np.zeros((ls,ls))

#we add the rates to the matrix

for l in range(levels.size):
    for s in range(levels.size):
        if l==s:
            M[l,s]=-(GGCs[1]+GGDs[1]+AACs[1]+AADs[1]+MAR3Ds[1]+
                      MAR3Cs[1]+MAR4Ds[s]+MAR4Cs[s]+MAR5Ds[s]+MAR5Cs[s]+
                      MAR6Ds[s]+MAR6Cs[s]+MAR7Ds[s]+MAR7Cs[s]+MAR8Ds[s]+
                      MAR8Cs[s]+MAR9Ds[s]+MAR9Cs[s]+MAR10Ds[s]+MAR10Cs[s])
        elif l-s==1:
            M[l,s]=GGDs[s]
        elif l-s==2:
            M[l,s]=AADs[s]
        elif l-s==3:
            M[l,s]=MAR3Ds[s]
        elif l-s==4:
            M[l,s]=MAR4Ds[s]
        elif l-s==5:
            M[l,s]=MAR5Ds[s]

```

```

        elif l-s== -6:
            M[l,s]=MAR6Ds[s]
        elif l-s== -7:
            M[l,s]=MAR7Ds[s]
        elif l-s== -8:
            M[l,s]=MAR8Ds[s]
        elif l-s== -9:
            M[l,s]=MAR9Ds[s]
        elif l-s== -10:
            M[l,s]=MAR10Ds[s]
        elif l-s== 1:
            M[l,s]=GGCs[s]
        elif l-s== 2:
            M[l,s]=AACs[s]
        elif l-s== 3:
            M[l,s]=MAR3Cs[s]
        elif l-s== 4:
            M[l,s]=MAR4Cs[s]
        elif l-s== 5:
            M[l,s]=MAR5Cs[s]
        elif l-s== 6:
            M[l,s]=MAR6Cs[s]
        elif l-s== 7:
            M[l,s]=MAR7Cs[s]
        elif l-s== 8:
            M[l,s]=MAR8Cs[s]
        elif l-s== 9:
            M[l,s]=MAR9Cs[s]
        elif l-s== 10:
            M[l,s]=MAR10Cs[s]

#at the end we add the normalisation condition
M=np.vstack([M,np.ones((1,levels.size))])

#we create the solution for the system
sol=np.zeros((levels.size,1))
sol=np.vstack([sol,1])

#and finally we can solve the eq system for obtaining the

```

```

probabilities

P=np.linalg.solve(M[1:ls+1],sol[1:ls+1])

#with P we can calculate the current

Ileft[h,m]=(np.matmul(GGC[1],P)+2*np.matmul(GGC[2],P)+2*np.matmul(AAC,P) +
+3*np.matmul(MAR3C,P)+4*np.matmul(MAR4C,P)+5*np.matmul(MAR5C,P) +
6*np.matmul(MAR6C,P)+7*np.matmul(MAR7C,P)+8*np.matmul(MAR8C,P) +
+9*np.matmul(MAR9C,P)+10*np.matmul(MAR10C,P)-
(np.matmul(GGD[1],P)+2*np.matmul(GGD[2],P)+2*np.matmul(AAD,P) +
3*np.matmul(MAR3D,P) +
4*np.matmul(MAR4D,P)+5*np.matmul(MAR5D,P) +
6*np.matmul(MAR6D,P)+7*np.matmul(MAR7D,P)+8*np.matmul(MAR8D,P) +
9*np.matmul(MAR9D,P)+10*np.matmul(MAR10D,P)))

Iright[h,m]=np.matmul(GGD[0],P)+np.matmul(GGC[2],P)-
(np.matmul(GGC[0],P)+np.matmul(GGD[2],P))
print("--- %s seconds ---" % (time.time() - start_time))

#create the map

GatePoints=np.linspace(-1,1.9,100)-0.45
fig0=plt.figure(figsize=(10,10),dpi=100)
ax0=fig0.add_subplot(111)
CP1=ax0.contour(GatePoints,BiasPoints,Ileft,120,cmap=plt.cm.pink)
cbar=fig0.colorbar(CP1,ticks=[0, 0.5, 1])
cbar.ax.set_ylabel(r'$e R_Q I/\Delta$')
ax0.set_xlabel(r'$n_g$')
ax0.set_ylabel(r'$e V_{\text{b}}/\Delta$')
ax0.set_xlim([-1.2,1.2])
ax0.set_ylim([0,4.5])
ax0.axvline(x=0.5,color='black',linewidth=3)

```

Bibliography

- [1] R. A. Millikan., “On the elementary electrical charge and the avogadro constant,” *Phys. Rev.*, vol. 2, pp. 109–143, 1913.
- [2] T. A. Fulton and G. J. Dolan, “Observation of single-electron charging effects in small tunnel junctions,” *Phys. Rev. Lett.*, vol. 59, pp. 109–112, 1987.
- [3] K. Likharev, “Single-electron transistors: Electrostatic analogs of the dc squids,” *IEEE Trans. Mag.*, vol. 23, no. 2, pp. 1142–1145, 1987.
- [4] D. Averin and K. Likharev, *Single electronics: A correlated transfer of single electrons and Cooper pairs in systems of small tunnel junctions (Chapter 6 of Mesoscopic phenomena in solids)*. Elsevier Science Publishers, 1991.
- [5] D. V. Averin and K. K. Likharev, “Coulomb blockade of single-electron tunneling, and coherent oscillations in small tunnel junctions,” *J. Low Temp. Phys.*, vol. 62, no. 3, pp. 345–373, 1986.
- [6] Y. Nazarov and Y. Blanter, *Quantum transport*. Cambridge university press, 2009.
- [7] V. Maisi, *Andreev tunneling and quasiparticle excitations in mesoscopic normal metal-superconductor structures*. PhD thesis, Aalto Yliopisto, Espoo, 2014.
- [8] M. Tinkham, *Introduction to superconductivity 2nd ed.* McGraw-Hill international editions, 1996.
- [9] R. C. Dynes, V. Narayanamurti, and J. P. Garno, “Direct measurement of quasiparticle-lifetime broadening in a strong-coupled superconductor,” *Phys. Rev. Lett.*, vol. 41, pp. 1509–1512, 1978.

- [10] G. L. Ingold, H. Grabert, and U. Eberhardt, “Cooper-pair current through ultrasmall josephson junctions,” *Phys. Rev. B*, vol. 50, pp. 395–402, 1994.
- [11] J. P. Pekola, V. F. Maisi, S. Kafanov, N. Chekurov, A. Kemppinen, Y. A. Pashkin, O.-P. Saira, M. Möttönen, and J. S. Tsai, “Environment-assisted tunneling as an origin of the dynes density of states,” *Phys. Rev. Lett.*, vol. 105, p. 026803, 2010.
- [12] J. C. Cuevas and E. Scheer, *Molecular electronics: an introduction to theory and experiment*. World Scientific Series in Nanoscience and Nanotechnology, 2017.
- [13] J. M. Van Ruitenbeek, A. Alvarez, I. Piñeyro, C. Grahmann, P. Joyez, M. H. Devoret, D. Esteve, and C. Urbina, “Adjustable nanofabricated atomic size contacts,” *Rev. Sci. Instrum.*, vol. 67, no. 1, pp. 108–111, 1996.
- [14] N. Agrait, A. L. Yeyati, and J. M. Van Ruitenbeek, “Quantum properties of atomic-sized conductors,” *Phys. Rep.*, vol. 377, no. 2-3, pp. 81–279, 2003.
- [15] J. C. Cuevas, A. Martín-Rodero, and A. L. Yeyati, “Hamiltonian approach to the transport properties of superconducting quantum point contacts,” *Phys. Rev. B*, vol. 54, pp. 7366–7379, 1996.
- [16] D. Averin and A. Bardas, “ac josephson effect in a single quantum channel,” *Phys. Rev. Lett.*, vol. 75, pp. 1831–1834, 1995.
- [17] J. Cuevas, *Electronic transport in Normal and Superconducting Nanocontacts*. PhD thesis, Universidad autónoma de Madrid, Madrid, 1999.
- [18] J. C. Cuevas and W. Belzig, “Full counting statistics of multiple andreev reflections,” *Phys. Rev. Lett.*, vol. 91, p. 187001, 2003.
- [19] J. C. Cuevas and W. Belzig, “dc transport in superconducting point contacts: A full-counting-statistics view,” *Phys. Rev. B*, vol. 70, p. 214512, 2004.

- [20] I. Snyman and Y. V. Nazarov, “Keldysh action of a multiterminal time-dependent scatterer,” *Phys. Rev. B*, vol. 77, p. 165118, 2008.
- [21] S. Pohlen, *The superconducting single electron transistor*. PhD thesis, Harvard University, Cambridge, Massachusetts, 1999.
- [22] J. Hergenrother, *Parity effects and charge transport in the single-electron transistor*. PhD thesis, Harvard University, Cambridge, Massachusetts, 1995.
- [23] M. Furlan, T. Heinzel, B. Jeanneret, and S. V. Lotkhov, “Coulomb blockade peak statistics influenced by background charge configuration,” *J. Low Temp. Phys.*, vol. 118, no. 5, pp. 297–306, 2000.
- [24] R. J. Fitzgerald, S. L. Pohlen, and M. Tinkham, “Observation of andreev reflection in all-superconducting single-electron transistors,” *Phys. Rev. B*, vol. 57, pp. R11073–R11076, 1998.
- [25] T. Lorenz, S. Sprenger, and E. Scheer, “Coulomb blockade and multiple andreev reflection in a superconducting single-electron transistor,” *J. Low Temp. Phys.*, vol. 191, no. 5, pp. 301–315, 2018.
- [26] S. L. Pohlen, R. J. Fitzgerald, and M. Tinkham, “The josephson–quasiparticle (jqp) current cycle in the superconducting single-electron transistor,” *Phys. B*, vol. 284, pp. 1812–1813, 2000.
- [27] M. T. Tuominen, J. M. Hergenrother, T. S. Tighe, and M. Tinkham, “Experimental evidence for parity-based 2e periodicity in a superconducting single-electron tunneling transistor,” *Phys. Rev. Lett.*, vol. 69, pp. 1997–2000, 1992.
- [28] Y. Nakamura, T. Sakamoto, and J. S. Tsai, “Study of josephson-quasiparticle cycles in superconducting single-electron transistors,” *JJAP*, vol. 34, no. 8S, p. 4562, 1995.
- [29] Y. Nakamura, C. D. Chen, and J. S. Tsai, “Quantitative analysis of josephson-quasiparticle current in superconducting single-electron transistors,” *Phys. Rev. B*, vol. 53, pp. 8234–8237, 1996.
- [30] T. A. Fulton, P. L. Gammel, D. J. Bishop, L. N. Dunkleberger, and G. J. Dolan, “Observation of combined josephson and charging effects in small tunnel junction circuits,” *Phys. Rev. Lett.*, vol. 63, pp. 1307–1310, 1989.

- [31] A. J. Manninen, Y. A. Pashkin, A. N. Korotkov, and J. P. Pekola, “Observation of thermally excited charge transport modes in a superconducting single-electron transistor,” *EPL*, vol. 39, no. 3, p. 305, 1997.
- [32] Y. Avishai, A. Golub, and A. D. Zaikin, “Quantum dot between two superconductors,” *EPL*, vol. 54, no. 5, p. 640, 2001.
- [33] T. Greibe, M. P. V. Stenberg, C. M. Wilson, T. Bauch, V. S. Shumeiko, and P. Delsing, “Are ‘pinholes’ the cause of excess current in superconducting tunnel junctions? a study of andreev current in highly resistive junctions,” *Phys. Rev. Lett.*, vol. 106, p. 097001, 2011.
- [34] T. M. Klapwijk, G. E. Blonder, and M. Tinkham, “Explanation of subharmonic energy gap structure in superconducting contacts,” *Physica B+C*, vol. 109, pp. 1657–1664, 1982.
- [35] T. Lorenz, *Wechselspiel von Vielteilchen-Transport und Ladungseffekten in supraleitenden Einzelelektronentransistoren*. PhD thesis, Universität Konstanz, Konstanz, 2018.
- [36] S. Sprenger, *Interplay between charging effects and multi-particle transport in superconducting single electron transistors with tunable junctions*. PhD thesis, Universität Konstanz, Konstanz, 2020.
- [37] R. Fazio, G. Schön, and J. Siewert, “Current–voltage characteristics of nss transistors,” *Phys. B*, vol. 284–288, pp. 1828–1829, 2000.
- [38] F. W. J. Hekking, L. I. Glazman, and G. Schön, “Andreev spectroscopy of josephson coupling,” *Phys. Rev. B*, vol. 51, pp. 15312–15316, 1995.
- [39] D. Sabonis, D. van Zanten, J. Suter, T. Karzig, D. I. Pikulin, J. I. Väyrynen, E. O’Farrell, D. Razmadze, P. Krogstrup, and C. M. Marcus, “Comparing tunneling spectroscopy and charge sensing of andreev bound states in a semiconductor-superconductor hybrid nanowire structure,” *arXiv*, 2021.
- [40] J. M. Hergenrother, M. T. Tuominen, and M. Tinkham, “Charge transport by andreev reflection through a mesoscopic superconducting island,” *Phys. Rev. Lett.*, vol. 72, pp. 1742–1745, 1994.

- [41] J. M. Hergenrother, M. T. Tuominen, and M. Tinkham, “Charge transport by andreev reflection through a mesoscopic superconducting island,” *Phys. Rev. Lett.*, vol. 72, pp. 1742–1745, 1994.
- [42] M. Tinkham, J. M. Hergenrother, and J. G. Lu, “Temperature dependence of even-odd electron-number effects in the single-electron transistor with a superconducting island,” *Phys. Rev. B*, vol. 51, pp. 12649–12652, 1995.
- [43] T. M. Eiles, J. M. Martinis, and M. H. Devoret, “Even-odd asymmetry of a superconductor revealed by the coulomb blockade of andreev reflection,” *Phys. Rev. Lett.*, vol. 70, pp. 1862–1865, 1993.
- [44] J. P. Pekola, O. P. Saira, V. F. Maisi, A. Kemppinen, M. Möttönen, Y. A. Pashkin, and D. V. Averin, “Single-electron current sources: Toward a refined definition of the ampere,” *Rev. Mod. Phys.*, vol. 85, pp. 1421–1472, 2013.
- [45] H. Grabert and M. H. Devoret, eds., *Single Charge Tunneling*. Springer, Boston, MA, 1992.
- [46] A. M. van den Brink, A. A. Odintsov, P. A. Bobbert, and G. Schön, “Coherent cooper pair tunneling in systems of josephson junctions: effects of quasiparticle tunneling and of the electromagnetic environment,” *Z. Phys.*, vol. 85, no. 3, pp. 459–467, 1991.
- [47] A. M. van den Brink, G. Schön, and L. J. Geerligs, “Combined single-electron and coherent-cooper-pair tunneling in voltage-biased josephson junctions,” *Phys. Rev. Lett.*, vol. 67, pp. 3030–3033, 1991.
- [48] P. Hadley, E. Delvigne, E. H. Visscher, S. Lähteenmäki, and J. E. Mooij, “ $3 e$ tunneling processes in a superconducting single-electron tunneling transistor,” *Phys. Rev. B*, vol. 58, no. 23, p. 15317, 1998.
- [49] O. P. Saira, *Electrostatic control of quasiparticles transport in superconducting hybrid nanostructures*. PhD thesis, Aalto Yliopisto, Espoo, 2013.
- [50] P. Joyez, V. Bouchiat, D. Esteve, C. Urbina, and M. H. Devoret, “Strong tunneling in the single-electron transistor,” *Phys. Rev. Lett.*, vol. 79, no. 7, p. 1349, 1997.

- [51] P. Joyez, D. Esteve, and M. H. Devoret, “How is the coulomb blockade suppressed in high-conductance tunnel junctions?,” *Phys. Rev. Lett.*, vol. 80, no. 9, p. 1956, 1998.
- [52] D. Chouvaev, L. S. Kuzmin, D. S. Golubev, and A. D. Zaikin, “Strong tunneling and coulomb blockade in a single-electron transistor,” *Phys. Rev. B*, vol. 59, pp. 10599–10602, 1999.
- [53] D. S. Golubev and A. D. Zaikin, “Strong electron tunneling through a small metallic grain,” *JETP*, vol. 63, no. 12, pp. 1007–1012, 1996.
- [54] A. Furusaki and K. A. Matveev, “Coulomb blockade oscillations of conductance in the regime of strong tunneling,” *Phys. Rev. Lett.*, vol. 75, pp. 709–712, 1995.
- [55] K. A. Matveev, “Coulomb blockade at almost perfect transmission,” *Phys. Rev. B*, vol. 51, pp. 1743–1751, 1995.
- [56] Y. V. Nazarov, “Coulomb blockade without tunnel junctions,” *Phys. Rev. Lett.*, vol. 82, pp. 1245–1248, 1999.
- [57] S. Jezouin, Z. Iftikhar, A. Anthore, F. D. Parmentier, U. Gennser, A. Cavanna, A. Ouerghi, I. P. Levkivskyi, E. Idrisov, E. V. Sukhorukov, L. I. Glazman, and F. Pierre, “Controlling charge quantization with quantum fluctuations,” *Nature*, vol. 536, no. 7614, pp. 58–62, 2016.
- [58] E. Scheer, P. Joyez, D. Esteve, C. Urbina, and M. H. Devoret, “Conduction channel transmissions of atomic-size aluminum contacts,” *Phys. Rev. Lett.*, vol. 78, pp. 3535–3538, 1997.
- [59] E. Scheer, N. Agrait, J. C. Cuevas, A. L. Yeyati, B. Ludoph, A. Martín-Rodero, G. R. Bollinger, J. M. van Ruitenbeek, and C. Urbina, “The signature of chemical valence in the electrical conduction through a single-atom contact,” *Nature*, vol. 394, no. 6689, pp. 154–157, 1998.
- [60] K. Gloos, P. Koppinen, and J. Pekola, “Properties of native ultrathin aluminium oxide tunnel barriers,” *J.Phys.*, vol. 15, no. 10, pp. 1733–1746, 2003.
- [61] N. Cai, G. Zhou, K. Müller, and D. E. Starr, “Tuning the limiting thickness of a thin oxide layer on al(111) with oxygen gas pressure,” *Phys. Rev. Lett.*, vol. 107, p. 035502, 2011.

- [62] F. Giazotto, T. T. Heikkilä, A. Luukanen, A. M. Savin, and J. P. Pekola, “Opportunities for mesoscopics in thermometry and refrigeration: Physics and applications,” *Rev. Mod. Phys.*, vol. 78, no. 1, p. 217, 2006.
- [63] Z. Iftikhar, S. Anthore, A. and Jezouin, F. D. Parmentier, Y. Jin, A. Cava, A. Ouerghi, U. Gennser, and F. Pierre, “Primary thermometry triad at 6 mK in mesoscopic circuits,” *Nat. comm.*, vol. 7, no. 1, pp. 1–7, 2016.
- [64] S. Jezouin, *Transport à travers un canal quantique élémentaire : action du circuit, quantification de la charge et limite quantique du courant de chaleur*. PhD thesis, Université Pierre et Marie Curie - Paris VI, 2014.
- [65] J. König, H. Schoeller, and G. Schön, “Cotunneling and renormalization effects for the single-electron transistor,” *Phys. Rev. B*, vol. 58, pp. 7882–7892, 1998.
- [66] D. V. Averin, A. N. Korotkov, A. J. Manninen, and J. P. Pekola, “Resonant tunneling through a macroscopic charge state in a superconducting single electron transistor,” *Phys. Rev. Lett.*, vol. 78, pp. 4821–4824, 1997.
- [67] L. J. Geerligs, D. V. Averin, and J. E. Mooij, “Observation of macroscopic quantum tunneling through the coulomb energy barrier,” *Phys. Rev. Lett.*, vol. 65, pp. 3037–3040, 1990.
- [68] C. Pasquier, U. Meirav, F. I. B. Williams, D. C. Glattli, Y. Jin, and B. Etienne, “Quantum limitation on coulomb blockade observed in a 2d electron system,” *Phys. Rev. Lett.*, vol. 70, no. 1, p. 69, 1993.
- [69] H. Schoeller and G. Schön, “Mesoscopic quantum transport: Resonant tunneling in the presence of a strong coulomb interaction,” *Phys. Rev. B*, vol. 50, pp. 18436–18452, 1994.
- [70] J. Wang, H. Guo, J. L. Mozos, C. C. Wan, G. Taraschi, and Q. Zheng, “Capacitance of atomic junctions,” *Phys. Rev. Lett.*, vol. 80, pp. 4277–4280, 1998.
- [71] M. H. Devoret, D. Esteve, H. Grabert, G.-L. Ingold, H. Pothier, and C. Urbina, “Effect of the electromagnetic environment on the coulomb

blockade in ultrasmall tunnel junctions,” *Phys. Rev. Lett.*, vol. 64, pp. 1824–1827, 1990.

- [72] L. W. Molenkamp, K. Flensberg, and M. Kemerink, “Scaling of the coulomb energy due to quantum fluctuations in the charge on a quantum dot,” *Phys. Rev. Lett.*, vol. 75, pp. 4282–4285, 1995.
- [73] K. Flensberg, “Capacitance and conductance of mesoscopic systems connected by quantum point contacts,” *Phys. Rev. B*, vol. 48, pp. 11156–11166, 1993.
- [74] K. Flensberg, “Capacitance and conductance of dots connected by quantum point contacts,” *Phys. B*, vol. 203, no. 3-4, pp. 432–439, 1994.
- [75] P. Joyez, *Le transistor à une paire de Cooper: un système quantique macroscopique*. PhD thesis, Université Paris-Saclay, Paris, 1995.
- [76] J. Senkpiel, R. Drost, J. C. Klöckner, M. Etzkorn, J. Ankerhold, J. C. Cuevas, F. Pauly, K. Kern, and C. R. Ast, “Extracting transport channel transmissions in scanning tunneling microscopy using superconducting excess current,” *Phys. Rev. B*, vol. 105, p. 165401, 2022.
- [77] V. F. Maisi, O. P. Saira, Y. A. Pashkin, J. S. Tsai, D. V. Averin, and J. P. Pekola, “Real-time observation of discrete andreev tunneling events,” *Phys. Rev. Lett.*, vol. 106, no. 21, p. 217003, 2011.
- [78] D. V. Averin and J. P. Pekola, “Nonadiabatic charge pumping in a hybrid single-electron transistor,” *Phys. Rev. Lett.*, vol. 101, no. 6, p. 066801, 2008.
- [79] J. Senkpiel, S. Dambach, M. Etzkorn, R. Drost, C. Padurariu, B. Kubala, W. Belzig, A. Levy-Yeyati, J. C. Cuevas, J. Ankerhold, C. Ast, and K. Kern, “Single channel josephson effect in a high transmission atomic contact,” *Comm. Phys.*, vol. 3, no. 1, pp. 1–6, 2020.
- [80] E. Scheer, W. Belzig, Y. Naveh, M. H. Devoret, D. Esteve, and C. Urbina, “Proximity effect and multiple andreev reflections in gold atomic contacts,” *Phys. Rev. Lett.*, vol. 86, pp. 284–287, 2001.